

UNIVERSITÀ DEGLI STUDI DI PADOVA

DIPARTIMENTO DI INGEGNERIA INDUSTRIALE

CORSO DI LAUREA MAGISTRALE IN INGEGNERIA ENERGETICA

Tesi Magistrale

**DESIGN OF A COMPACT COOLING SYSTEM FOR THE
FUTURE ITS OFF-DETECTOR ELECTRONICS IN THE ALICE
EXPERIMENT AT CERN**

Relatore: *Prof. Davide Del Col*

Correlatori: *Ing. Andrea Francescon*

Ing. Massimo Benettoni

Laureanda: *Claudia Cantarello*

ANNO ACCADEMICO 2015/2016

*“We cannot solve our problems with the same
thinking we used when we created them”*

A. Einstein

Index

Abstract	7
1 Alice Experiment at CERN	9
1.1 LHC	10
1.2 Particle Detectors	11
1.3 The ALICE experiment	12
1.4 The Current ALICE Detector	13
1.4.1 ITS	16
1.5 The ALICE upgrade	17
1.5.1 ITS upgrade.....	18
1.5.2 ITS Off-Detector Electronics	22
2 Preliminary Design	27
2.1 Requirements and Boundary Conditions	27
2.2 Preliminary Layout Definition	28
2.3 Thermal and Hydraulic Behaviour	32
2.3.1 Governing Equations	33
2.3.2 Boundary layer	34
2.3.2.1 Velocity Boundary Layer	35
2.3.2.2 Thermal Boundary Layer	36
2.3.3 Internal Flow	37
2.3.4 Heat Transfer Coefficients in Fully Developed Region.....	39
2.3.4.1 Constant Surface Heat Flux	40
2.3.4.2 Constant Wall Temperature	42
2.3.5 Pressure Drop in Fully Developed Region	43
2.3.6 Entry Region	44
2.3.7 Heat Transfer Coefficients in the Entry and Developing Region.....	44
2.3.8 Pressure Drop in Developing Region.....	46
2.3.9 Pressure Drop in Bends	47
3 Numerical Simulation of Partial Channel	49
3.1 Meshing Tools and Meshing Quality Parameters	49
3.2 Water Flow: Mesh Creation	53
3.2.1 Mesh Characterisation	54

3.3 Fluent Analysis	55
3.3.1 Heat Transfer Coefficients.....	59
3.4 Velocity profiles	61
3.5 Mesh Selection	62
4 Numerical Simulation of the System	63
4.1 Water Flow and Pipe Meshing	63
4.2 Plate Meshing	63
4.3 Simulation Results: Fluent Analysis	65
5 Experimental Investigation	71
5.1 Prototype Manufacturing	71
5.2 Test Section	73
5.3 Tests on the pipe	77
5.3.1 Test on the Connection Pipes.....	77
5.3.2 Test on the Serpentine	78
5.4 Test on the Plate	81
5.4.1 First Test with the Inlet Water Flow at 20°C.....	82
5.4.2 Second Test with the Inlet Water Flow at 15°C	84
5.4.3 Thermal Analysis with the Infrared Camera	85
6 Comparison Between Simulations and Experimental Results	89
Conclusions	93
Bibliography	95
Ringraziamenti	97

Abstract

One of the detectors installed in the LHC experiment at CERN, ALICE, will be partially rebuilt in 2020. The ALICE detector is situated hundred meters underground and is basically made of concentric layers. Each one performs different investigations on matter behaviour. The most inner tracker, ITS (Inner Tracking System), will be totally replaced by its new upgrade. This work starts with an overview of the LHC experiment at CERN and with the ALICE current detector features and its upgrade. The upgrade will provide a new carbon structure, a new cooling system and also a new read out electronics for external data reading and recording. For this aim new electronics components and boards will be installed. These electronics boards spread lot of heat that needs to be removed because of the temperature requirements that must be respected inside the cave. For this reason, an ad hoc thermal management is required. This will be based on a cooling water system that is studied here. This system has to work below the atmospheric pressure to prevent water to go outside from the circuit. To perform this, the chosen solution is the use of a thin metallic cold plate that houses a steel pipe. Inside the pipe water flows at a temperature of about 20°C. The system was designed on the dimensions of the electronics board, with a 3D modeller. The model was then manufactured and this first prototype was tested. Tests were performed to analyse the thermal behaviour of the chips and the water flow. As validation of test results, a study with the infrared camera was also done. At the end the values obtained from each experimental conditions were compared with analytical calculations and with numerical simulations. These last were made with the software ANSYS Fluent. The results obtained from the tests and the comparisons between them, are reported in this work.

1 Alice Experiment at CERN

Founded in 1954, CERN (European Organization for Nuclear Research) is one of the biggest laboratories involved in the study of matter constituents that means fundamental particles and accelerators physics. This research, made from physicists and engineers, are probing the fundamental structure of the universe. Here the particles are made to collide together at close to the speed of light. The process gives the physicists clues about how the particles interact, and provides insights into the fundamental laws of nature.

CERN is based on Accelerators and Detectors. Accelerators send beams of particles into a large circular path to increase their velocity and energy. After this acceleration, the beams are made to collide with each other or with stationary targets in fixed locations along the path: the detectors. They observe and record the results of each collision that takes place. CERN laboratory sits astride the Franco-Swiss border near Geneva. It was one of Europe's first joint ventures and now has 22 member states.

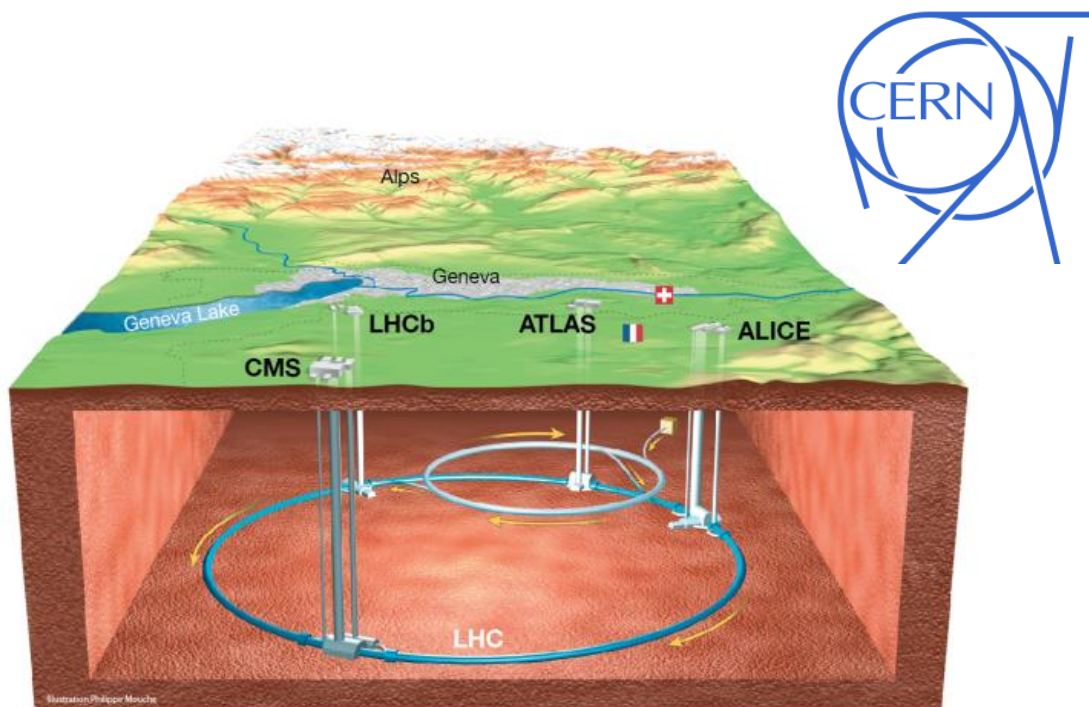


Fig. 1 Location of the particle detectors along the LHC experiment and CERN's symbol [17]

1.1 LHC

The Large Hadron Collider (LHC) is the world's largest and most powerful particle accelerator. It first started up on 10 September 2008, and remains the latest addition to CERN's accelerator complex. The LHC consists of a 27-kilometre ring of superconducting magnets with a number of accelerating structures to boost the energy of the particles along the way. Inside the accelerator, two high-energy particle beams travel at close to the speed of light before they are made to collide. The beams travel in opposite directions in separate beam pipes (two tubes kept at ultrahigh vacuum). They are guided around the accelerator ring by a strong magnetic field maintained by superconducting electromagnets. The electromagnets are built from coils of special electric cable that operates in a superconducting state, efficiently conducting electricity without resistance or loss of energy. This requires chilling the magnets to -271.3°C : a temperature colder than outer space. For this reason, much of the accelerator is connected to a distribution system of liquid helium, which cools the magnets, as well as to other supply services.

Thousands of magnets of different varieties and sizes are used to direct the beams around the accelerator. These include 1232 dipole magnets: 15 metres in length which bend the beams, and 392 quadrupole magnets, each 5-7 metres long, which focus the beams. Just prior to collision, another type of magnet is used to "squeeze" the particles closer together to increase the number of efficient collisions. The particles are so small that the task of making them collide is like firing two needles 10 kilometres apart with such precision that they meet halfway. After the acceleration, the beams inside the LHC are made to collide at four locations around the accelerator ring, corresponding to the positions of four particle detectors: ATLAS, CMS, ALICE and LHCb [Fig. 1]. In the first part of the accelerator, an electric field removes electrons from hydrogen nuclei (consisting of one proton and one electron). Electric fields along the accelerator switch from positive to negative at a given frequency, pulling charged particles forwards along the accelerator. Controls are made on the frequency of the beam injection to ensure the particles accelerate not in a continuous stream, but in closely spaced little groups. It's important that the particles do not collide with gas molecules on their journey through the accelerator, so the beam is contained in an ultrahigh vacuum inside a metal pipe called "beam pipe".

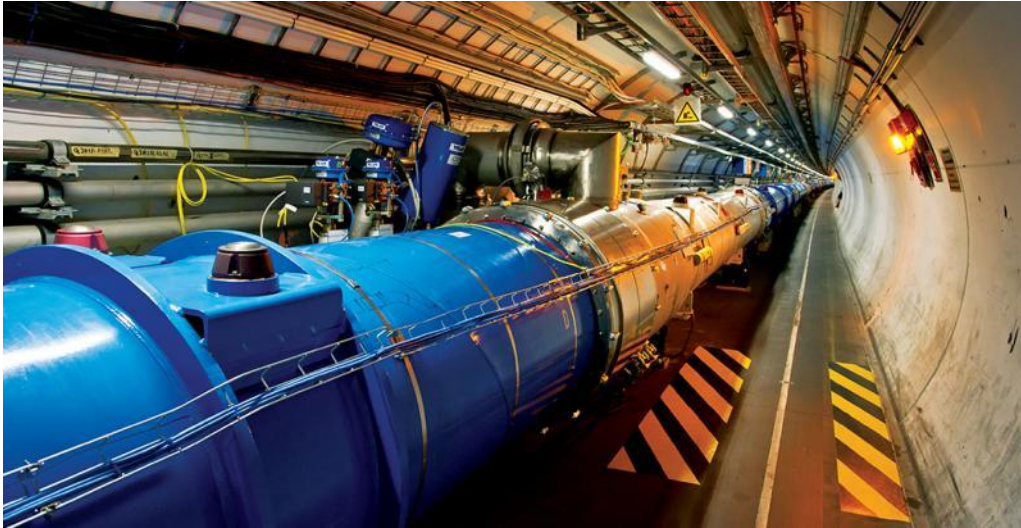


Fig. 2 LHC magnets inside the cave [17]

1.2 Particle Detectors

Particle detectors are placed in four locations around the LHC ring. The major Detectors' names are ALICE, ATLAS, CMS and LHCb; each of these investigates the behaviour of the matter. Their aim is to take data from the collisions: this data will be reworked to reveal what types of particles emerge from the collision.

Before the beams enter the LHC, particles are squeezed closer together. Along their travel they continue to be reduced in dimensions. Three quadrupoles are used for this aim. They create a system called "inner triplet". There are eight inner triplets, two of which are located at each of the four large LHC detectors. Inner triplets tighten the beam, making it 12.5 times narrower (from 0.2 millimetres down to 16 micrometres across). After the beams collide in the detector, enormous magnets aid the measurement of collisions' products. Physicists look at how charged particles are and how much bended are their trajectories through the magnetic field by calculating their momentum. In this way they can determine their identity.

After colliding, the particle beams are separated again by dipole magnets. Other magnets minimize the spread of the particles from the collisions. When it is time to stop the particles in their journey, they are deflected from the LHC along a straight line towards the beam dump. A "dilution" magnet reduces the beam intensity by a factor of 100.000 before the beam collides with a block of concrete and graphite composite for its final stop.

1.3 The ALICE experiment

ALICE (A Large Ion Collider Experiment) is one of the major experiment along the LHC. Optimized for the study of heavy-ion collisions, is designed to address the physics of strongly interacting matter, and in particular the properties of the Quark-Gluon Plasma (QGP), by colliding ions. The prime aim of the experiment is to study in detail the behaviour of nuclear matter at high densities and temperatures, where the formation of a new phase, the quark gluon plasma is expected. In these reactions the LHC's enormous energy (collisions of Pb nuclei are 100 times more energetic than those of protons) heats up the matter in the collision zone to a temperature which is 100000 times higher than the temperature in the core of our sun (15.000.000 °K). Nuclei and nucleons melt into their elementary constituents, quarks and gluons, to form for a brief instant the primordial matter which filled the universe until a few microseconds after the Big Bang. The hot reaction zone expands almost at the speed of light, and in the process cools, breaks up and condenses back into a plethora of ordinary, composite matter particles. The purpose is to carry out a comprehensive study of hadrons, electrons and photons produced in the collision of heavy nuclei. The ALICE detector consists of a central part, which measures hadrons, electrons, and photons, and a forward single arm spectrometer that focuses on muon detection. Even if ALICE is usually referred to be one of the smaller detectors, it stands 16 meters tall, is 16 m wide and 26 m long, and weighs in at approximately 10,000 tons. It has been designed and built over almost two decades by a collaboration which currently includes over 1000 scientists and engineers from more than 100 Institutes in some 30 different countries. The experiment consists of 17 different detection systems, each with its own specific technology choice and design constraints.

1.4 The Current ALICE Detector

The ALICE apparatus [Fig. 3] consists of a central barrel, a forward muon spectrometer, and a set of small detectors for triggering and event characterisation. The apparatus allows for a comprehensive study of hadrons, electrons, muons, photons and jets produced in heavy ion collisions.

Starting from a general approach, the experiment consists essentially of two main components: the central part, composed of detectors mainly devoted to the study of hadronic signals and dielectrons, and the forward muon spectrometer, devoted to the study of quarkonia behaviour. The design of the experiment has been based on the highest value: 8000 charged particles per unit of rapidity. This multiplicity dictates the granularity of the detectors and their optimal distance from the colliding beams. The central part, which covers $\pm 45^\circ$ over the full azimuth, is embedded in a large magnet with a weak solenoidal field; it covers the direction perpendicular to the beam from 45° to 135° and is located inside a huge solenoid magnet. As a warm resistive magnet, the maximum field at the nominal power of 4 MW reaches 0.5 T. The central barrel contains a set of tracking detectors, which record the momentum of the charged particles by measuring their curved path inside the magnetic field. These particles are then identified according to mass and particle type by a set of particle identification detectors, followed by two types of electromagnetic calorimeters for photon and jet measurements.

Deeping in the experiment, starting from the inner section, the detectors composing ALICE experiment are those reported in figure 3. Near the beam pipe is situated the ITS (Inner Tracking System) with the aim of understanding where the particles collide. This tracker doesn't give any indications about the identity of the particles produced during the clash. Around the ITS is located the TPC (Time Projection Chamber) that is a detector filled with gas, that provides information on the flavour composition of the collision fireball. The following cylindrical detector is TOF (Time of Flight). This detector identifies the particles by time measures: adding to this values the momentum and the

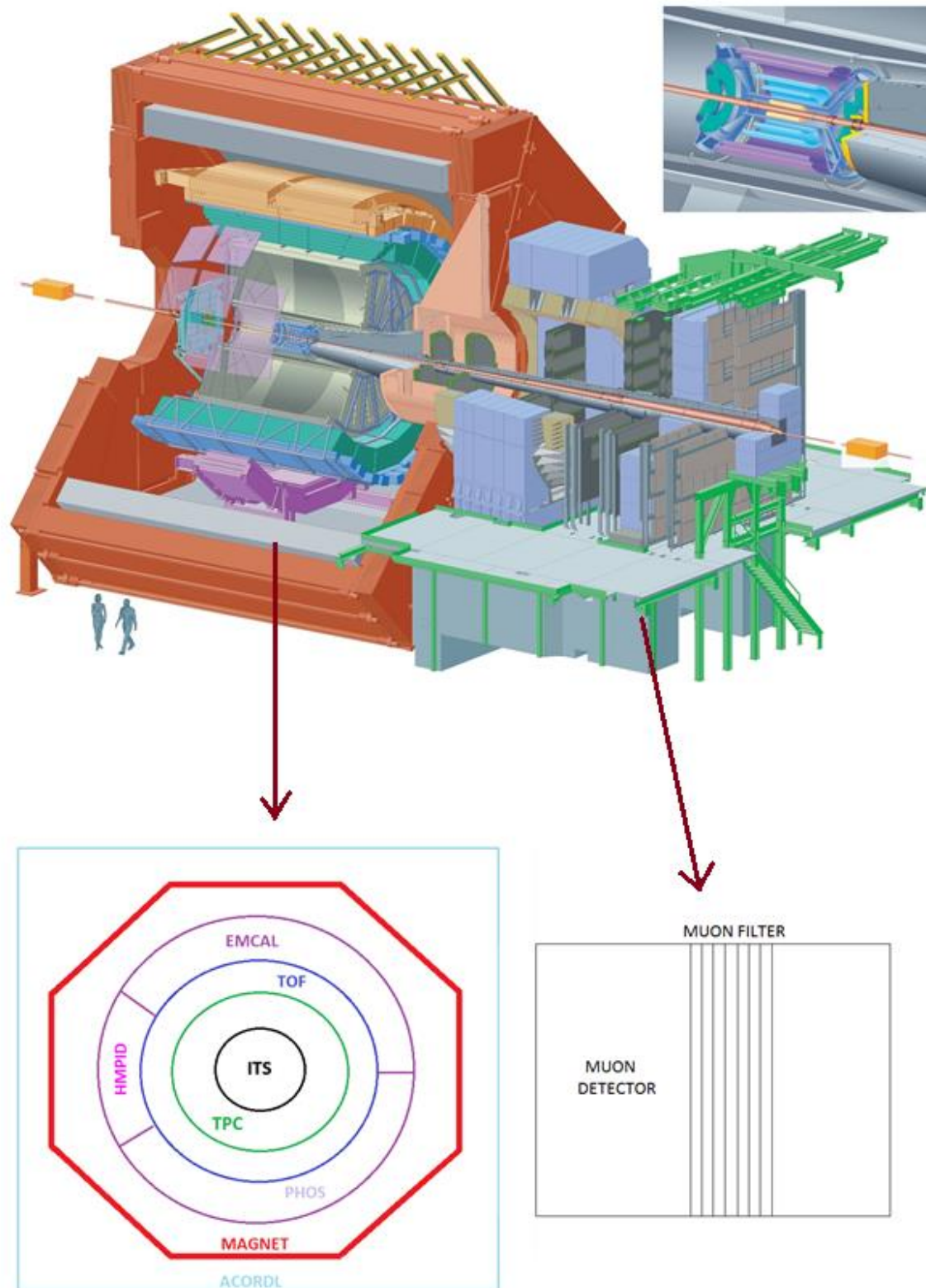


Fig.3 Illustration of the current ALICE detector and section of the whole experiment with the several detectors installed [18]

tracks length left from the particles after the collisions, it's possible to obtain the particles' mass. Around this inner section three other detector are installed: EMCal, PHOS, HMPID. EMCal is an electromagnetic calorimeter for photons detection. It acts by stopping particles and transforming them into heat. PHOS (Photon Spectrometer) is a high resolutions electromagnetic calorimeter consisting of 17920 detection channels based on leadtungstate crystals. This detector studies the initial phase of the heavy nuclei collision for understanding photons and diphotons behaviour. MPID (High Momentum Particle Identification Detector) measures the momentum range due to the heat losses of the particles during their collision. As figure 3 shows, each of this three detectors occupies only a small cylindrical sector in the same most external layer. Around this four layers, a huge magnet is installed as a shell for the other detectors. His task is to deflect particles' tracks and gives to their momentum a specify curvature angle: knowing the track left from each particle and their angular deviation is easy to define their mass. The big red magnet is locked up inside ACORDL that is a sort of shield that take into account the energy contribute brings from each particles that comes from the space. Knowing how many particles are entering the detector from the outside, is possible to subtract them to the number of particles birth during the collision. Behind the red magnet is located another detector: the Muon Detector. Is task, as the name implies, is to study the muon behaviour. It is located outside the main detector, and at one extremities because muons are not able to interact with the matter they find around them.

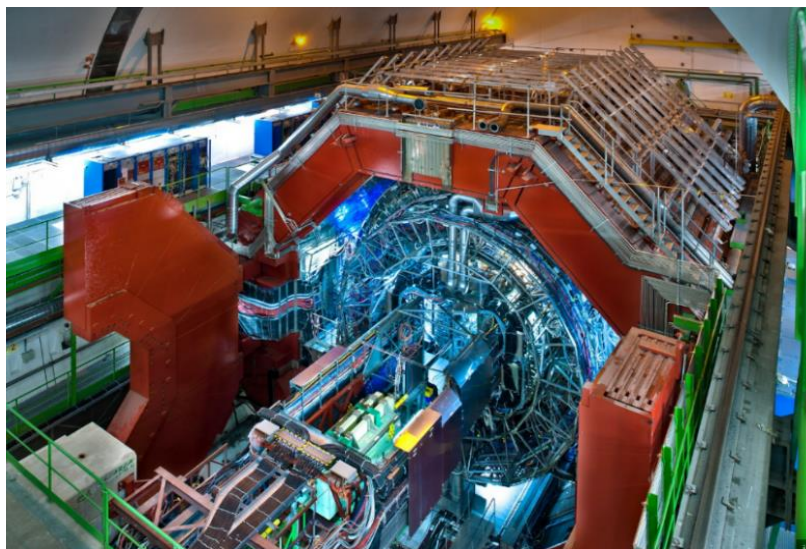


Fig. 4 ALICE detector inside the cave [18]

1.4.1 ITS

The ITS (Inner Tracking System) is the internal core of the experiment. It recognises particles containing heavy quarks by identifying the points at which they decay. The ITS consists of six cylindrical layers of silicon detectors, mounted on a support structure. The layers surround the collision point for measure the properties of the emerging particles.

The ensemble of cylindrical detectors (from inside out: ITS Pixels (ITS Drift, ITS Strips)) measures at many points the passage of each particle carrying an electric charge, so that its trajectory is precisely known. The ALICE tracking detectors are embedded in a magnetic field bending the trajectories of the particles: from the curvature of the tracks one can find their momentum. The ITS is so precise that particles with a very short life, generated during the decay of other particles, can be identified by seeing that they don't come from the point of interaction (the "vertex"), but at a distance of a tenth of millimetre from the vertex.

The ITS is composed of three systems [Fig. 5]:

- SPD (Silicon Pixel Detector)
- SSD (Silicon Strip Detector)
- SDD (Silicon Drift Detector)

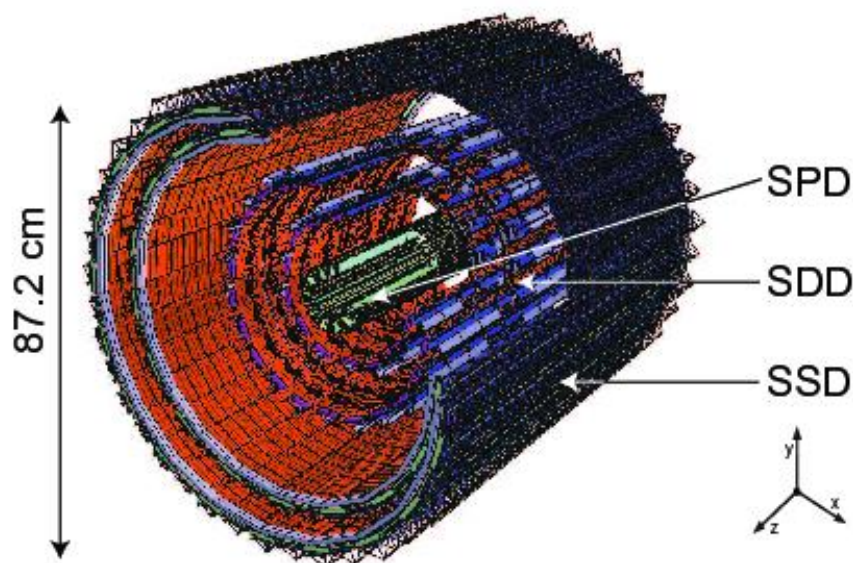


Fig. 5 Location inside the ITS of the inner detector SPD, SDD and SSD [18]

It is made of a concentric structure: two layers of pixel staves are arranged in space, at a radial distance from the beam axis of about 40 mm for the first, and 70 mm for the second. Each layer is made of stave that are pixel detectors glued on an electrical connection. The staves are glued onto 10 carbon-fibre support sectors as shown in Fig. 6. Each sector supports two staves from the first layer and four staves from the second layer. Six staves are mounted on each support. The superposition of the staves is such that no particle can go undetected. An External Shield made of Al-coated carbon fibre acts as a thermal screen towards the temperature-sensitive SDD planes and provides support and protection for the SPD barrel.

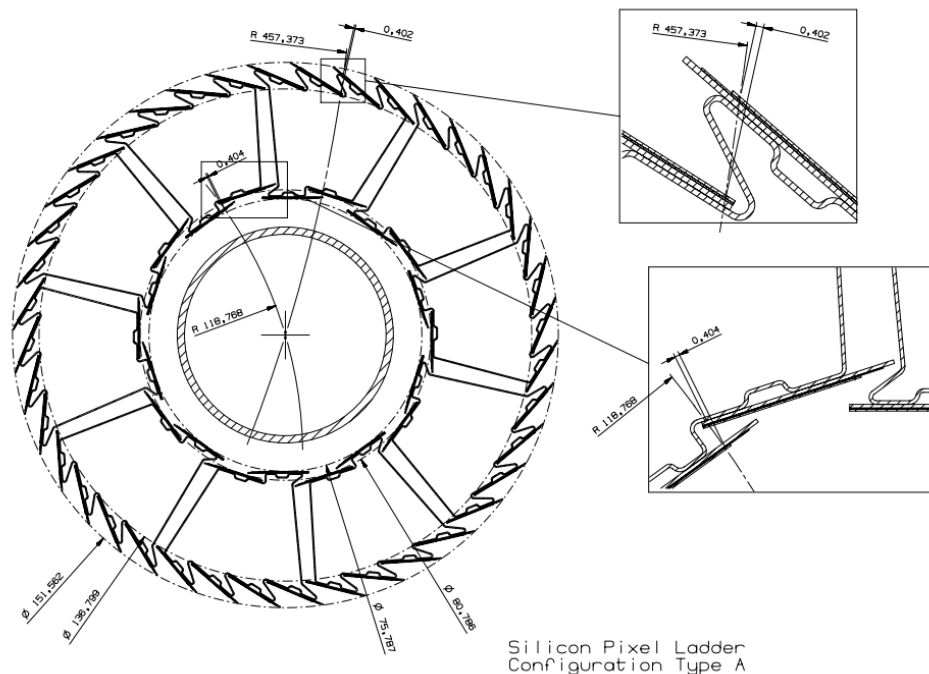


Fig. 6 Arrangement of the staves around the beam pipe [18]

1.5 The ALICE upgrade

ALICE is preparing a major upgrade of its apparatus, planned for installation in the second long LHC shutdown (LS2) in the years 2019-2020. The main physics topics require the measurement of heavy-flavour hadrons, quarkonia, and low-mass dileptons at low transverse momenta, together with new measurements of jets and their constituents. Many of these measurements in Pb-Pb collisions are characterised by a very small background signal, which are a problem for the trigger statistics. For these

measurements, the upgrade will provide an increase of statistics quality of about two orders of magnitude with respect to the initial programme. For the measurements that are currently based on rare triggers, the increase in statistics quality will be of one order of magnitude. The upgrade strategy is based on the LHC plans to increase the luminosity collisions progressively reaching instantaneous luminosity of $L = 6 \times 10^{27} \text{cm}^{-2} \text{s}^{-1}$. In the proposed plan, the ALICE upgrade include:

- A new beam pipe with smaller diameter;
- A new, high-resolution, low-material Inner Tracking System (ITS);
- Upgrade of the Time Projection Chamber (TPC), consisting of the replacement of the wire chambers with Gas Electron Multiplier (GEM) detectors and new pipelined read-out electronics;
- Upgrade of the read-out electronics of Transition Radiation Detector (TRD), Time of Flight detector (TOF), and Muon Spectrometer for high rate operation;
- Upgrade of the forward trigger detectors;
- Upgrade on the online systems and online reconstruction and analysis framework.

1.5.1 ITS upgrade

One of the future upgrade in ALICE will be made on the inner tracking system (ITS). An overview of the new ITS is reported in Fig. 7. The new ALICE core will be made of staves as the previous but the inner layers will be much closer to the particle beam. The design of the new ITS is conceived as a two-barrel structure: the Inner Barrel (IB), formed by Layers 0 to 2, and the Outer Barrel (OB), formed by Layers 3 to 6. The three Layers of the IB are also referred to as the Inner Layers, with Layers 3 and 4 as Middle Layers and Layers 5 and 6 as Outer Layers. In the azimuthal direction, each Layer is segmented in elements called Staves. The Staff, which extends over the whole length of the respective Layer, is made of carbon fibre. It contains all structural and functional components, thus making it the smallest operable part of the detector. The three Inner Layers are built with identical Staves, while the Staves of the OB Layers have a different layout due to their longer length.

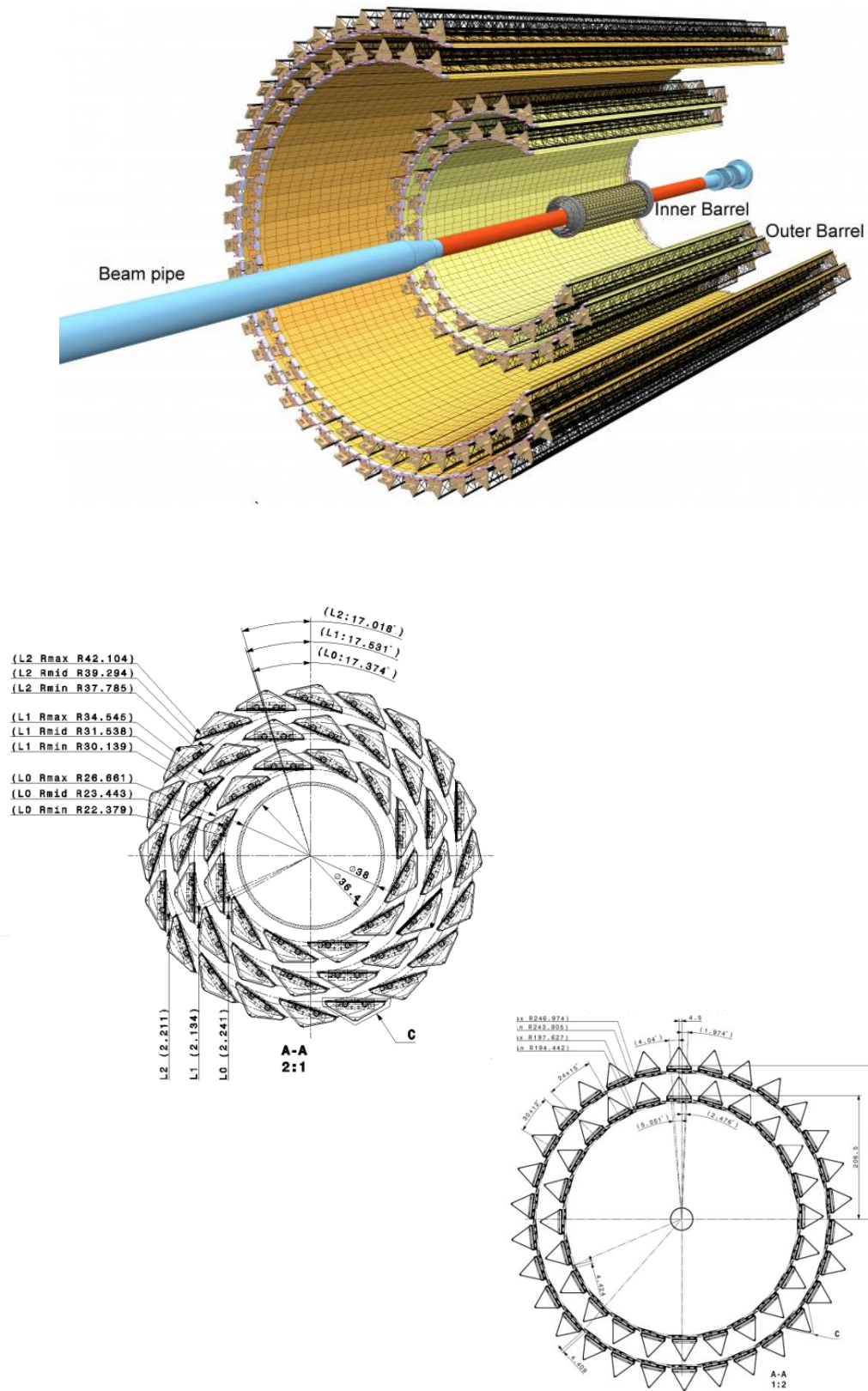


Fig. 7 New ITS design: stave location for the outer, middle and inner layers [15]

The conceptual design of both IB and OB Staves is based on the following elements:

- Space Frame: a carbon fibre support structure providing the mechanical support and the necessary stiffness;
- Cold Plate: a sheet of high-thermal conductivity carbon fibre with embedded polyimide cooling pipes, which is either integrated within the Space Frame (for the IB Staves) or attached to the Space Frame (for the OB Staves); the Cold Plate is in thermal contact with the Pixel Chips or with the Module carbon plate to remove the generated heat.
- Hybrid Integrated Circuit (HIC): an assembly of a polyimide Flexible Printed Circuit (FPC) on which a number of Pixel Chips, namely 9 and 14 for the IB and OB Staves respectively, and some passive components, are bonded;
- Module: the HIC glued to a Module carbon plate, which provides the necessary stiffness for the handling and possible replacement of a single Module in case of malfunctions;
- Half-Staff: the OB Staves are further segmented in azimuth in two halves, called Half-Staves. Each Half-Staff, extending over the full length of the Staff, consists

The design of the Staves [Fig. 8] takes into account the specifications of the new ITS. The low material budget combined with very good rigidity and stability of a relatively large structure imposes severe constraints in terms of design and technical solutions that can be implemented.

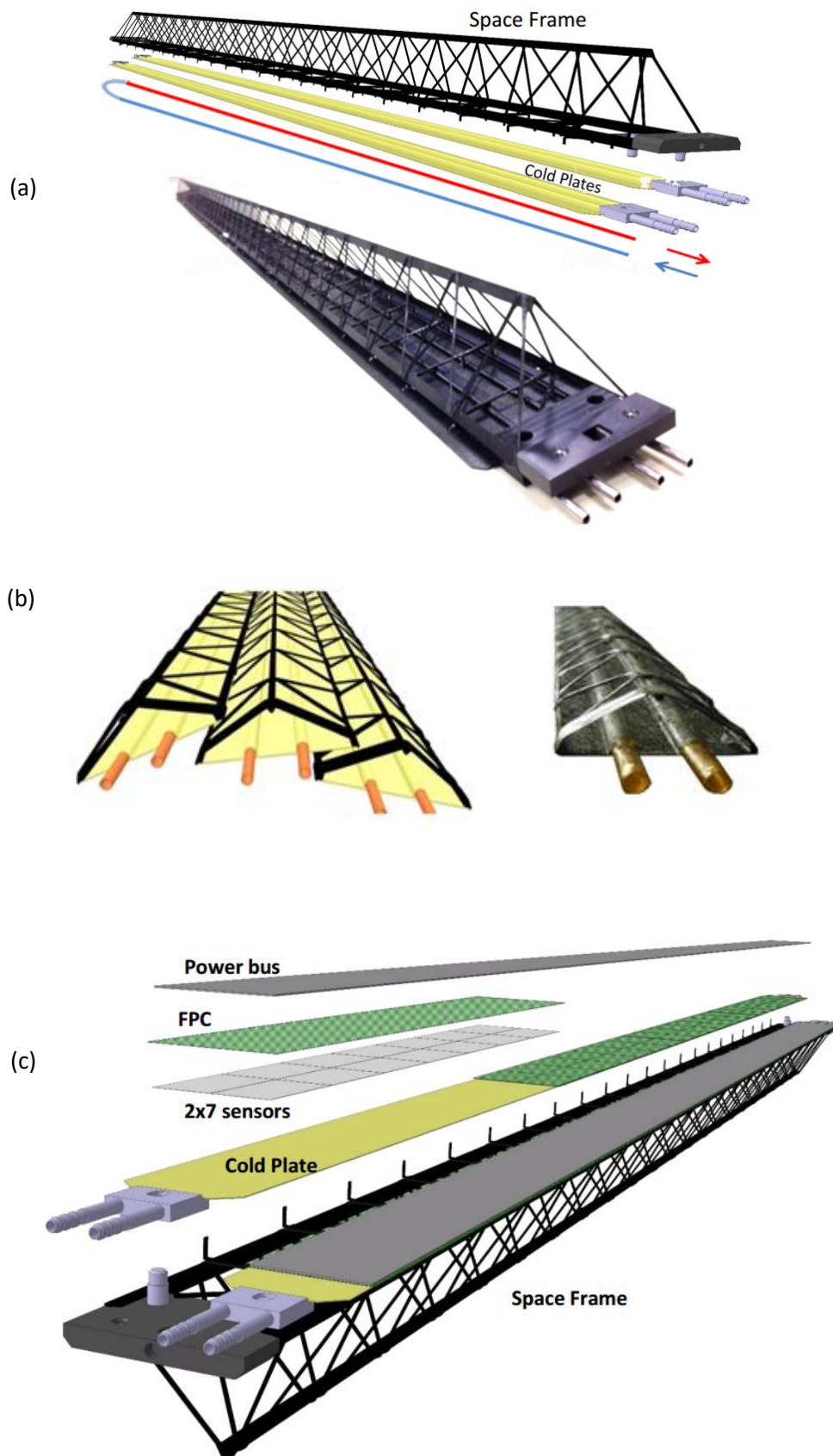


Fig. 8 Staves design: (a) carbon stave coupled with the cooling lines; (b) Stave position and prototype; (c) Stave coupled with the power supply line and pixels detectors [15]

1.5.2 ITS Off-Detector Electronics

The task of each stave is to support the main important part of the detector: the pixels. These pixels act like a camera: each time a collision takes place they capture the event producing electrical signals that are sent to electronics devices. These devices work out signals again and send them to computers. These devices are the Read Out Unit (ROU). Together with this ROU, Power Supply and Control Boards are installed. In this work only the ROU will be investigated because of the fast variation that occurs at the electronics pool in designing boards and also because the ROU is at the moment, more complete in components than the others. The chips that will be assembled on the board are already fixed, but their position is still not so fixed that means changes are possible while proceeding with the design. The role of the ROU is a sort of interface between collisions and data reading. To fulfil the aim, several basic chips are needed. The first prototype of the ROU board is the one in figure 9. The most relevant components for the computations, but also from a thermal point of view, are those who follow:

FPGA

GBTx

VTTx

The first chip [Fig. 10(a)], is a Field-Programmable Gate Array (FPGA) that is an integrated circuit designed to be configured by a customer. The FPGA configuration is generally specified using a hardware description language. FPGAs contain a lot of logic gates that can be inter-wired in different configurations.

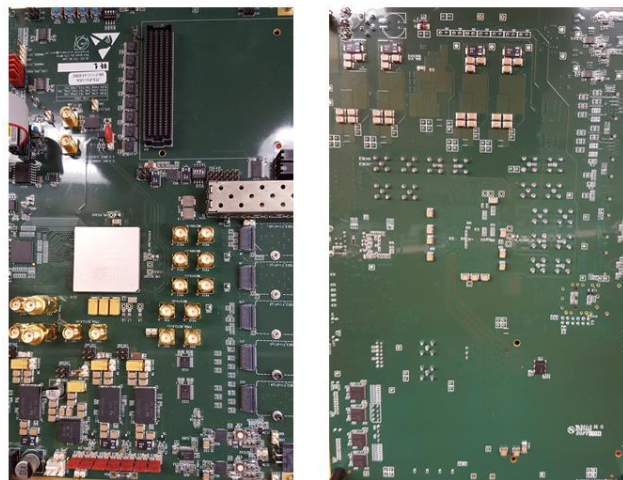


Fig. 9 Electronics board: front side on the left, back side on the right

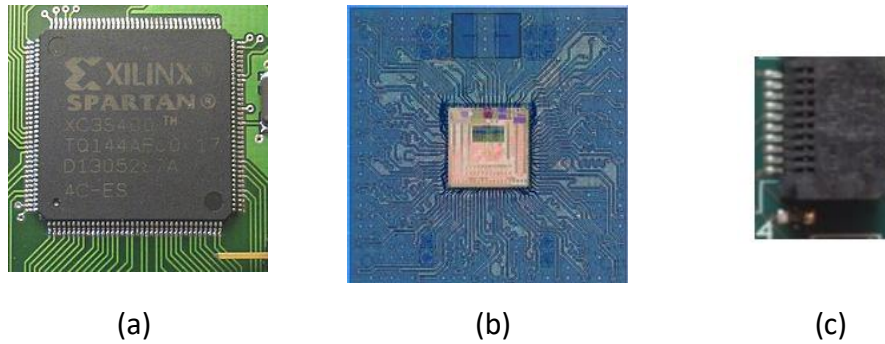


Fig. 10 Electronics chips: (a) FPGA, (b) GBTx, (c) VTTx

Logic blocks can be configured to perform complex combinational functions, or merely simple logic gates. Two of this chips will be assembling on the board, each one has a nominal power of 7.5 W. The second component, GBTx, GigaBit Transceiver [Fig. 10(b)], is a radiation tolerant chip, developed at CERN, that can be used to implement multipurpose high speed (3.2-4.48 Gb/s) bidirectional optical links for high energy physics experiments. It provides three “distinct” data paths for Timing and Trigger Control (TTC), Data Acquisition (DAQ) and Slow Control (SC) information. In practice, the three logical paths do not need to be physically separated. The aim of such architecture is to allow a single bidirectional link to be used simultaneously for data readout, trigger data, timing control distribution, and experiment slow control and monitoring. On the board there will be three GBTx each one has a nominal power of 1.2 W. VTTx is a double optical transmitter [Fig. 10(c)]. It allows adaptation of the read out bandwidth to the detector segmentation: he acts like a link between chips. On the board three of this chips will be mounted. Each of this has a nominal power of 0.75 W.

Another chip that will be considered is SCA, Slow Control Adapter. It provides several user buses to interface electronics devices. The information’s traffic arrives to this chip by passing through GBTx. Only one of this will be installed for a total nominal power of 0.1 W. For taking into account other little chips, electrical connections, connection doors etc., a percentage of the total power, estimates to be produce from the board, is used as if it was another chip with the name of “OTHER”. Its power measures 5 W. The computation of the total power produced from the board is reported in table 1.

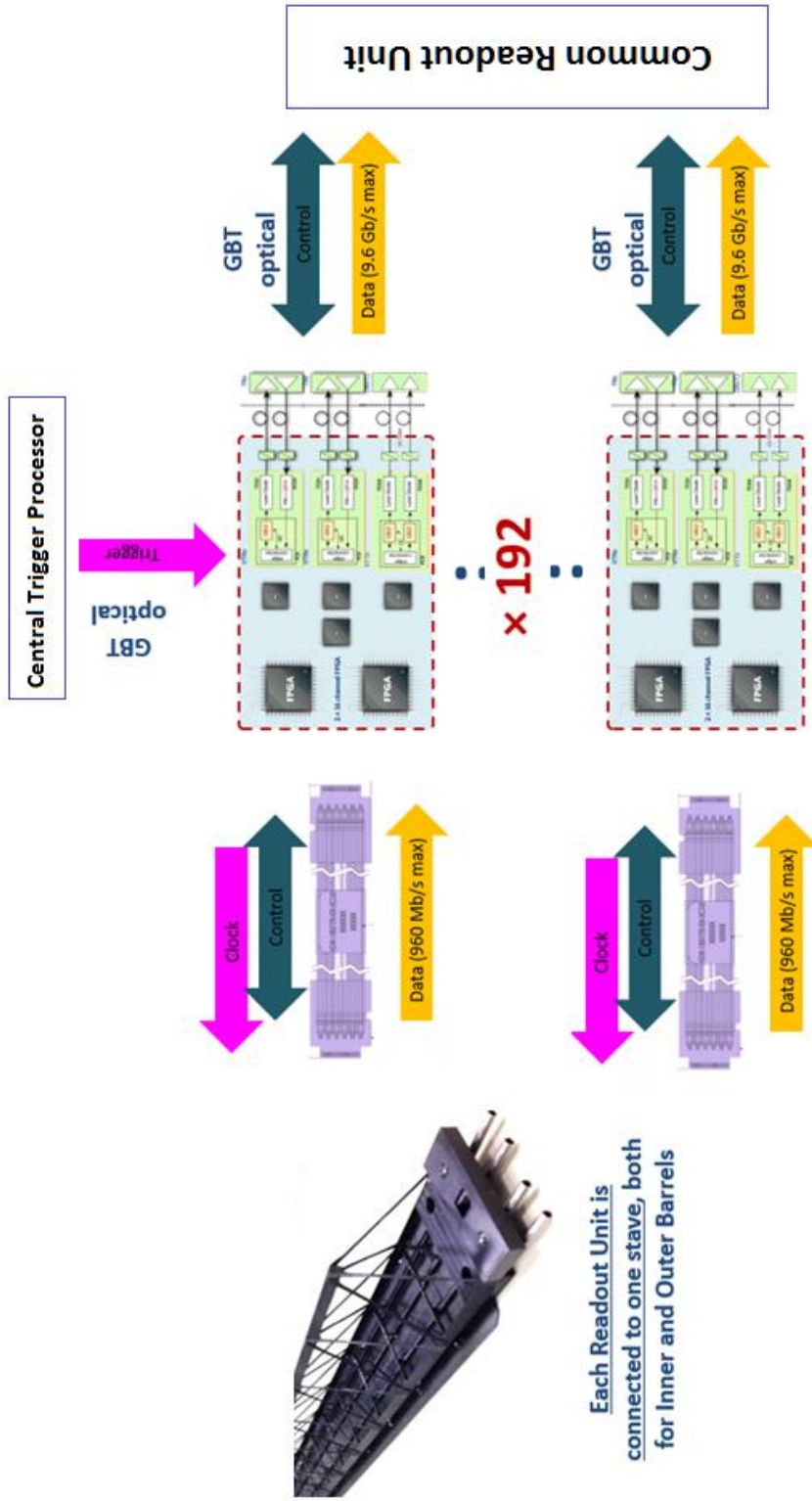


Fig. 11 Staves' electrical connections overview: starting from the left the signals taken from the pixels located on the staves, are reworked by the triggers that have to decide in few nanoseconds which data are good to be kept and which are not. After the trigger the signal go to the read out unit to be readable by a computer.

	Nominal Power [W]	n° of chips	TOT Power per chip [W]
FPGA	7.5	2	15
GBTx	1.2	3	3.6
VTTx	0.75	3	2.25
SCA	0.1	1	0.1
OTHER	5	1	5
	<i>TOT board's power:</i>		<u>25.95</u>

Tab. 1 Calculation of the total power produced by the board

The boards will be coupled with a thermal interface material on both sides of the cooling system that is studied in this work. This system will be able to host the ROU but also the PSU. It will be a thin metallic plate that cools from its inside. The boards coupled with their plate will be then housed in a closed crate. The Board and the crate can be seen in figure 12. There will be 12 crates and each one will host 16 boards for a total of 192 boards. Then the total power spread by the 192 boards will be of about 5 kW. Each crate will be provided with a water circuit that comes from the main cooling plant that will be installed in the cave. The crates have to be easy to reach because of the will to make easy the maintenance. For this reason, they will be located in the Patch Panel (Mini Frame) [Fig. 13] that is the most accessible area of the detector, the first you meet when you enter the cave.

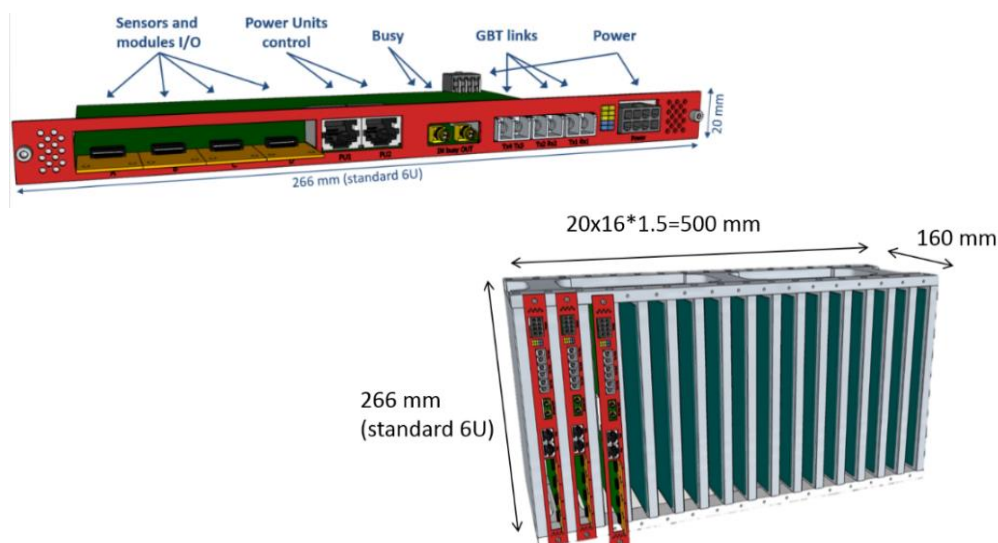


Fig. 12 Readout board (on the top) and crate (on the bottom).

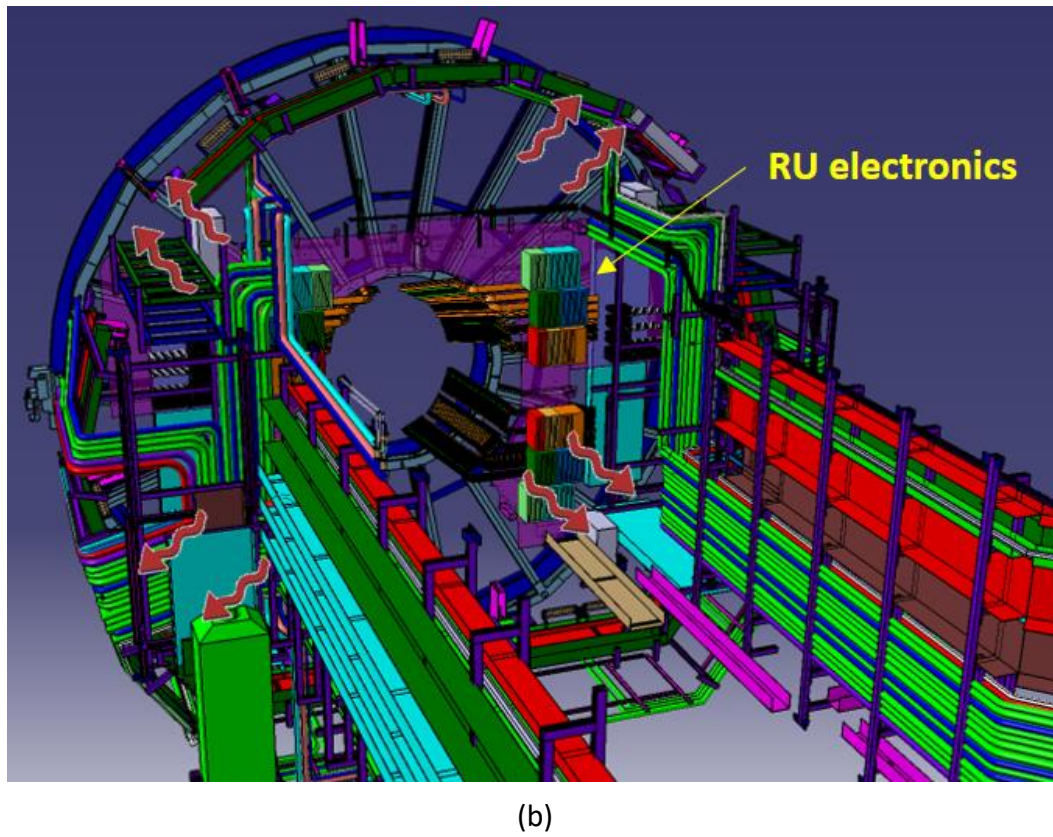
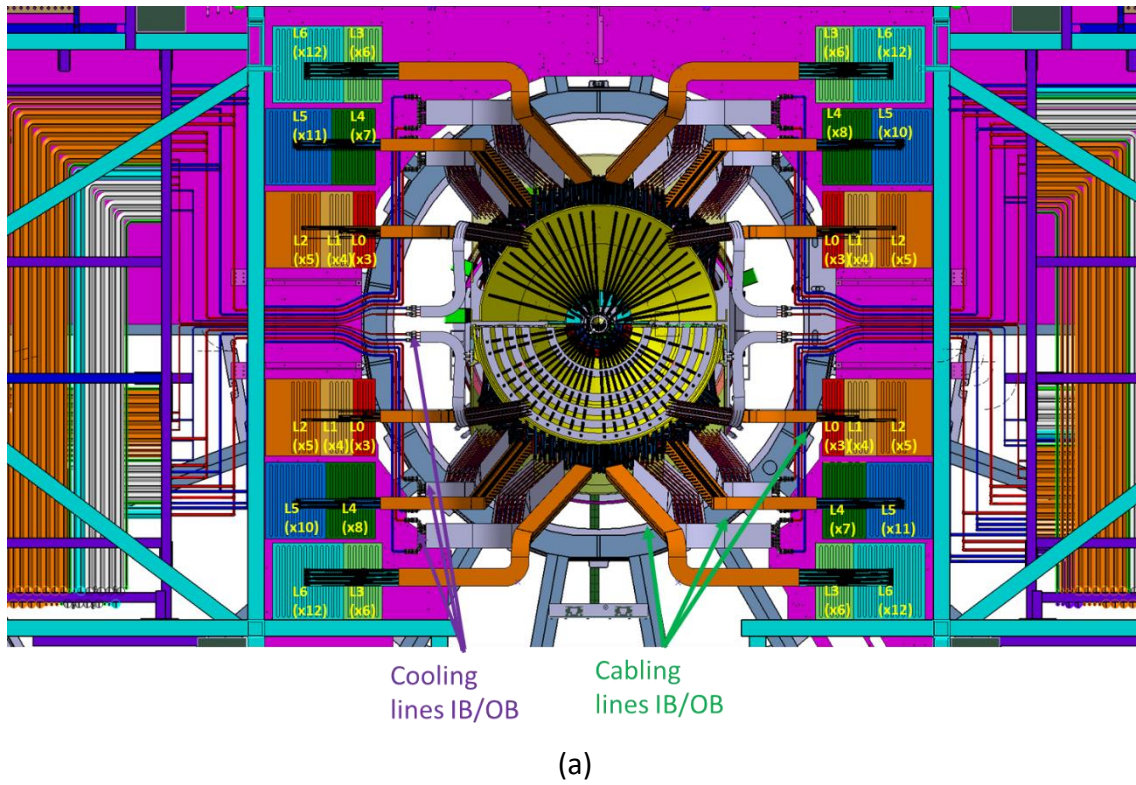


Fig. 13 Patch Panel (Mini Frame): section view (a); panel position on the detector inside the cave (b)

2 Preliminary Design

Once known the design of the ROU board, the cooling system is ready to be designed. Before dealing with the dimensioning of the cooling system, it is important to know the dimensions of the ROU board: 233.3 x 160 mm. Due to the shape of the boards, that are thin FR-4 (vetronite) plates, an appropriate cooling system is needed. For having a good heat exchange a good choice is of sure a thin plane plate cooled from its inside by water. In this way the coupling between the board and its cooling plate will be uniform and performing from a thermal and a mechanical point of view. For adding more details, more requirements need to be known.

2.1 Requirements and Boundary Conditions

The system will be cooled by water, because this was selected for the thermal management of the ITS detector and also because it is the safest fluid to use. For avoiding any interaction between water and the metal, the water has to be demineralized and has to flow in contact with steel instead of aluminium or other materials that tend to release ions when they enter in contact with fluids. As a request, the system has to work with a water flow of 11 l/h. This requirement is related to the already designed plant that will be installed in the cave. For the same reason it is important to design a system that works below the atmospheric pressure (for avoiding air to enter the circuit) with the less possible pressure drop, to stay below 0,4 bar that is the maximum drop achievable in the whole plant.

A major constraint is to save space because of the high number of electronics boards involved (192 only ROU). This means to create a plate much thin as possible. In this way good results on the thermal performances can be also obtained. Furthermore, the improvements dictated from the upgrade, request the design of a system easy to remove for maintenance and then to be repositioned once finished.

From a thermal point of view, the task is to remove from each board 51 W: 26 W from the ROU board and 25 W from the PSC boards. As explained in subchapter 2.5.2, here only the ROU is taken into account for the dimensioning and the tests. For this reason, the aim is to remove 26 W per board. While trying to do this, it is important to maintain the system below the air dew point to avoid air condensation on the components. The temperature limit request inside the cave is of 25°C. This means that the heat spread that comes from the chips, need to be removed, also because the boards will be installed inside creates and the radiative spread can be a problem if the temperature limit is the same of the room temperature.

2.2 Preliminary Layout Definition

The solution of a plane plate seems to have many positive features: permits a good coupling and also to save space. For this reasons the dimensioning starts from the width of the plate that should be within 4 mm. In this way the best solution for the cooling, is to place inside the plate a pipe made of steel that covers the largest area possible. For respecting the bond of the thickness, at first a 1-2 mm of inner diameter pipe was take into account. Looking at the possible providers, the perfect outer diameter for the aim can be of 2 or 3 mm.

Inside this range of dimensions, the shape and the dimension of the pipe inside the plate, can be now considered. Important, while doing this, is to take into account that there is a limit on the maximum pressure drop that can occurs inside the plant: 0.4 bar.

Several shapes for the pipe circuit were considered and are here reported in figure 14.

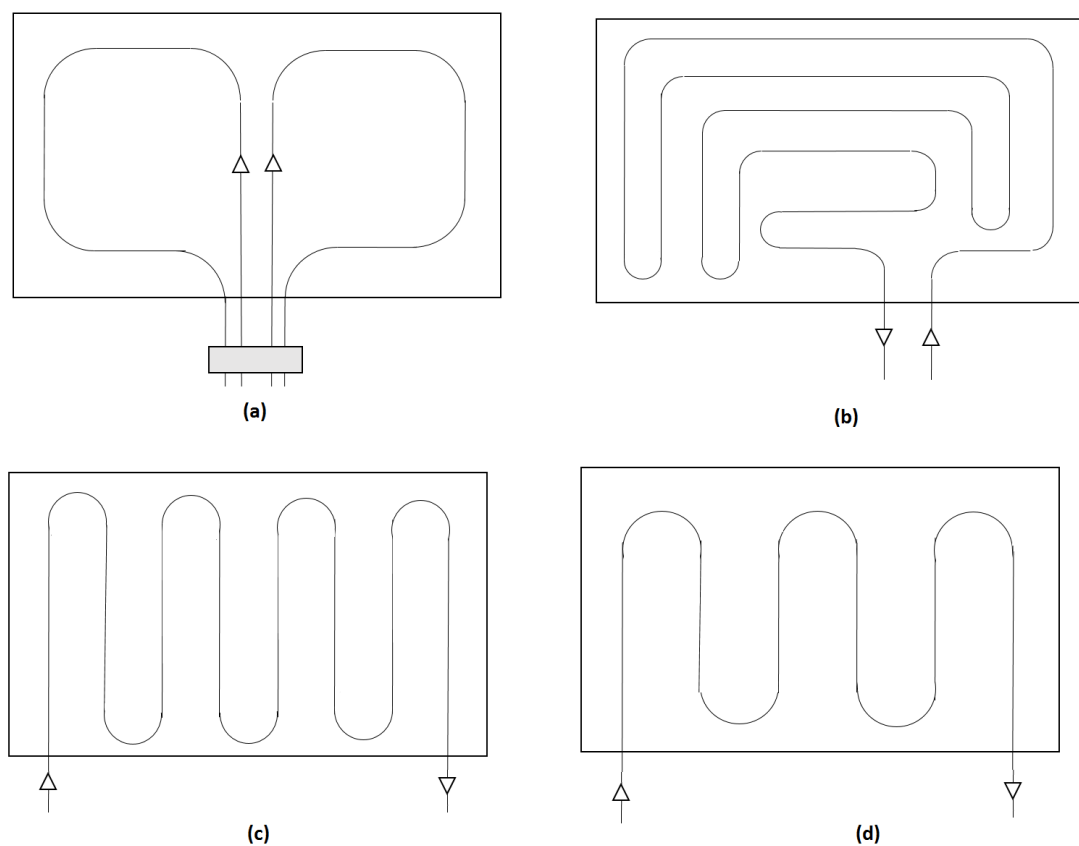


Fig. 14 Possible configurations for the pipe inside the plate

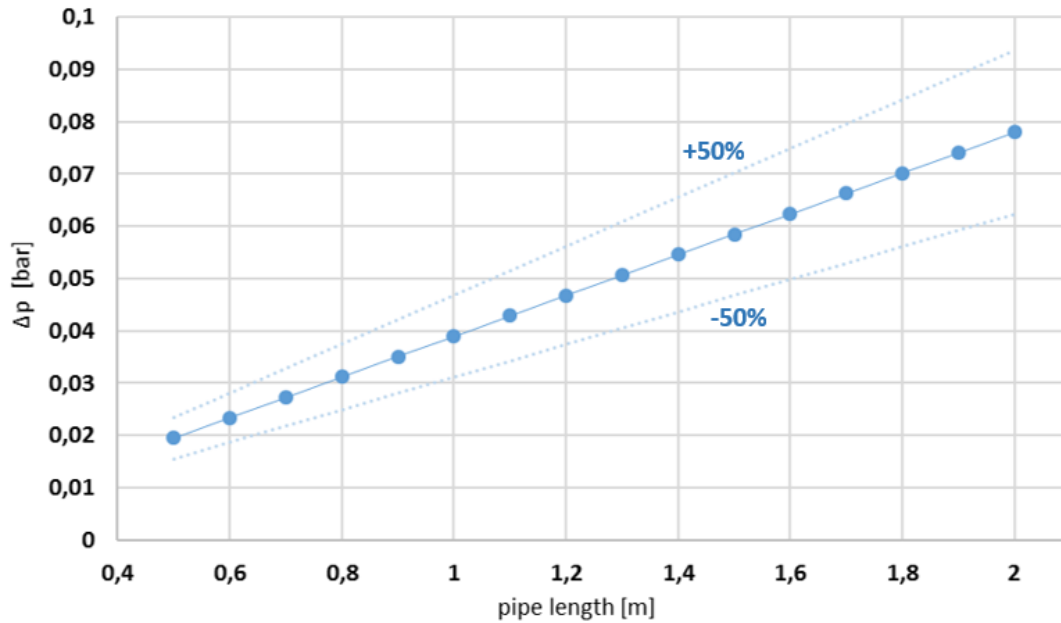


Chart 1. Water pressure drop at different pipe length

Among these proposals (b) can be discarded because of the difficulty in manufacturing. Scheme (a) can't be accounted because it needs too much water connection that means more pressure drops and more complexity in the system. Proposals (c) and (d) are basically the same but they cover a different surface; (c) would be more performing but needs to be tested on the drops. For this reason, a pressure drop calculation was made for being sure if proposal (c) can be used although the numerous curves involved.

As chart 1 shows, the limit of 0.4 bar is never reached if the pipe's length stays between 0.5 and 2 m length. For being sure, a safety factor of $\pm 50\%$ is added to drops' value.

Knowing the power dissipate and the water flow, the temperature difference between inlet and outlet can be calculates as

$$Q = m \, c_p \, \Delta T \rightarrow \Delta T = \frac{Q}{m \, c_p} = \frac{26}{0.00305 * 4184} = 2.8^\circ K$$

With 11 l/h Reynolds number is equal to 1938.64 that means a water velocity of 0.972 m/s. A fast analysis on the flow gives:

$$L_{th} = d \, Re \, Pr \, 0.05 \quad \underline{L_{th}} \quad 1.35705 \quad m$$

$$L_{id} = 0.05 \, d \, Re \quad \underline{L_{id}} \quad 0.193864 \quad m$$

The thermal and the hydraulic lengths were calculated by using the previous data assumptions. After 1.3 meter a fully developed laminar flow is assured.

From this it is understood that there are no problems between the considered configurations. For this reason, configuration (c) and (d) remain both possible. A preliminary 3D model of the plate was made by using the software SolidWorks and NX.

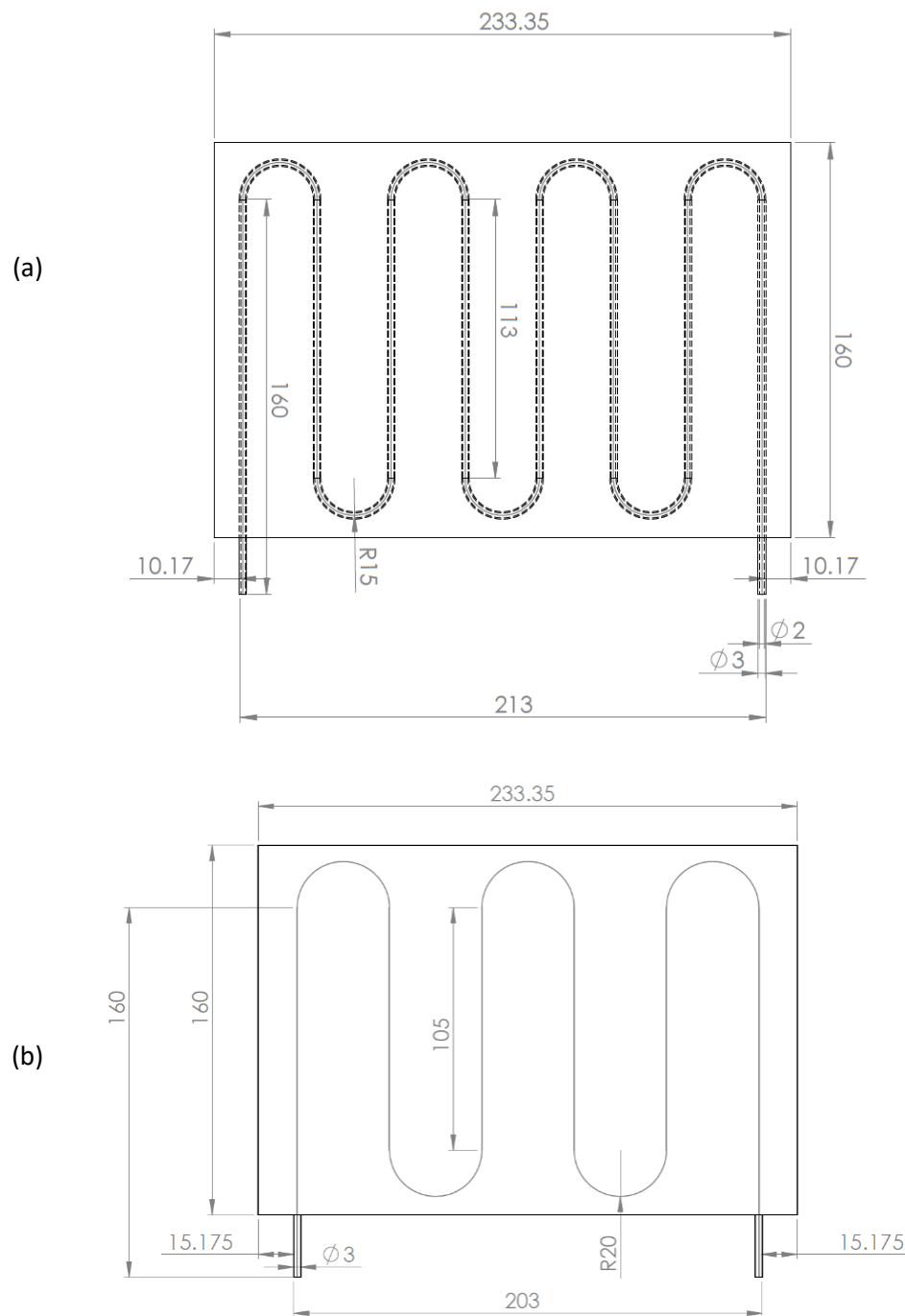


Fig. 15 Plate first possible configurations: (a) pipe with 7 curves; (b) pipe with 5 curves

For testing if there are differences between the two configurations, 5 and 7 curves, a deeper comparison of the pressure drops was done.

5 curves		7 curves	
Flow [l/h]	Pressure [bar]	Flow [l/h]	Pressure [bar]
5,5	0,04	5,5	0,05
11	0,08	11	0,10
16,5	0,12	16,5	0,15
22	0,16	22	0,21

Tab. 2 Pressure drop values at different water flows for the two configurations

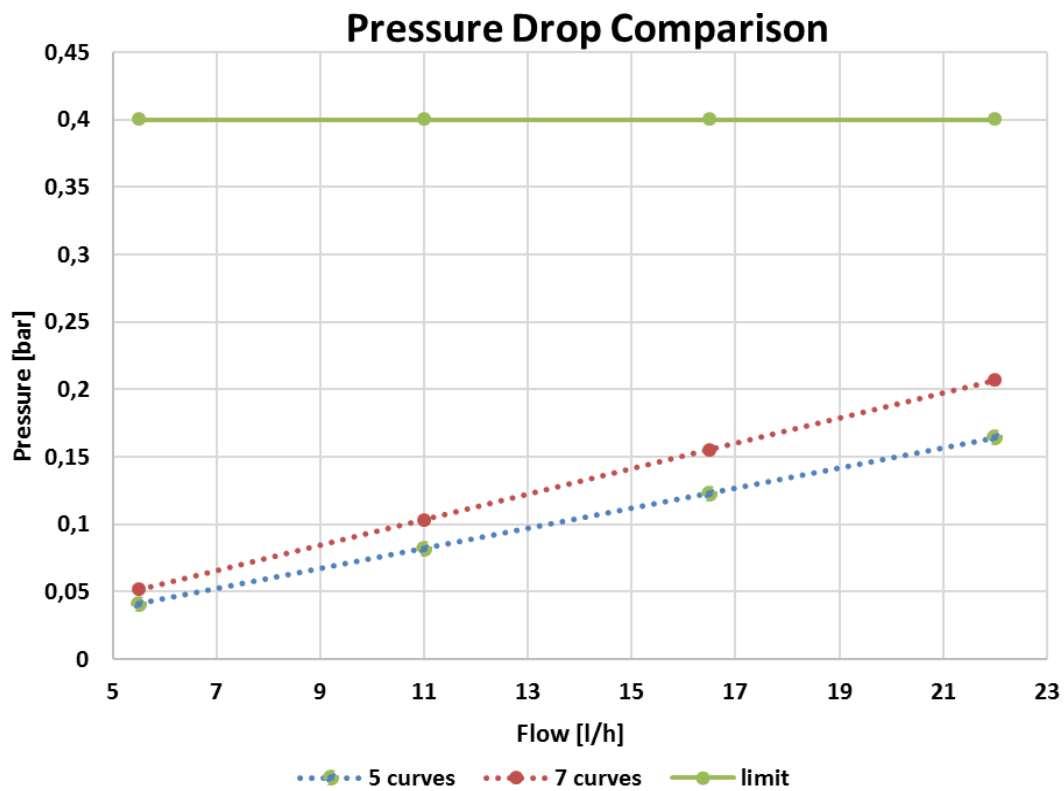


Chart. 2 Comparison of the pressure behaviour between the two possible configurations of the pipe

As chart 2 shows, with both the solutions it's possible to stay below the limit imposed from the cooling plant. For this reason, the plate with the pipe made of 7 curves can be chosen. In this way we are able to cover a larger area and then to have a better uniformity in cooling.

2.3 Thermal and Hydraulic Behaviour

Studying the behaviour of the water flow inside the pipe, emerges from Re calculations, that the water flow tends to a laminar regime for the most of the length. Here conduction and convection are both involved in the heat exchange between the chips and the water flow. Conduction is easy to be resolved with the help of a simulation tool, instead of convection that needs a deeper investigation. The theoretic study will be then use as a validation of the numerical simulation results.

Convection is one of the way in which heat transfer can take place. Convection occurs between a fluid in motion and a bounding surface, only when the two are at different temperatures. Convection is basically based on the same microscopic ways for heat transfer that occurs in conduction. The fundamental difference between convection and conduction is due to the fluid motion. The convection heat transfer mode is composed of two mechanisms: the random molecular motion (diffusion) related to the energy transfer and the macroscopic motion of the fluid, related to the energy transferred by the bulk. This motion is associated with the fact that, at any instant, large numbers of molecules move themselves collectively. Such motion in presence of a temperature gradient, contributes to the heat transfer. On the other hand, conduction appears each times the fluid stays still: energy is transmitted through particles without the macroscopic matter motion. The fluid motion can be the consequence of several phenomena (forced convection). If the motion is due to the heat exchange (that modifies the fluid properties as density and temperature) a bulk shift starts. This give birth to the so called natural convection. As known, the motion can be laminar, turbulent or in transition from the first to the second state. As shown in figure 16 the transition zone hasn't fixed characteristics as laminar or turbulent motion. For either conditions, the fluid motion is characterized by velocity component in x and y direction.

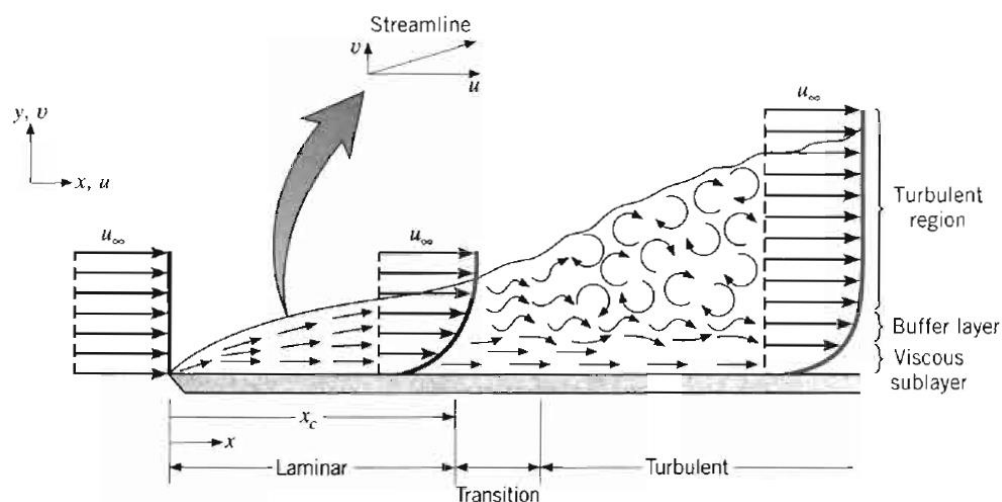


Fig. 16 Laminar to turbulent transition [1]

In laminar condition the fluid flow is high ordered and it is possible to identify streamlines along which fluid particles move. This kind of order continue until a transition zone is reached and then a switch into turbulent condition occurs. Here the flow is highly irregular and is characterized by random, three-dimensional motion. A sort of mixing between the layers where the fluid velocity is higher, and the layers where is near to zero starts. This mixing creates vortices called 'streaks' that appear and disappear irregularly. For knowing if a flow is in laminar or turbulent a dimensionless parameter, the Re number, has to be taken into account.

Generally, for a fluid flow into a circular duct:

- Laminar flow for $Re \leq 2300$
- Transition flow for $2300 \leq Re \leq 4000$
- Turbulent flow for $Re \geq 4000$

It is assumed that the transition between the two main conditions takes place at x_c , critical location, for

$$Re = \frac{\rho u x}{\mu} = 5 \times 10^5 . \quad (1)$$

2.3.1 Governing Equations

The flow motion is based on the following fundamental equations:

- Continuity Equation

$$\frac{\partial \rho}{\partial t} + \text{div}(\rho \mathbf{u}) = 0 \quad (2)$$

- Momentum Equations

$$\begin{aligned} \frac{\partial \rho u}{\partial t} + \text{div}(\rho \mathbf{u} u) &= -\frac{\partial p}{\partial x} + \text{div}(\mu \text{grad} u) + \left[-\frac{\partial T_{xx}}{\partial x} - \frac{\partial T_{xy}}{\partial y} - \frac{\partial T_{xz}}{\partial z} \right] + M_x \\ \frac{\partial \rho v}{\partial t} + \text{div}(\rho \mathbf{u} v) &= -\frac{\partial p}{\partial y} + \text{div}(\mu \text{grad} v) + \left[-\frac{\partial T_{yx}}{\partial x} - \frac{\partial T_{yy}}{\partial y} - \frac{\partial T_{yz}}{\partial z} \right] + M_y \\ \frac{\partial \rho w}{\partial t} + \text{div}(\rho \mathbf{u} w) &= -\frac{\partial p}{\partial z} + \text{div}(\mu \text{grad} w) + \left[-\frac{\partial T_{zx}}{\partial x} - \frac{\partial T_{zy}}{\partial y} - \frac{\partial T_{zz}}{\partial z} \right] + M_z \end{aligned} \quad (3)$$

- Energy Equation

$$\frac{\partial \rho e}{\partial t} + \text{div}(\rho \mathbf{e} \mathbf{u}) = -p \text{div} \mathbf{u} + \text{div}(\lambda \text{grad} T) + \Phi + H \quad (4)$$

Since these equations are really complex to resolve, lots of approximations and simplifications are necessary for having a solution. Momentum and energy transfer within a flow field subjected to some boundary conditions, are governed by the principle of conservation of mass (Newton's second law of motion) and by the laws of thermodynamics. Essential for the study of fluid flow is the Navier-Stokes differential system of equations. The system describes the fluid motion only if the fluid is a deformable continuum (it doesn't make sense for a rarefied gas). These equations are the sum of the total forces applied over an infinitesimal volume. Analytical solutions are available only by making a lot of simplifications, conversely approximated solutions can be found only with the support of calculation software. These equations are also made on fundamental equations as Newton's and Fourier's laws. It is also useful to know the Hagen-Poiseuille's law, a physical law that gives the pressure drop in an incompressible Newtonian fluid, in laminar flow, flowing through a long cylindrical pipe of constant cross section. These are the fundamental equations implemented in the simulation tools.

2.3.2 Boundary layer

The concept of the boundary layer is central to understand how the heat transfer is involved in convection. For knowing the flow behaviour in this region, several simplifications on the balance equations need to be made. Considering a fluid flow over a surface, the interaction between the fluid and the surface has, as consequence, the development of a region in the fluid through which the velocity varies and where there is also a temperature variation from T_{sup} , at the "wall", to T_{bulk} in the outer zone of the fluid flow. This region is known as boundary layer. The contribution of the random molecular motion dominates near the surface where the fluid velocity is low or tends to zero: in this region the heat is transferred only by this mechanism. The contribution of the bulk fluid motion is due to the boundary layer growth along the x direction: the heat conducted into this layer is swept downstream and is eventually transferred to the fluid outside the boundary layer.

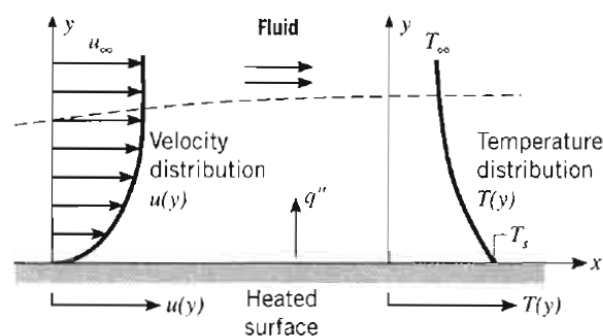


Fig. 17 Developing of velocity and thermal boundary layer [1]

The convection heat transfer process can be explained by the following equation:

$$q'' = h (T_s - T_b) \quad (5)$$

Where q'' is the convection heat flux [W/m^2], h is the convection heat transfer coefficient [$\text{W}/\text{m}^2 \text{K}$] and T_s e T_b are respectively the temperature of the surface and the bulk. The equation is presumed to be positive if the heat is transferred from the surface and negative if it is transferred to the surface. The h coefficient depends on the boundary layer condition which are influenced by the surface geometry, the nature of the fluid motion and the thermodynamic proprieties of the fluid involved.

Process	h ($\text{W}/\text{m}^2 \cdot \text{K}$)
Free convection	
Gases	2–25
Liquids	50–1000
Forced convection	
Gases	25–250
Liquids	100–20,000
Convection with phase change	
Boiling or condensation	2500–100,000

Tab. 3 Typical values for the convection heat transfer coefficient [1]

2.3.2.1 Velocity Boundary Layer

Maintaining the same assumptions used before for the geometry of the problem, when fluid particles make contact with the surface, their velocity is reduced significantly and usually is considered to be zero. These particles then act to retard the motion of the particles in the nearest layers, this last layer retard other layers and so on since this effect won't become negligible. This retard in the motion is associated with the shear stresses τ , acting in planes parallel to the fluid velocity.

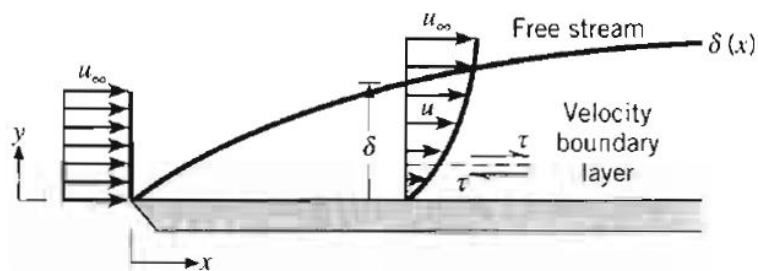


Fig. 18 Thermal boundary layer in its development along a surface [1]

With increasing distance from the surface, the velocity begins to increase till it reaches the free stream value u_∞ . δ is the boundary layer thickness and is defined as the y value for which $u=0.99 u_\infty$. From this starts the development of a region in the fluid through which the velocity varies from zero, at the surface, to infinite in the outer flow: this zone is called *hydrodynamic boundary layer*. Therefore, in this region there are high values of velocity gradient and shear stresses, but with increasing distance they become negligible.

2.3.2.2 Thermal Boundary Layer

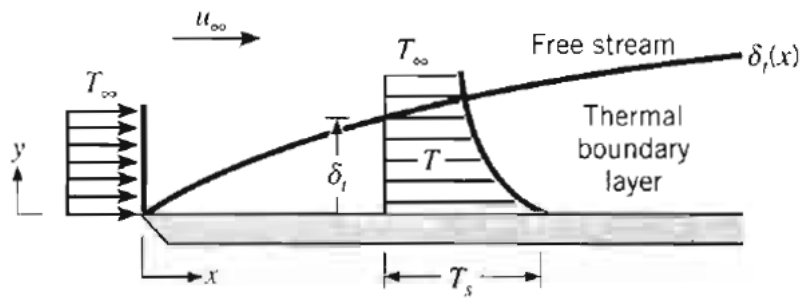


Fig. 19 Velocity boundary layer in its development along a surface [1]

If the surface and the flow are at different temperatures, there will be a region through which the temperature varies from T_{sup} , at the “wall”, to T_{bulk} in the outer zone of the fluid flow; this region is called *thermal boundary layer*. The thermal boundary layer develops if the fluid free stream and surface are at different temperature. Consider an isothermal flat plane: on the leading edge the temperature profile is uniform with $T(y) = T_\infty$. Each particle that came into contact with the heated surface, achieve thermal equilibrium at the plate’s surface temperature. In turn this particles exchange energy with those in the nearest fluid layers and temperature gradients develop in the fluid. The region into the fluid where occurs this kind of exchange is the *thermal boundary layer*. δ_t is the boundary layer thickness and is defined as the y value for which $[(T_s - T)/(T_s - T_\infty)] = 0.99$. At any distances from the leading edge, the local surface heat flux can be obtained by applying Fourier’s law to the fluid at $y=0$:

$$q_s'' = -k_f \left. \frac{\partial T}{\partial y} \right|_{y=0} \quad (6)$$

Therefore, while boundary layer thickness grows along x direction, the velocity gradient decrease. Also the shear stress τ decreases with increasing x .

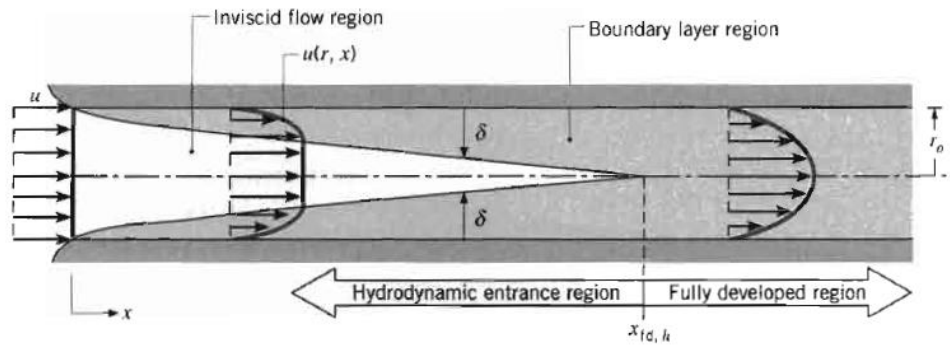


Fig. 20 Developing flow into a straight pipe: velocity profile in its development and merging of the two surfaces' boundary layers [1]

2.3.3 Internal Flow

Considering the geometry used in this work, a cylindrical pipe, the fluid flow is confined by surface. This means dealing with internal flow. For this reason, it is useful to know if the motion is laminar or turbulent, but it is more fundamental to discover at which length ends the entrance region and starts the fully developed laminar region.

Consider a laminar fluid flow inside a circular pipe of radius r_0 . When the fluid makes contact with the surface, the viscous effects become important, and the developing of the boundary layer starts along the x direction. This happens over the total internal pipe surface, which means there is an inviscid central zone inside the flow where the viscosity is negligible; this zone ends where the boundary layers merge together in the tube centerline. After the merge zone, viscous effects extend over the entire section, and the velocity profile changes with increasing x [Fig. 18]. After this point, the flow is said to be *fully developed*.

2.3.3.1 Hydrodynamic Developed Flow: Velocity Profile

The distance between the beginning point of the fully developed flow and the fluid inlet, is called *hydrodynamic entry length*. Figure 18 shows how the fully developed velocity profile is parabolic. To calculate the entry region length, the Re number and the pipe diameter are requested:

$$L_h \approx 0.05 Re D \quad [\text{m}] \quad (6)$$

This equation is based on the presumption that the fluid enters the pipe with a uniform velocity profile. Considering now a laminar flow of an incompressible fluid with constant properties in the laminar fully developed region, with this hypothesis it is possible to find an equation for the velocity profile.

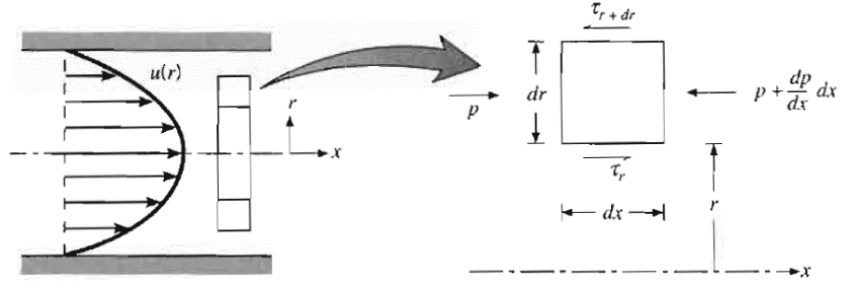


Fig. 21 Shape of the velocity profile calculated in the infinitesimal volume on the right [1]

An important feature for laminar flow is that the radial velocity component v , and his gradient on x , are everywhere equal to zero: $v = 0$, $\left(\frac{dv}{dx}\right) = 0$. Hence the radial component depends only on r $u(x,r)=u(r)$.

The force balance applied on an infinitesimal volume of fluid inside a pipe gives [Fig. 19]:

$$\tau_r(2\pi r dx) - \left\{ \tau_r(2\pi r dx) + \frac{d}{dr} [\tau_r(2\pi r dx)] dx \right\} + p(2\pi r dr) - \left\{ p(2\pi r dr) + \frac{d}{dx} [p(2\pi r dr)] dx \right\} = 0 \quad (7)$$

which is reduces to:

$$-\frac{d}{dr}(r\tau_r) = r\frac{dp}{dx} \quad (8)$$

Placing $y = r_0 - r$ the Newton's law of viscosity

$$\tau_{xy} = \tau_{yx} = \mu \left(\frac{\partial u}{\partial y} + \frac{\partial v}{\partial x} \right) \quad (9)$$

We obtain

$$\tau_r = -\mu \frac{du}{dr} \quad (10)$$

Than replacing equation (10) in equation (8), and solving:

$$\frac{\mu}{r} \frac{d}{dr} \left(r \frac{du}{dr} \right) = \frac{dp}{dx} \quad (11)$$

$$r \frac{du}{dr} = \frac{1}{\mu} \left(\frac{dp}{dx} \right) \frac{r^2}{2} + C_1 \quad (12)$$

$$u(r) = \frac{1}{\mu} \left(\frac{dp}{dx} \right) \frac{r^2}{4} + C_1 \ln r + C_2 \quad (13)$$

Assuming this boundary conditions

$$u(r_o) = 0 \quad \text{and} \quad \left. \frac{\partial u}{\partial r} \right|_{r=0} = 0 \quad (14)$$

At the end the velocity profile is obtained:

$$u(r) = -\frac{1}{4\mu} \left(\frac{dp}{dx} \right) r_o^2 \left[1 - \left(\frac{r}{r_o} \right)^2 \right] \quad (15)$$

2.3.3.2 Thermal Developed Flow

Consider a fluid with constant temperature, entering a pipe with a surface uniform temperature (imposed by an external heat flux) bigger than the fluid one. Convection heat transfer occurs and a thermal boundary layer begins to develop. In the same way we have seen before for the hydrodynamic developed region, a thermal region starts to develop till it reaches the fully developed condition at a distance from the enter that is call *thermal entry length* and is calculates as:

$$L_t \approx 0.05 Re Pr D \quad [\text{m}] \quad (16)$$

If $Pr > 1$ the hydrodynamic boundary layer develops more rapidly than the thermal layer ($x_h < x_t$), while the inverse if $Pr < 1$. The fully developed temperature profile starts at the entrance with an uniform shape and then along x direction it takes a parabolic shape, but with the opposite orientation of the hydrodynamic parabolic profile [Fig. 22].

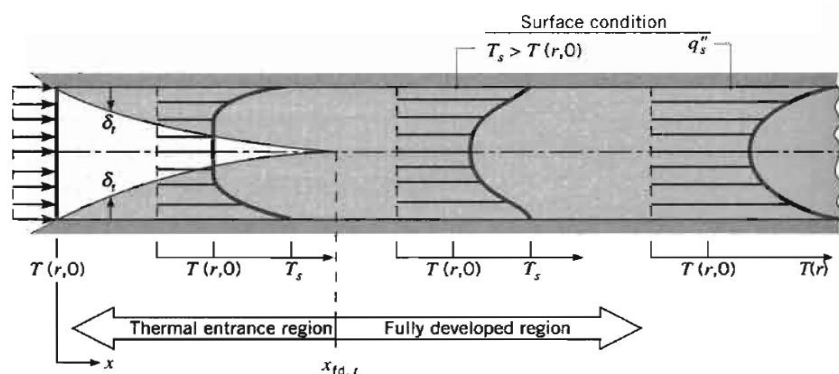


Fig. 22 Shape of the temperature profile developing inside a straight pipe [1]

2.3.4 Heat Transfer Coefficients in Fully Developed Region

A fluid flow reaches the developed region when is both thermally and hydrodynamic developed. In this region the parameters related to the convection change and

become constant. Considering a liquid flow in a cylindrical pipe, an energy balance can be written for determining the mean temperature $T_m(x)$ along the tube and for understanding in which ways the convective heat transfer is related to the difference in temperature between inlet and outlet. Assuming that the viscous dissipation is negligible and that the fluid can be modelled as an incompressible or ideal gas with negligible pressure variations. Then the thermal balance is

$$q_{conv} = m c_p (T_{m,o} - T_{m,i}) \quad (17)$$

This is a general relation that can be use irrespective of the nature of the surface type and the flow conditions.

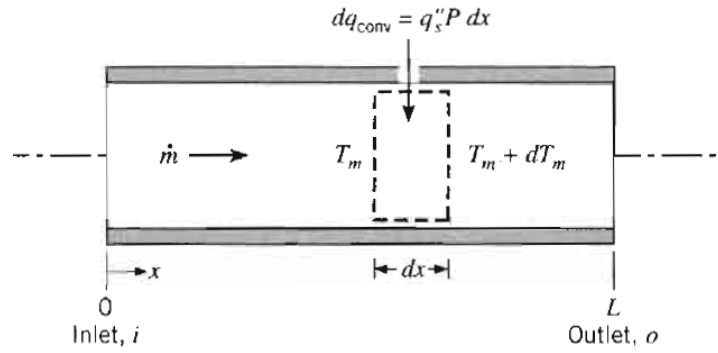


Fig. 23 Control zone in which the thermal balance is applied [1]

Applying this equation to the control volume shown in figure 19 is obtained: (18)

$$dq_{conv} = m c_p [(T_m - dT_m) - T_m]$$

Knowing that

$$dq_{conv} = q'' p dx \quad (19)$$

where p is the circular surface perimeter, the result for T_m is:

$$\frac{dT_m}{dx} = \frac{q'' p}{m c_p} = \frac{p}{m c_p} h(T_s - T_m) \quad (20)$$

2.3.4.1 Constant Surface Heat Flux

For constant q'' the previous equation has the middle expression that is constant too and becomes

$$\frac{dT_m}{dx} = \frac{q''p}{m c_p} \neq f(x) \quad (21)$$

Integrating from $x=0$ it follows that

$$T_m(x) = T_{m,i} + \frac{q''p}{m c_p} x \quad (22)$$

The mean temperature varies along the tube. It is also expected that $(T_s - T_m)$ varies with x . This difference is initially small (due to the large value of h near the entrance) but increases with increasing x due to the decrease of h that occurs as the boundary layer develops. In the fully developed region h is independent of x : it follows that in this region $(T_s - T_m)$ must also be independent of x . This is show in figure 24.

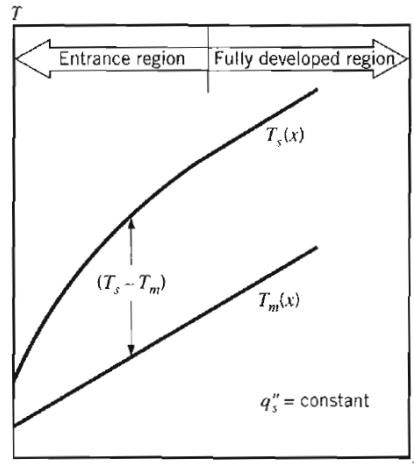


Fig. 24 Temperature difference between the bulk and the surface, along a pipe with constant heat flux applied on it [1]

In this condition (developed flow and q'' constant), the asymptote for the local Nusselt number at a point located at a distance x from the pipe inlet is given by $Nu = 4.36$. This is the value reachable in laminar fully developed flow. If the flow is still developing thermally and has been developed hydro dynamically, the asymptote for Nu number is

$$Nu = 1.302 \sqrt{Re Pr \frac{d}{x}} \quad (23)$$

Local Nusselt number is than in the range between the two asymptotes determinate numerically by Shah and London. To obtain the local Nusselt number in the entire range the following equation has to be used.

$$Nu = \left\{ 4.364^3 + 1 + \left[1.953 \sqrt[3]{Re Pr \frac{d}{l}} \right]^3 \right\}^{\frac{1}{3}} \quad (24)$$

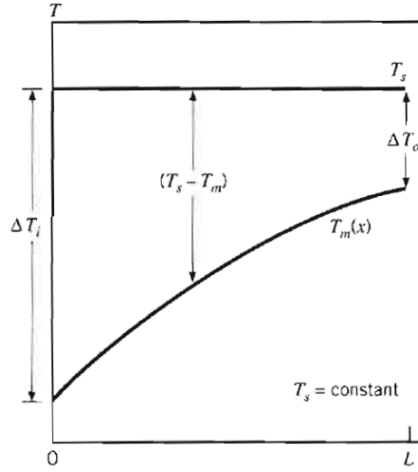


Fig. 25 Temperature difference between the bulk and the surface, along a pipe with constant wall temperature [1]

2.3.4.2 Constant Wall Temperature

Considering a constant temperature on the pipe surface equation 20 can be written as

$$\frac{dT_m}{dx} = -\frac{d(\Delta T)}{dx} = \frac{p}{m c_p} h \Delta T \quad (25)$$

Integrating from the tube inlet to the tube outlet and writing the equation for a general surface along the tube it results

$$\frac{T_s - T_{m,o}(x)}{T_s - T_{m,i}} = \exp\left(-\frac{p x}{m c_p} h'\right) \quad (26)$$

where h' is now the average value of h from tube inlet to x . This equation tells that the temperature difference $(T_s - T_m)$ decays exponentially with distance along the tube. This is shown in figure 23. The asymptote for the local Nu number at a point x , is given in this case (developed flow and constant wall temperature) by $Nu = 3.66$ for small values of $Re Pr (d/x)$, and

$$Nu = 1.077 \sqrt[3]{Re Pr \frac{d}{l}} \quad (27)$$

for high values of $Re Pr (d/x)$. To obtain the local Nusselt number in the entire range the following equation needs to be used.

$$Nu = \left\{ 3.66^3 + 0.7^3 + \left[1.615 \sqrt[3]{Re Pr \frac{d}{l}} \right]^3 \right\}^{\frac{1}{3}} \quad (28)$$

2.3.5 Pressure Drop in Fully Developed Region

The following considerations make sense only if it is assumed to work with a continuum Newtonian fluid. Considering the equilibrium of a fluid element of length dx in a pipe of diameter D , the force due to the pressure difference dp is balanced by the frictional force due to the shear stress τ at the wall

$$\left(\frac{\pi}{4}D^2\right) dp = (\pi D dx) \tau \quad (29)$$

The pressure gradient and the wall shear stress are then related by

$$\frac{dp}{dx} = \frac{4\tau}{D} \quad (30)$$

In these equation τ is defined as

$$\tau = \mu \frac{du}{dy} \quad (31)$$

where μ is the dynamic viscosity. From this parameter another important dimensionless factor called *friction coefficient* is obtained. It's uses in heat transfer because it represents the momentum transfer process of the fluid flow. In literature lots of different formulations for this factor can be found. The coefficient is called *Fanning friction coefficient* and is defined as

$$f = \frac{\tau}{\frac{1}{2} \rho u_m^2} \quad (32)$$

where u_m is the mean flow velocity in the channel. This factor depends on flow conditions, the channel wall geometry and on the surface conditions: laminar or turbulent flow; fully developed, or not, flow; smooth or rough wall.

For fully developed laminar f can be defined with the help of the Poiseuille and Reynolds number as follows

$$f = \frac{Po}{Re} \quad (33)$$

It can be seen that for a circular pipe $Po = f Re = 16 \rightarrow f = \frac{16}{Re}$.

The related pressure drop Δp over a length L is obtain from the following equation

$$\Delta p = \frac{2fL\rho u_m^2}{D} \quad (34)$$

Working with the *Moody (or Darcy) friction factor* (not a friction coefficient) there is also:

$$f_D = \frac{-\frac{dp}{dx} D}{\rho \frac{u^2}{2}} \quad (35)$$

this factor for fully developed laminar flow, gives by Hagen-Poiseuille equation is than

$$f_D = \frac{64}{Re} \quad (36)$$

The Darcy friction factor f is four times the Fanning factor f_D :

$$f_D = 4f \quad (37)$$

2.3.6 Entry Region

If either or both profiles are not fully developed, the flow is said to be in the *entry region*. The energy balance becomes more complicate due to the presence of the radial component of the flow velocity. Two different ways for the balance solution of this region have been obtained. The simplest solution resolves the *entry length problem*, and it assumes a fully developed velocity profile. This kind of situation can appear when there is an unheated starting length before the heat transfer region starts. In contrast the *combine entry length problem* corresponds to the case for which the temperature and velocity profiles develop simultaneously. It would never be the case that thermal conditions are fully developed and hydrodynamic condition are developing: since the temperature distribution depends on the velocity distribution, as long as the velocity is still changing, thermal conditions cannot be fully developed.

2.3.7 Heat Transfer Coefficients in the Entry and Developing Region

There are two possibilities to find a solution for the thermal balance. The first look goes to the so called entry length problem. Is necessary to introduce G_z as

$$G_z = \frac{d}{x} Re Pr \quad (38)$$

The solution at this problem presented from Kays is than

$$Nu = 3.66 + \frac{0.0668 G_z}{1 + 0.04 G_z^{2/3}} \quad (39)$$

This value is obtained assuming T_s constant and $Pr \geq 5$ in the entry length. For the solution of the combined entry problem Baehr and Stephan recommended the following formula

$$Nu = \frac{\frac{3.66}{\tanh(2.264 G_z^{-\frac{1}{3}} + 1.7 G_z^{-\frac{2}{3}})} + 0.0499 G_z \tanh(G_z^{-1})}{\tanh(2.432 Pr^{\frac{1}{6}} G_z^{-\frac{1}{6}})} \quad (40)$$

This solution is obtained assuming T_s constant and $Pr \geq 0.1$ in the entry length.

After the entrance, in the following region, while velocity profile is developing, heat is transferred and the temperature profile also starts to build up. Boundary layers are thus formed. The local Nusselt number can be determined from

$$Nu = 0.332 \sqrt[3]{Pr} \sqrt{Re \frac{d}{x}} \quad (41)$$

$$Nu = \frac{1}{2} \left(\frac{2}{1 + 22Pr} \right)^{\frac{1}{6}} \left(Re Pr \frac{d}{x} \right)^{\frac{1}{2}} \quad (42)$$

The factor 0.332 is in good approximation for $Pr > 0.1$. These two equations are for high values of d/x . As the length of the flow path becomes greater, d/x becomes progressively less, and higher values for Nu are obtained.

Next equation allows to find the Nusselt number at any point along the pipe, in which the laminar flow is developing thermally and hydro dynamically

$$Nu = \left\{ 3.66^3 + 0.7^3 + \left[1.077 \sqrt{Re Pr \frac{d}{x}} - 0.7 \right]^3 + \frac{1}{2} \left(\frac{2}{1 + 22Pr} \right)^{\frac{1}{6}} \left(Re Pr \frac{d}{x} \right)^{\frac{1}{2}} \right\}^{\frac{1}{3}} \quad (43)$$

If there is only thermal developing flow the local heat transfer is calculated by the Shah-London's equation (1987):

$$Nu = 4.363 + 8.68 (10^3 x^*)^{-0.506} e^{-41x^*} \quad (44)$$

where $x^* = x/Re d$. The equation is based on the thermal length ($L_t = c Re Pr d$ with $c=0.05$ for circular channels). Anyway in literature there are lots of different formulations for Nusselt number, obtained from experimental works or data fitting. Some of these are reported in table 4.

Laminar Forced Convection Correlations in Smooth Straight Circular Ducts

No.	References	Correlation	Limitations and Remarks
1.	Nusselt–Graetz [1,2]	$Nu_T = 1.61(Pe_b d/L)^{1/3}$ $Nu_T = 3.66$	$Pe_b d/L > 10^3$, constant wall temperature. $Pe_b d/L < 10^2$, fully developed flow in a circular duct, constant wall temperature.
2.	Schlünder [3]	$Nu_T = [(3.66)^3 + (1.61)^3 Pe_b d/L]^{1/3}$	Superposition of two asymptotes given in No. 1 for the mean Nusselt number. $0.1 < Pe_b d/L < 10^4$.
3.	Hausen [4]	$Nu_T = 3.66 + \frac{0.19(Pe_b d/L)^{0.8}}{1 + 0.117(Pe_b d/L)^{0.467}}$	Thermal entrance region, constant wall temperature. $0.1 < Pe_b d/L < 10^4$.
4.	Nusselt–Graetz [1,2]	$Nu_T = 1.953(Pe_b d/L)^{1/3}$ $Nu_H = 4.36$	$Pe_b d/L > 10^2$, constant heat flux. $Pe_b d/L < 10$, fully developed flow in a circular duct, constant heat flux.
5.	Pohlhausen [6]	$Nu_T = 0.664 \frac{1}{(Pr)^{1/6}} (Pe_b d/L)^{1/2}$	$Pe_b d/L > 10^3$, $0.5 < Pr < 500$, simultaneously developing flow.
6.	Stephan [8]	$Nu_T = Nu$ $+ f(d_0/D_i) \frac{0.19(Pe D_h/L)^{0.8}}{1 + 0.117(Pe D_h/L)^{0.467}}$ $\phi(d_0/D_i) = 1 + 0.14(d_0/D_i)^{-1/2}$ $\phi(d_0/D_i) = 1 + 0.14(d_0/D_i)^{0.1}$	Circular annular duct, constant wall temperature, thermal entrance region. Outer wall is insulated, heat transfer through the inner wall. Heat transfer through outer and inner wall.
7.	Sieder and Tate [11]	$Nu_T = 1.86(Re_b Pr_b d/L)^{1/3} (\mu_b/\mu_w)^{0.14}$	Thermal entrance region, constant wall temperature, $0.48 < Pr_b < 16,700$, $4.4 \times 10^{-3} < (\mu_b/\mu_w) < 9.75$, $(Re_b Pr_b d/L)^{1/3} (\mu_b/\mu_w)^{0.14} > 2$.
8.	Oskay and Kakaç [13]	$Nu_H = 1.86(Re_b Pr_b d/L)^{1/3} (\mu_b/\mu_w)^{0.152}$	Thermal entrance region, constant wall heat flux, for oils $0.8 \times 10^3 < Re_b < 1.8 \times 10^3$, $1 < (T_w/T_b) < 3$.
9.	Kuznetsova [14]	$Nu_H = 1.23(Re_b Pr_b d/L)^{0.4} (\mu_b/\mu_w)^{1/6}$	Thermal entrance region, constant heat flux, $400 < Re_b < 1900$, $170 < Pr_b < 640$, for oils.
10.	Test [15]	$Nu_b = 1.4(Re_b Pr_b d/L)^{1/3} (\mu_b/\mu_w)^n$	Thermal entrance region, $n = 0.05$ for heating liquids, $n = 1/3$ for cooling liquids.

Tab. 4 Different equations for evaluating Nusselt number in different condition of the fluid regime [1]

2.3.8 Pressure Drop in Developing Region

The pressure gradient in a small diameter channel is quite high. To account the non-developed flow, is used in literature an apparent friction factor f_{app} : it represents an average value of the friction factor over the flow length between the entrance section and the location under consideration. Then the pressure drop is expressed as

$$\Delta p = \frac{2 f_{app} \rho u_m^2 x}{D_h} \quad (45)$$

where D_h is the hydraulic diameter.

The difference between the apparent friction factor over a length x and the fully developed friction factor is expressed in terms of an incremental pressure defect $K(x)$:

$$k(x) = (f_{app} - f) \frac{4x}{D_h} \quad (46)$$

2.3.9 Pressure Drop in Bends

The total pressure drop in a bend is the sum of the frictional head loss due to the length of the bend, head loss due to curvature and head loss due to excess pressure drop in the downstream pipe because of the velocity profile distortion. A total loss coefficient can be defined as

$$\Delta p = K \frac{\rho u_m^2}{2} \quad (47)$$

where

$$K = \frac{4L f_c}{D_h} = \frac{4L f}{D_h} + K^* \quad (48)$$

and f_c is the bend friction factor, f is the friction factor for a straight pipe at the Reynolds number in the bend, and K^* represents a combined loss coefficient other than friction loss. To calculate f_c in a smooth bend of any degree $<360^\circ$:

$$\begin{aligned} f_c &= 5 Re^{-6,5} (R/a)^{-0,175} & \text{for } 50 < De \leq 600 \\ f_c &= 2,6 Re^{-0,55} (R/a)^{-0,225} & \text{for } 600 < De \leq 1400 \\ f_c &= 1,25 Re^{-0,45} (R/a)^{-0,275} & \text{for } 1400 < De \leq 5000 \end{aligned} \quad (49)$$

For turbulent flow, is recommended the use of the following loss coefficient K^* :

$$K^* = B(\varnothing)[0,051 + 0,38 (R/a)^{-1}] \quad (50)$$

where

$$B(\varnothing) = \begin{cases} 1 & \text{for } \varnothing = 90^\circ \\ 0,9 \sin \varnothing & \text{for } \varnothing \leq 70^\circ \\ 0,7 + 0,35 \sin(\varnothing/90) & \text{for } \varnothing \geq 70^\circ \end{cases} \quad (51)$$

3 Numerical Simulation of Partial Channel

The purpose of this chapter is to find a valid way to create a mesh for the water laminar flow, with ANSYS Workbench. The final aim is to compare among them, several types of meshes to choose, after a validation, one to apply at the entire water flow inside the board's pipe.

3.1 Meshing Tools and Meshing Quality Parameters

It's difficult to define a general way to create a perfect mesh; this depends on the physical situation under study. In case of laminar flow, there are strong temperatures and velocity gradients near the wall that means fast variations of the parameters involved. A mesh is no more than a grid that covers the whole geometry. In the nodes that are formed between cells, the fundamental equations, seen in chapter 3, subchapter 3.3.1, are applied and calculated. Then the results will be an average of those found in the nodes. The first thing to deal with is the geometry of the grid. Many different cells and grids types are available: choice depends on the physical problem and the solver power.

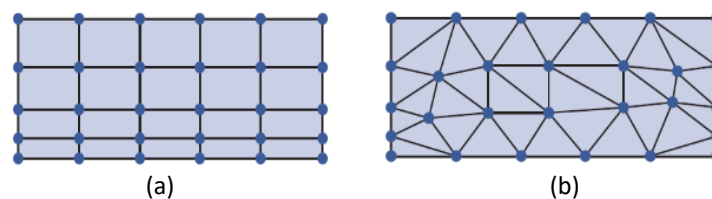


Fig. 26. (a) Structured mesh (b) Unstructured mesh [25]

ANSYS gives the possibilities to build two types of grid: a *structured grid*, much more clear and ordinate, and an *unstructured one*. Generally, having a structured grid composed by hexahedral cells is much suitable than having a tetrahedral one. This because the hexahedral mesh is more ordered than the others, and also because it needs less time to be configured by the software, that means less computing power. This kind of mesh gives in return more accurate solutions, especially if the grid lines are aligned with the flow. This doesn't exclude that for such cases a tetrahedral mesh won't be suitable (in fact it's the first mesh generates from the software because of its simplicity), but generally a well-structured grid is much optimized than an unstructured one [Fig. 26]. For a laminar flow the region adjacent to the wall is fundamental; the model should have a sufficiently fine mesh to adequately capture regions where the flow experiences rapid change in variables such as pressure, velocity or temperature for the resolution of the boundary layer. A typical velocity profile in the near-wall region has a variation in the velocity wall normal direction and it's important to

capture this gradient correctly. In this layer quad, hex cells are preferred over tri's and tets [Fig. 27].

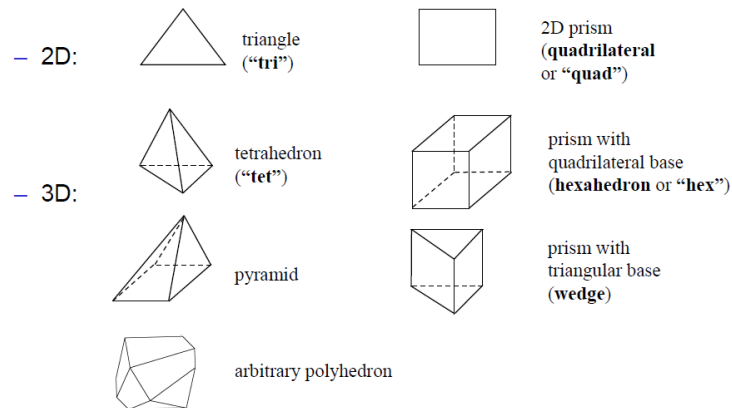


Fig. 27 Different types of cells implemented by ANSYS [25]

For this purpose, it's a good practise to use in this area the tool “inflation”. It allows to have more cells density near the wall that gradually decreases with the increasing of the length. It's appropriate to apply inflation on pipe sections but also on its length (following the flow direction) starting from the inlet, with much more subdivisions, for ending at the outlet with less of them [Fig. 28].

Another useful tool is “sweep”. The Sweep Method begins by meshing a particular 'source'/surface; this surface will then be swept through the body, spacing it by a certain incremental dimension or by splitting the swept side faces into a desired number of divisions.

Sometimes becomes necessary to use the tool “sizing” that allows to increase or decrease the number of subdivision on an edge or inside a volume or along a surface. This helps to control the number of cells that compose the model.

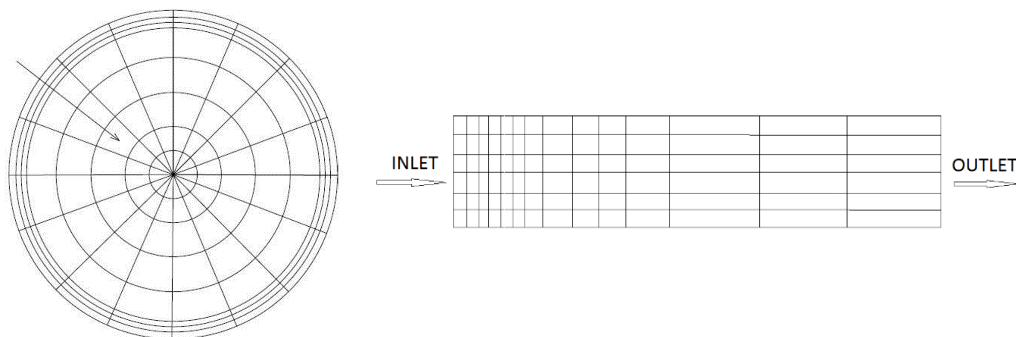


Fig. 28 Inflation layers with lateral surface as boundary geometry on the left and with the circular edge on the right [25]

To estimate the quality of the grid under construction there are some parameters that need to be monitored while meshing a geometry.

The first one is surely “*number of cells*”. Having a high number of cells means a high quality on the final results but makes the calculation heavier and longer. This permits to say that an optimized mesh is the one that gives good results with the less possible number of elements. For understanding what means higher or lower number of cells it is possible to follow the conceptual example below:

- 10^4 are relatively small problems;
- 10^5 are intermediate size problems;
- 10^6 are large problems. Such problems can be efficiently run using multiple CPUs, but mesh generation and post-processing may become slow;
- 10^7 are huge problems and should be avoided if possible.

An important parameter for understanding the real quality of the mesh, is the “*aspect ratio*”. It gives the measure of the stretching of a cell. It is computed as the ratio of the maximum value to the minimum value of any of the following distances: the normal distances between the cell centroid and face centroids, and the distances between the cell centroid and nodes. It is easily the ratio of longest edge to shortest edge length. The ideal condition is having aspect ratio equal to 1.

Higher values of this parameter means that there is almost one three-dimensional cell that develops in length with a very strange shape that reduces the mesh quality.

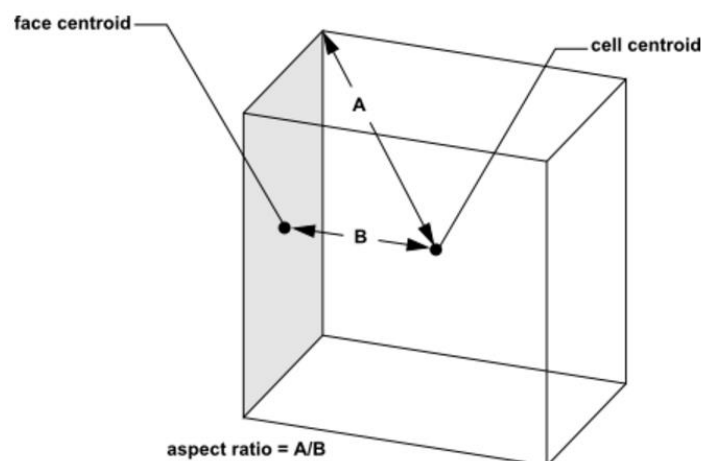


Fig. 29 Geometrical meaning of aspect ratio [24]

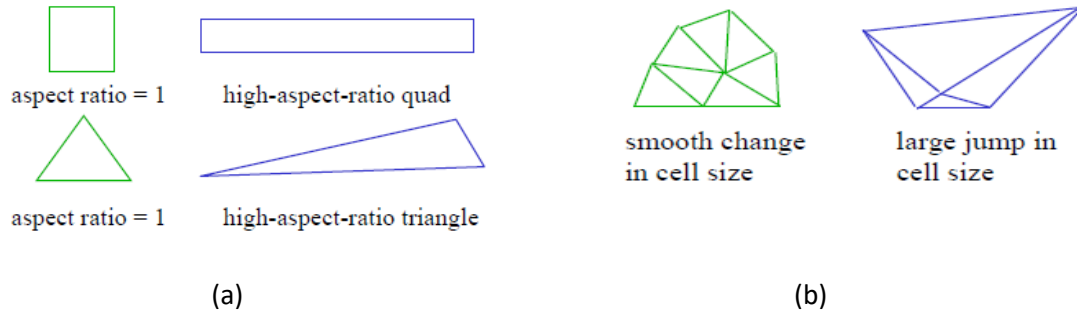
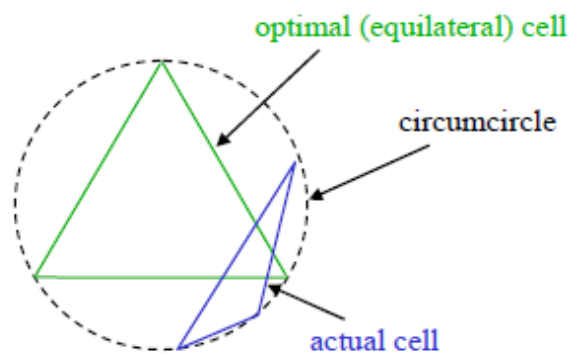


Fig 30 Geometrical meaning of (a) Aspect ratio (b) Smoothness [24]

Tied to the size of the cell, also the “smoothness” has to be considered. This is related to the change in size that takes place between two adjacent cells. It is preferred a change in size as graduate as possible. Ideally the maximum change in grid spacing should be <20%:

$$\frac{\Delta x_{i+1}}{\Delta x_i} \leq 1.2$$

“Skewness” is another parameter to take into account. High values of this parameter are not recommended because it means that the cell is too much warped and then the calculations in that place will be affected by errors. A scale for skewness validation is reported in figure 31. ANSYS give back a minimum and a maximum for this parameter: generally the max should stay below 0.85 and goes to 0.

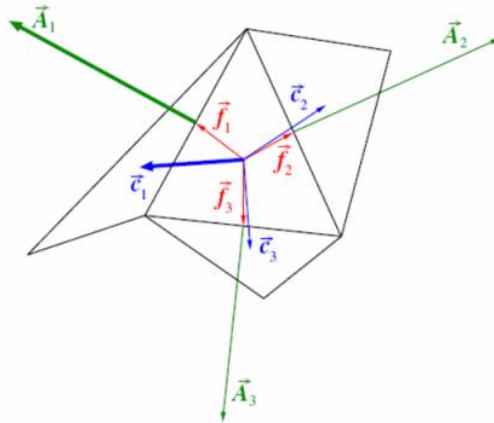


Skewness mesh metrics spectrum

Excellent	Very good	Good	Acceptable	Bad	Unacceptable
0-0.25	0.25-0.50	0.50-0.80	0.80-0.94	0.95-0.97	0.98-1.00

Fig. 31 Skewness geometrical representation and metrics for its evaluation [24]

Another important parameter is the “*orthogonal quality*”. The orthogonal quality for cells is computed using the face normal vector, the vector from the cell centroid to the centroid of each of the adjacent cells, and the vector from the cell centroid to each of the faces. Low orthogonal quality is not recommended. This value has a maximum and a minimum as the one before: the max has to go to 0 and the min to 1.



Orthogonal Quality mesh metrics spectrum					
Unacceptable	Bad	Acceptable	Good	Very good	Excellent
0-0.001	0.001-0.14	0.15-0.20	0.20-0.69	0.70-0.95	0.95-1.00

Fig. 32 Orthogonal quality geometrical representation and metrics for its evaluation [24]

3.2 Water Flow: Mesh Creation

After having well analysed the physical behaviour of the water flow, it is known that, starting from the pipe's inlet, there is a region where the flow is not already fully in laminar motion but still under development: in this region there isn't a well-defined boundary layer. Accounting also the external heat that arrives to the water from the electronics chips, for sure an important heat exchange takes place in this region with higher values of the heat transfer coefficients. For these reasons it is very important to build a mesh with a high accuracy on the water wall. For this reason, it is fundamental to deal with a structured mesh: much order helps the calculation on the water surface. For this reason, a mesh using prisms (rectangles) is preferred over a mesh using tetrahedrons (triangles). Not to forget that the mesh has to develop in the same direction of the water flow.

For trying to build an acceptable mesh that respects the previous requirements, different types of meshes were created and then compared. The comparisons will give the possibility to understand which one fits better the water behaviour and will give values closer to those that come from the analytic evaluations.

To test the property of each mesh, the water was simulated at first, with a straight cylinder of 2 mm of diameter and of 600 mm length. This length was chosen because it gives the possibility to try different meshing methods in an easy way due to the speed in which the calculations are performed. Secondary because the simulations will be compare with analytical equations use as benchmark. A good comparison can be made only if the benchmark is something really well known. Looking at the water behaviour, the scientific certitude is in the laminar fully developed region. Here literature gives lots of tested correlations unlike for the developing region where the behaviour isn't well defined. For all this reasons the meshes were tested on a length of 600 mm that is bigger than the length at which the fully developed laminar flow starts: 450 mm. in this way there is the possibility to dial with a fully developed laminar flow.

3.2.1 Mesh Characterisation

The first mesh created, called 77K [Fig. 33], is the one with the lowest number of cells and the one built by ANSYS without using any additional tool. This mesh has 77.162 cells and no inflation layers or sizing on it.

- Aspect ratio max 2
- $0.048 < \text{skewness} < 0.566$
- $0.67 < \text{orthogonal quality} < 0.99$

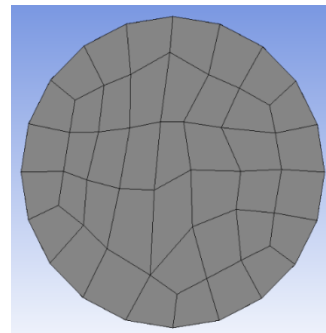


Fig. 33: MESH 77K/ 77.162 elements

Mesh 300K-INF has 308.380 elements [Fig. 34]. In this case was built by using a sweep method on the whole body starting from the inlet surface up to the outlet surface. After this the sweep method was inflate by using 5 layers of inflation with a growth rate of 1.2.

- Aspect ratio max 15
- $0.083 < \text{skewness} < 0.470$
- $0.74 < \text{orthogonal quality} < 0.99$

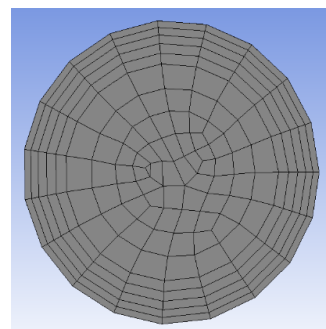


Fig. 34: MESH 300K-INF / 308.380 elements

Mesh 700K-INF has 704.340 elements [Fig. 35]. Is made in the same way of the previous one but in adjunction was introduced an edge sizing made of 30 subdivisions.

- Aspect ratio max 11
- $0.03 < \text{skewness} < 0.64$
- $0.64 < \text{orthogonal quality} < 0.99$

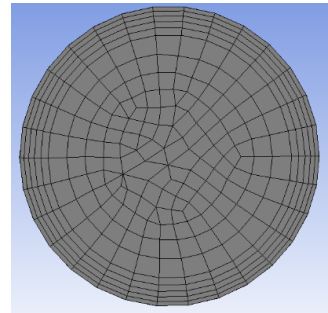


Fig. 35: MESH 700K-INF / 704.340 elements

Mesh 1500K-INF has 1.464.436 elements [Fig. 36]. Is similar to the previous one but with 7 layers of inflation with a growth rate of 1.1 and with an edge sizing made of 40 division.

- Aspect ratio max 15
- $0.032 < \text{skewness} < 0.41$
- $0.64 < \text{orthogonal quality} < 0.99$

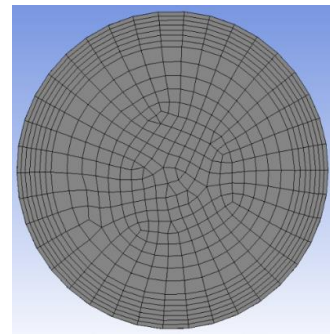


Fig. 36: MESH 1500K-INF / 1.464.436 elements

3.3 Fluent Analysis

Each mesh was then sent to Fluent for hydrodynamic evaluations. The following data were used:

\underline{r}	0.001	<i>m</i>	\underline{v}	0.32	<i>m/s</i>	$\underline{\mu}$	0.001	<i>Pa*s</i>
\underline{d}	0.002	<i>m</i>	\underline{m}	0.001004	<i>kg/s</i>	$\underline{\rho}$	998.210	<i>kg/m³</i>
\underline{L}	0.600	<i>m</i>	$\underline{\Delta T}$	4.7	<i>°K</i>	\underline{cp}	4182	<i>J/kgK</i>
$\underline{2p}$	6.28E-03	<i>m</i>	\underline{Q}	20.000	<i>w</i>	\underline{k}	0.6	<i>W/mK</i>
\underline{A}	3.14E-06	<i>m²</i>	$\underline{Q/Alat}$	5305.165	<i>W/m²</i>	\underline{Pr}	7.008	-
\underline{Alat}	3.77E-03	<i>m²</i>				\underline{Re}	637.834	-

An inlet velocity of 0.32 m/s and a constant wall heat flux of 5305.165 W/m² were imposed as boundary conditions. The wall temperature and the bulk temperature were obtained from Fluent and with these values Nusselt number and the convective coefficient were calculated. This was done for each surface situated at the different distances along the pipe, reported in figure 37.

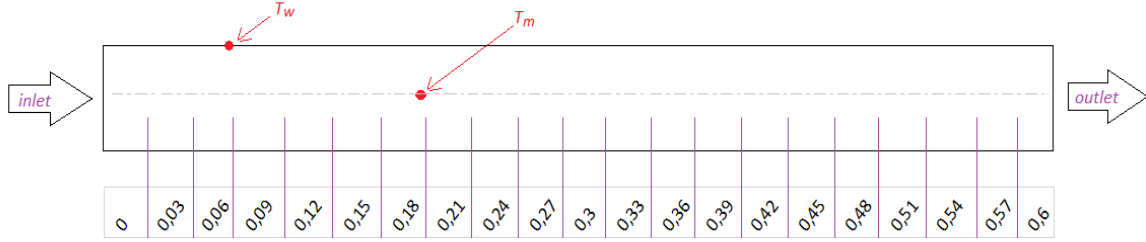


Fig. 37 Surfaces chosen along the pipe length

Knowing the temperature values the h coefficient and the Nu number were obtained by calculations.

$$h = \frac{Q}{T_w - T_m} \quad Nu = \frac{h d}{k} \quad (52)$$

On the other hand, the analytical values for the temperature and the thermal coefficients, were obtained with thermal balances applied between the inlet and each section in figure 37. Thermal balance from inlet up to each desired section was made as follow

$$Q = m cp (T_{out} - T_{in}) \quad (53)$$

$$T_{out} = \frac{Q}{m cp} + T_{in}$$

Where T_{out} will become T_m at the end of each section. The thermal balance that gave T_{sup} on each circular surfaces along the pipe is:

$$Q = h (T_{sup} - T_m) \quad (54)$$

$$T_{sup} = \frac{Q}{h} + T_m$$

In order to obtain Nu number, the following equation was used:

$$Nu = 4.363 + 8.68 (10^3 x^*)^{-0.506} e^{-41x^*} \quad (55)$$

$$x^* = \frac{x}{Re d}$$

while h was obtained from:

$$q'' = h (T_s - T_b) \quad (56)$$

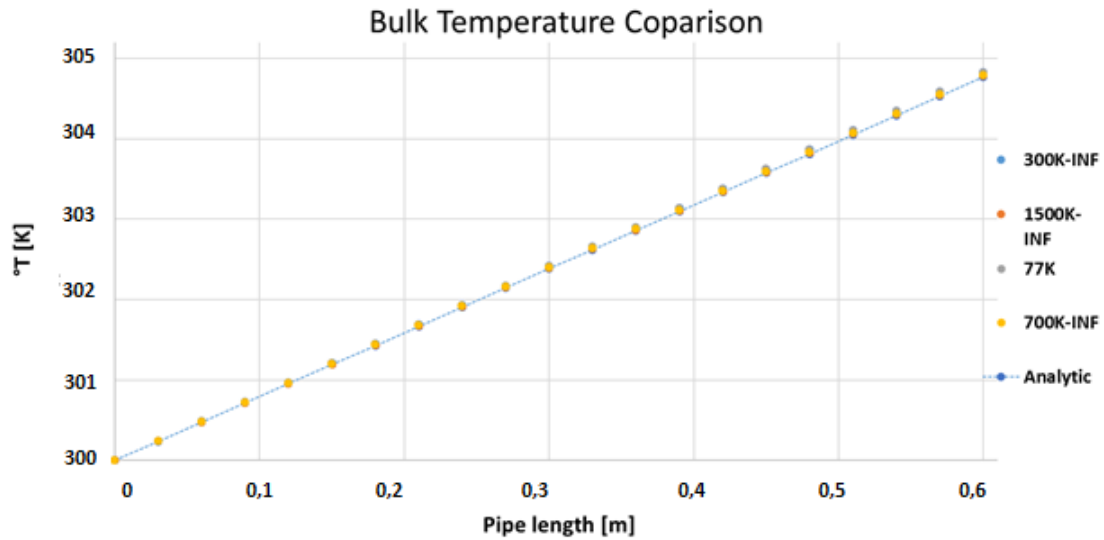


Chart. 3 Water bulk temperature: comparison between the analytic and numerical results. Results reported for each mesh created

Making the comparison between Fluent results and the analytic ones, the results obtained are reported here in table 5.

	Equation	77K	300K- INF	700k- INF	1500k- INF
m	T_m	T_m	T_m	T_m	T_m
0	300,00	300,00	300,00	300,00	300,00
0,03	300,24	300,24	300,24	300,24	300,24
0,06	300,48	300,48	300,48	300,48	300,48
0,09	300,71	300,72	300,73	300,72	300,72
0,12	300,95	300,97	300,97	300,96	300,96
0,15	301,19	301,21	301,21	301,20	301,20
0,18	301,43	301,45	301,45	301,44	301,43
0,21	301,67	301,69	301,69	301,68	301,67
0,24	301,91	301,93	301,93	301,92	301,91
0,27	302,14	302,17	302,17	302,16	302,15
0,3	302,38	302,41	302,42	302,40	302,39
0,33	302,62	302,66	302,66	302,64	302,63
0,36	302,86	302,90	302,90	302,88	302,87
0,39	303,10	303,14	303,14	303,11	303,11
0,42	303,34	303,38	303,38	303,35	303,35
0,45	303,57	303,62	303,62	303,59	303,59
0,48	303,81	303,86	303,86	303,83	303,83
0,51	304,05	304,10	304,11	304,07	304,06
0,54	304,29	304,34	304,35	304,31	304,31
0,57	304,53	304,59	304,59	304,55	304,54
0,6	304,77	304,83	304,83	304,79	304,78

Tab. 5 Bulk temperature [$^{\circ}$ K]: comparison between the analytic and numerical results. Results reported for each mesh created

The same comparison was made for the wall temperature. Results are in table 6.

	Equation	77K	300K- INF	700k-INF	1500k-INF
m	T_w	T_w	T_w	T_w	T_w
0	300,05	300,73	300,12	300,09	300,07
0,03	303,75	302,09	302,27	302,29	302,27
0,06	304,37	302,78	303,05	303,05	303,04
0,09	304,72	303,36	303,61	303,60	303,59
0,12	304,99	303,85	304,07	304,05	304,05
0,15	305,24	304,27	304,48	304,46	304,46
0,18	305,48	304,66	304,85	304,83	304,83
0,21	305,72	305,01	305,19	305,17	305,18
0,24	305,96	305,34	305,52	305,50	305,51
0,27	306,20	305,65	305,83	305,81	305,82
0,3	306,44	305,95	306,13	306,11	306,12
0,33	306,67	306,25	306,42	306,40	306,41
0,36	306,91	306,53	306,70	306,68	306,69
0,39	307,15	306,81	306,97	306,95	306,96
0,42	307,39	307,09	307,24	307,22	307,23
0,45	307,63	307,35	307,51	307,49	307,50
0,48	307,87	307,62	307,77	307,75	307,76
0,51	308,10	307,88	308,03	308,00	308,01
0,54	308,34	308,14	308,28	308,26	308,27
0,57	308,58	308,40	308,54	308,51	308,52
0,6	308,82	308,16	308,70	308,70	308,72

Tab. 6 Water wall temperature: comparison between the analytic and numerical results. Results reported for each mesh created

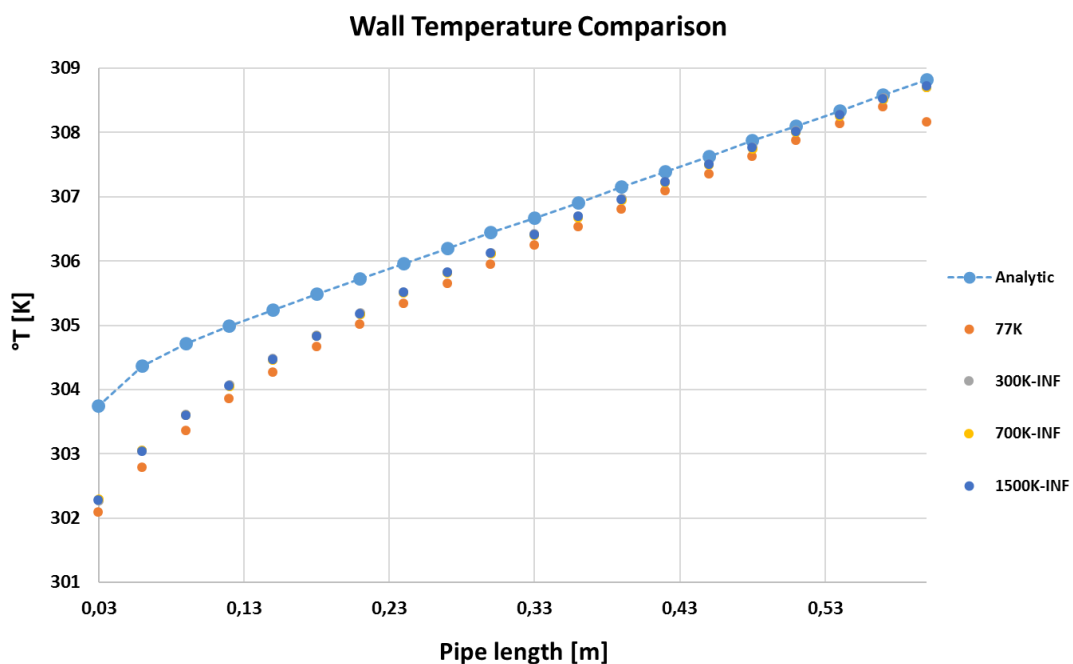


Chart. 4 Water wall temperature: comparison between the analytic and numerical results. Results reported for each mesh created

Tables and charts show that several meshes give good results. In particular, giving a look at the chart 3, is possible to notice that the analytical and numerical results are really close together. For this reason, can be deduced that mesh built in this way are appropriate. To understand which is the best way to mesh, chart 4 with the wall temperature comparison is analysed: the difference between the values analytically deducted and those from the simulations is obvious. At a first glance is clear the difference of 77K results in comparison to the other meshes but mainly in comparison with the analytic results. This gives the possibility to discard this mesh and to focus on the others. The other meshes with more elements, gave nearly the same results closer to those from the correlations in the fully developed region after 0.45 m. Before this point the trends of the meshes diverge. This is due to the developing of the laminar motion that is detected only by the simulations but not from the analytic estimations (in fact the used equation was wrote for developed laminar flow only).

3.3.1 Heat Transfer Coefficients

To evaluate the thermal behaviour of the water flow, Nu number and the convective coefficient, h , were calculated for each meshes, using the parameters previously obtained, and also were calculated trying different correlations: the aim is to find the one that fits better the numerical results.

For the meshes, knowing the wall and the bulk temperature of the water flow, the h coefficient was calculated as $h = \frac{q''}{T_w - T_m}$.

Afterwards Nu number was obtained using $Nu = \frac{h d}{k}$, where k is the water conductivity coefficient.

The analytic equations used for the comparison are those presented here:

- **Shah – London Equation** for developing flow

$$Nu = 4.363 + 8.68 (10^3 x^*)^{-0.506} e^{-41x^*} \quad (57)$$

$$x^* = \frac{x}{Re d}$$

- **Kays Equation** for developing flow

$$Nu = 3.66 + \frac{0.0668 G_z}{1 + 0.04 G_z^{2/3}} \quad (58)$$

$$G = \frac{d Pr Re}{x}$$

- **Baher - Stephan Equation** for developing flow

$$Nu = \frac{\frac{3.66}{\tanh(2.264 G_z^{-\frac{1}{3}} + 1.7 G_z^{-\frac{2}{3}})} + 0.0499 G_z \tanh(G_z^{-1})}{\tanh(2.432 Pr^{\frac{1}{6}} G_z^{-\frac{1}{6}})} \quad (59)$$

- **Costant Surface Heat Flux Equation (Cost. SHF)** for fully developed region

$$Nu = \left\{ 4.364^3 + 1 + \left[1.953 \sqrt[3]{Re Pr \frac{d}{l}} \right]^3 \right\}^{\frac{1}{3}} \quad (60)$$

The results of Nu number along the pipe for each mesh and for each equation are those in table 7. Is necessary to remember that a constant heat flux was imposed all over the lateral surface of the water flow.

	Cost. SHF	Sha - London	Kays	Baher- Stephan	77K	300K-INF	700K- INF	1500K- INF
<i>m</i>	Nu	Nu	Nu	Nu	Nu	Nu	Nu	Nu
0,03	13,19	5,03	10,79	11,83	9,56	8,71	8,63	8,71
0,06	10,60	4,54	8,33	9,06	7,69	6,88	6,88	6,91
0,09	9,36	4,42	7,22	7,82	6,70	6,14	6,14	6,16
0,12	8,60	4,38	6,57	7,08	6,14	5,70	5,72	5,72
0,15	8,07	4,37	6,13	6,58	5,78	5,41	5,42	5,42
0,18	7,68	4,37	5,81	6,21	5,51	5,20	5,22	5,20
0,21	7,37	4,36	5,57	5,93	5,33	5,05	5,07	5,04
0,24	7,12	4,36	5,38	5,70	5,19	4,93	4,94	4,91
0,27	6,91	4,36	5,22	5,52	5,08	4,83	4,84	4,82
0,30	6,73	4,36	5,09	5,36	5,00	4,77	4,77	4,74
0,33	6,58	4,36	4,99	5,23	4,93	4,70	4,70	4,68
0,36	6,45	4,36	4,89	5,11	4,87	4,65	4,65	4,63
0,39	6,33	4,36	4,81	5,01	4,82	4,62	4,61	4,59
0,42	6,23	4,36	4,74	4,93	4,77	4,58	4,57	4,56
0,45	6,14	4,36	4,68	4,85	4,74	4,55	4,53	4,52
0,48	6,06	4,36	4,63	4,78	4,70	4,52	4,51	4,50
0,51	5,98	4,36	4,58	4,71	4,68	4,51	4,50	4,48
0,54	5,92	4,36	4,53	4,66	4,65	4,50	4,48	4,47
0,57	5,85	4,36	4,49	4,61	4,64	4,48	4,47	4,44
0,60	5,80	4,36	4,46	4,56	5,31	4,57	4,52	4,49

Tab. 7 Nusselt number: comparison between the analytic and numerical results.
Results reported for each mesh created

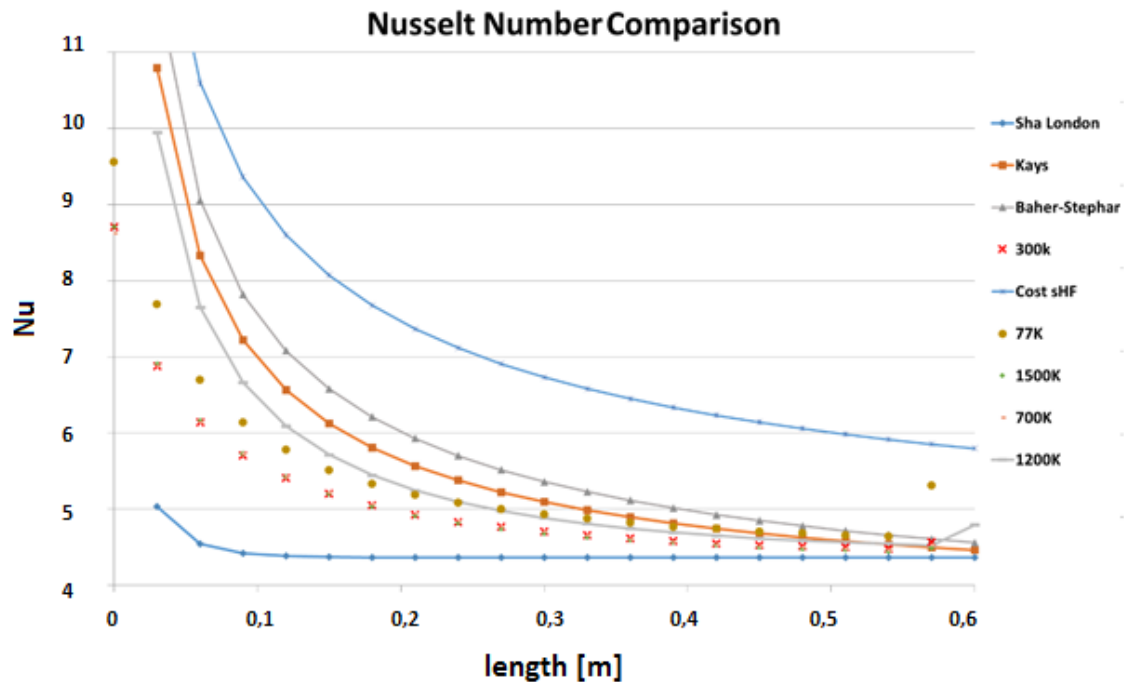


Chart. 5 Nusselt number: comparison between the analytic and numerical results. Results reported for each mesh created

This comparison shows that at the beginning of the developed region, the trend of each correlation tends to be 4.36 that is the Nu values for the fully laminar flow. The results of the simulations are really accurate after the developing region. In fact, they have the same trend the correlations have. The two meshes that give the most accurate results are those with 300k and 1500k elements.

3.4 Velocity profiles

For a deeper validation of the meshes, a comparison of the water velocity profile was made. The equation that gives the velocity profile of the flow in a section along the pipe, normal to the flow direction, is the one that follows:

$$v = \frac{\Delta p}{4 l \mu} (R^2 - r^2) \quad (61)$$

where R is the radius of the water channel, 1 mm, and r is the position along the diameter of a circular section of the channel. Δp indicates the pressure drops that occurs between the inlet surface and each surface along the pipe as shown in figure 35. The numerical results were conversely obtained from ANSYS Fluent. The comparison is reported in chart 5. It shows that each mesh fits very well the analytic profile.

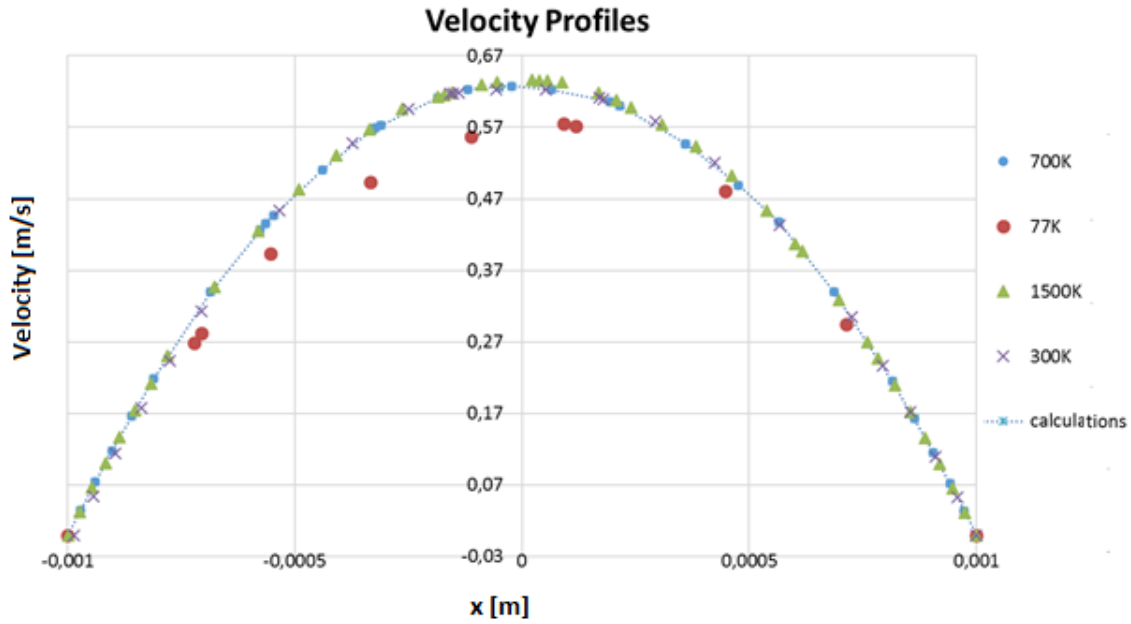


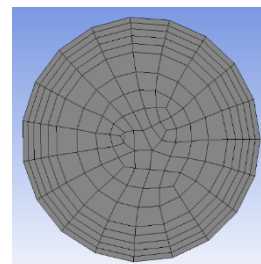
Chart. 6 Velocity profile: comparison between the analytic and numerical results. Results reported for each mesh created

Only mesh 77K has a different trend. This gives the certitude that this mesh isn't reliable at all. The others give good realistic results and can still be considered.

3.5 Mesh Selection

With these different comparisons made on the results from each mesh, it is now possible to select the best mesh to use on the future water simulations of the flow inside the plate. After the evaluations and the comparisons of the quality parameters, it's also necessary to make a forecast on the number of cells involved once increasing the pipe length. As said this is one of the most important parameter for the final choice. As in table 8, the last two meshes will give an excessive number of cells for a length of 1.3 m (that is the one estimated in the first dimensioning). 77K was already not considered because of its worst results on simulations. Therefore, only meshes 300K and 700K remain available. These two meshes give similar good results. For this reason, with the aim to create the lightest mesh possible, the mesh 300K seems to be the best solution for this type of problem.

	600 mm		1327,7 mm
77K	77162	→	170746
300K-INF	308380	→	682393
700K-INF	704340	→	1558587
1500K-INF	1464436	→	3240553



Tab. 8 Cells growing while increasing pipe's length: mesh choice on the right

4 Numerical Simulation of the System

4.1 Water Flow and Pipe Meshing

Once the mesh 300K-INF was selected for the fluid meshing, this was applied to the water domain inside the plate. For having the same good results, already tested, a sweep method (that has as source the inlet water surface) was applied to the flow and to the pipe's length with a growth rate of 50; this method was then inflated with 5 layers and a growth rate of 1.2. The result is the one in figure 38.

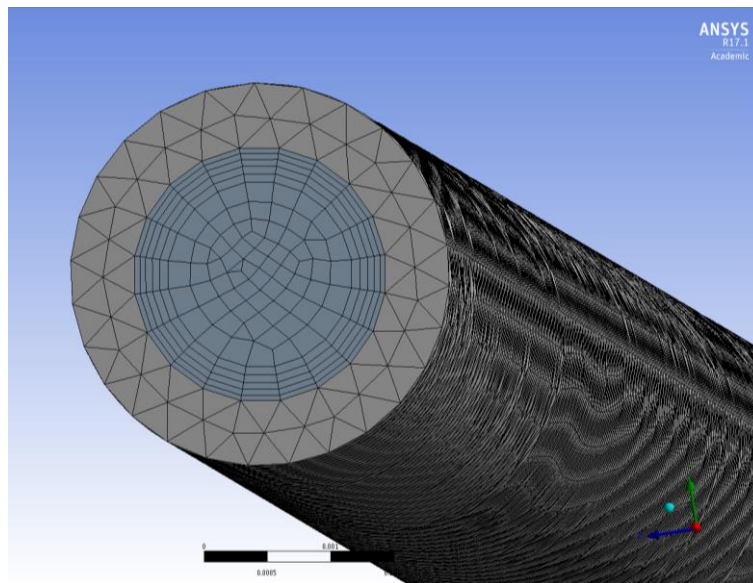


Fig. 38 Mesh of the water flow and the steel pipe inside the plate

4.2 Plate Meshing

For the plate a structured mesh was implemented by changing the parameter of the initial sizing defaulted by ANSYS. MultiZone method was applied to the plate starting from the surface which contains the chips. A tetrahedral mesh was obtained, is surely well structured but is not made of hexahedrons because the software perceives the plate too thin in some areas and here is able to create good meshes only by using tetrahedrons. The result is reported in figure 39.

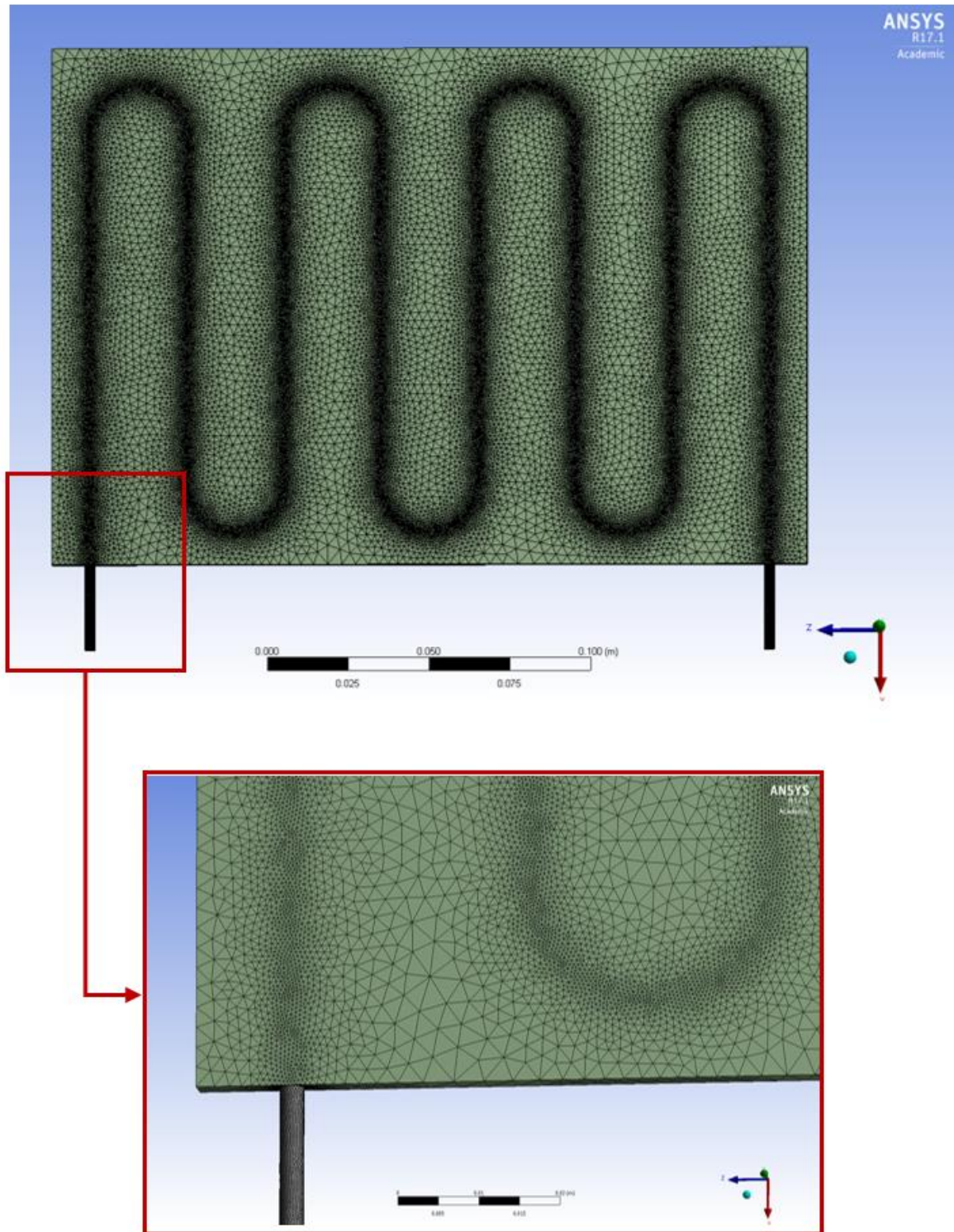


Fig. 39 Mesh of the whole plate

4.3 Simulation Results: Fluent Analysis

The simulations with ANSYS Fluent, were performed for three different water flows, 5,11,15 l/h, at the nominal chips' power. The simulations were also experienced at an inlet water flow of 20°C and of 15°C. The data required to start the simulation are here reported in table 9.

	5 l/h	11 l/h	15 l/h
m [kg/s]	0,001	0,003	0,004
v [m/s]	0,44	0,97	1,32
ΔT [°K]	4,46	2,03	1,48
Re	880	1936	2640
Lth [m]	0,61	1,35	1,84
Lid [m]	0,08	0,19	0,26

Tab. 9 Water behaviour at different flows

On one side of the plate 10 areas were drawn to simulate the main chips. To each area a power in W/m² was given, as table 10 shows.

	Dimensions	Area [m ²]	Nominal Power [W]	W/m ²
FPGA	2x2 cm	0,0004	7,5	18750
VTTX	2x1 cm	0,0002	0,75	3750
GBTX	1x1 cm	0,0001	1,2	12000
SCA	1x1 cm	0,0001	0,1	1000
OTHER	3x2,5 cm	0,00075	5	6667

Tab. 10 Chips dimension and power in W and W/m²

As boundary conditions were given the inlet temperature and the water velocity at the pipe's inlet. At the outlet the pressure was imposed as 0 Pa.

Is already known that the simulation won't give very realistic value because it considers an adiabatic work space that means no heat exchanges with the air around the plate, and also won't consider the chips thermal resistances and the resistance that will appear while gluing the board to the plate. The simulations, therefore, will give an ideal condition difficult to reach during a test section.

The results are here reported for the nominal chips conditions in table 11 and 12; in figure 40 is reported a graphic view of the simulation results for the 11 l/h flow.

5 l/h						11 l/h						15 l/h					
		T MAX	T MIN	MEDIA				T MAX	T MIN	MEDIA				T MAX	T MIN	MEDIA	
gbtx1		25,83	25,33	25,58		gbtx1		23,25	22,74	22,99		gbtx1		22,66	22,16	22,41	
gbtx2		26,18	25,74	25,96		gbtx2		23,60	23,16	23,38		gbtx2		22,99	22,55	22,77	
gbtx3		26,14	25,72	25,93		gbtx3		23,61	23,19	23,40		gbtx3		23,01	22,59	22,80	
vtx1		25,02	24,72	24,87		vtx1		22,62	22,35	22,49		vtx1		22,06	21,80	21,93	
vtx2		25,21	25,08	25,15		vtx2		22,85	22,71	22,78		vtx2		22,28	22,13	22,20	
vtx3		24,88	24,61	24,74		vtx3		22,59	22,36	22,48		vtx3		22,02	21,81	21,91	
fpga1		27,08	25,38	26,23		fpga1		25,07	23,47	24,27		fpga1		23,00	23,00	23,00	
fpga2		27,06	25,52	26,29		fpga2		25,07	23,68	24,38		fpga2		24,57	23,17	23,87	
other		23,51	22,28	22,89		other		22,28	21,32	21,80		other		22,00	21,12	21,56	
sca		22,06	21,67	21,87		sca		21,02	20,79	20,90		sca		20,79	20,61	20,70	
plate		26,90	20,78	23,84		plate		25,05	19,95	22,50		plate		24,38	20,20	22,29	

Tab. 11 Simulations results in °C: chips and plate temperatures with inlet water at 20°C

5 l/h	LOW T			11 l/h	LOW T			15 l/h	LOW T		
	T MAX	T MIN	MEDIA		T MAX	T MIN	MEDIA		T MAX	T MIN	MEDIA
gbtx1	20,82	20,32	20,57	gbtx1	18,24	17,74	17,99	gbtx1	17,63	17,13	17,38
gbtx2	21,16	20,73	20,95	gbtx2	18,16	18,23	18,19	gbtx2	17,98	17,54	17,76
gbtx3	21,13	20,70	20,92	gbtx3	18,61	18,19	18,40	gbtx3	18,00	17,59	17,79
vtx1	20,01	19,71	19,86	vtx1	17,62	17,35	17,49	vtx1	17,05	16,79	16,92
vtx2	20,20	20,07	20,14	vtx2	17,85	17,71	17,78	vtx2	17,27	17,12	17,20
vtx3	19,87	19,59	19,73	vtx3	17,56	17,36	17,46	vtx3	17,01	16,81	16,91
fpga1	22,07	20,37	21,22	fpga1	20,07	18,47	19,27	fpga1	19,56	18,00	18,78
fpga2	22,05	20,51	21,28	fpga2	20,07	18,68	19,38	fpga2	19,57	18,17	18,87
other	18,50	17,27	17,89	other	17,28	16,32	16,80	other	17,00	16,12	16,56
sca	17,05	16,66	16,86	sca	16,02	15,79	15,90	sca	15,79	15,61	15,70
plate	21,95	15,75	18,85	plate	20,07	15,00	17,54	plate	18,49	15,00	16,74

Tab. 12 Simulation results in °C: chips and plate temperatures with inlet water at 15°C

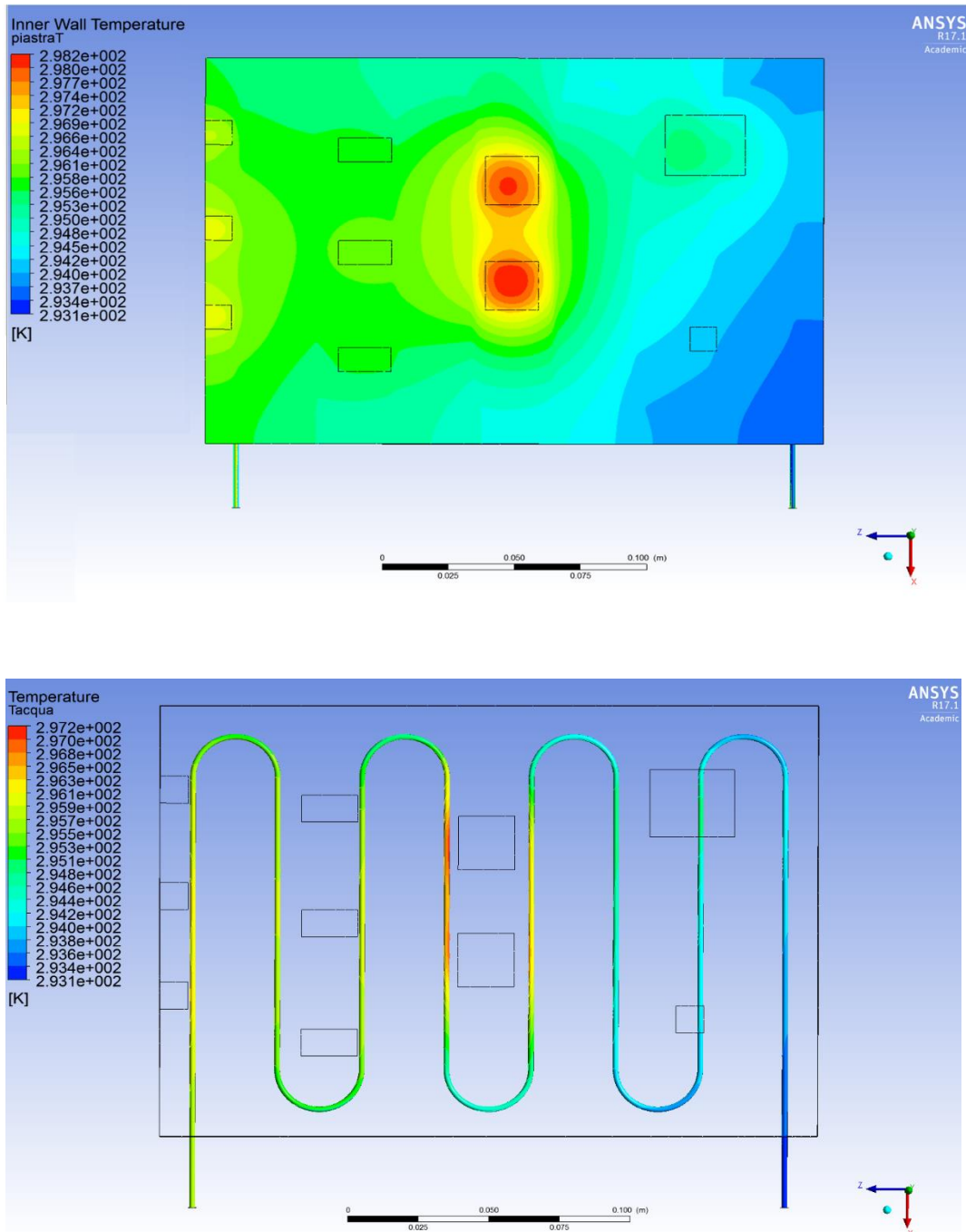


Fig. 40 Simulation result for 11 l/h flow: plate temperature in the picture above; water and chips on the one below

Looking at the pressure drops the results obtained from the simulation are reported in table 13 and will be later compared with the values obtained from the tests.

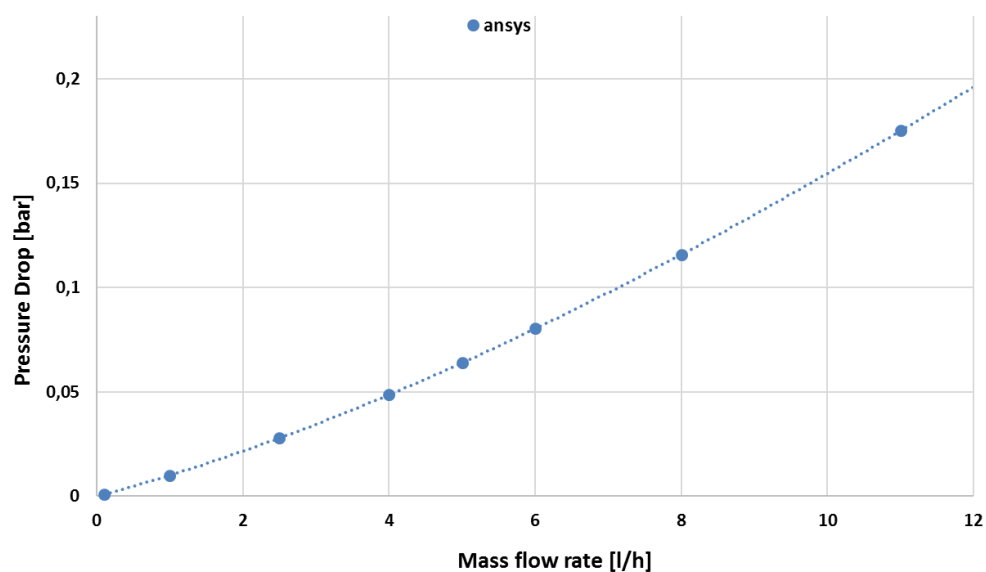
Δp		
m	Pa	bar
5 l/h	64250	0,64
11 l/h	17515	0,17
15 l/h	26170	0,26

Tab. 13 Pressure drop inside the plate at different water flows

On the water flow more simulations were performed at several values of l/h, for being able to obtain the trend of the pressure drop. This trend will be than compared to the one obtained from the tests.

Δp		
m [l/h]	Pa	bar
0,1	93,836	0,001
1	1001,5	0,01
2,5	2785,5	0,02
4	4869,9	0,05
5	6399	0,06
6	8039,2	0,08
8	11575	0,12
11	17515	0,17
15	26170	0,26

Water Serpentine - Pressure Drop



Tab. 14 and Chart. 7 Pressure drop: trend while varying the water flow

5 Experimental Investigation

5.1 Prototype Manufacturing

A main part of this work is based on testing the cooling plate prototype. The 3D model made with the use of SolidWorks and NX was sent to a technician for the manufacture. At first the stainless steel pipe was bent. An aluminium plate, used as support, was created for joining a jig [Fig. 41(c)] that is a tool, like a pulley, that allows to bend the pipe at a fixed bending radius. The bend radius used was of 15 mm.

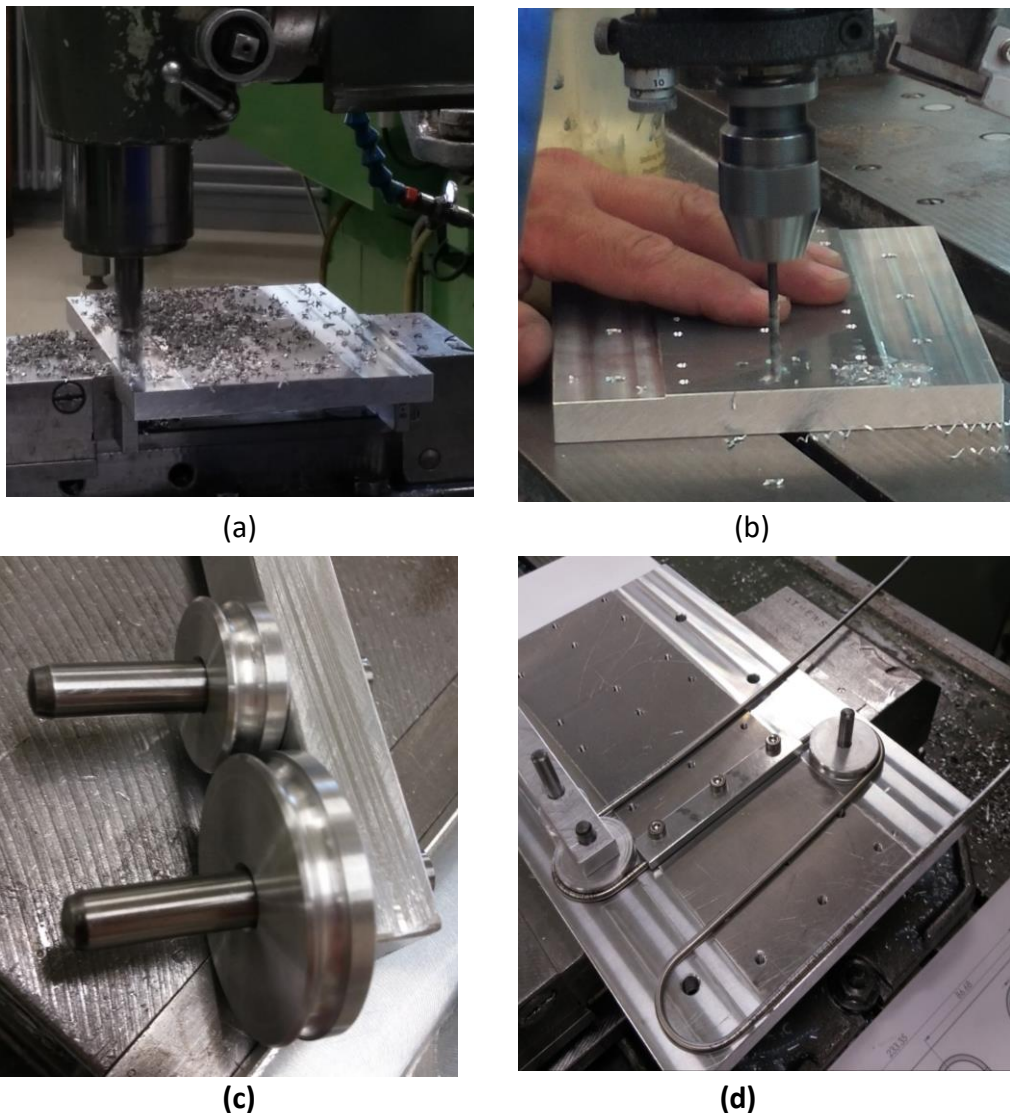


Fig. 41 (a), (b) support plate; (c) Jig; (d) pipe bending

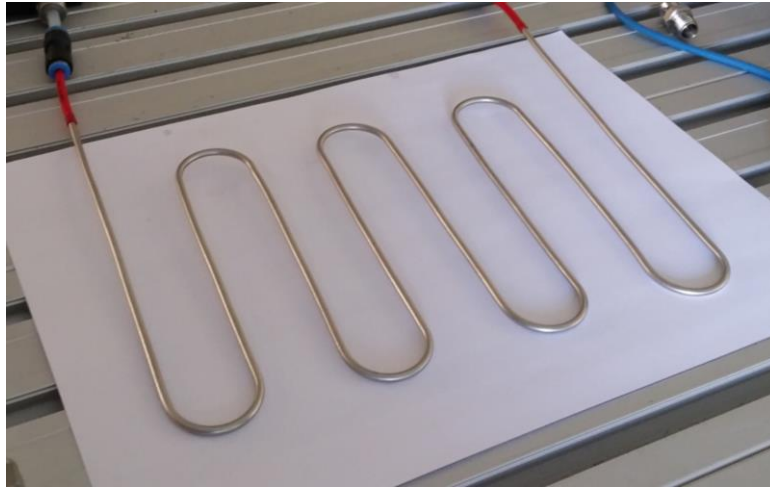


Fig. 42 *Finished prototype pipe*

After being bent, the entire pipe was curved and ready to be tested.

The plates manufacturing was based on the following step. At first the pipe's circuit was machined into a 2 mm aluminium plate. This was done for two plates. At the end the plates and the pipe were coupled together with a conductive glue and screwed together.

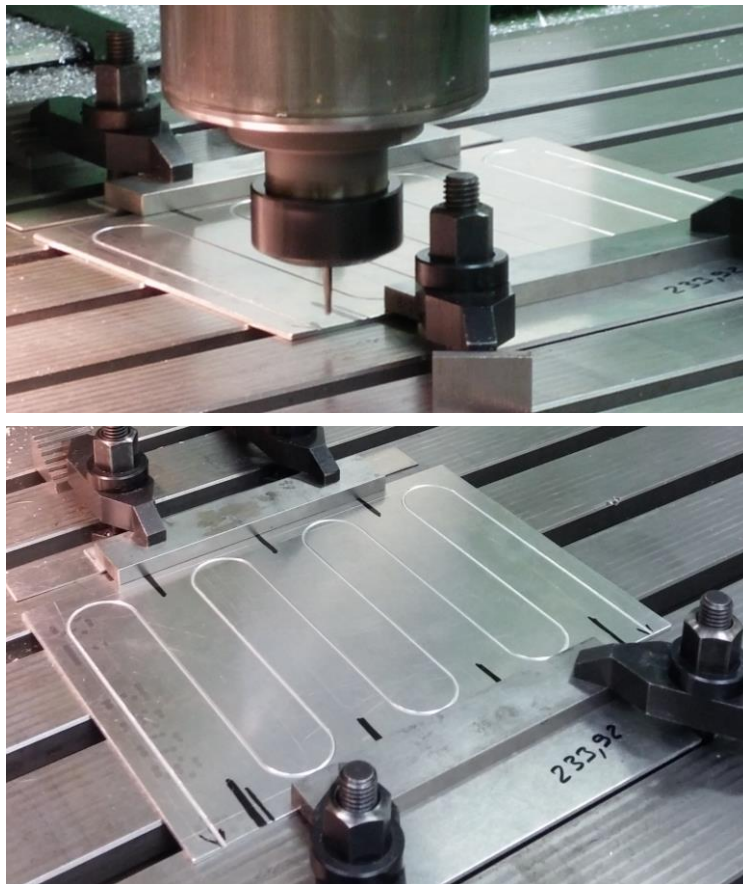


Fig. 43 *Plate machining*

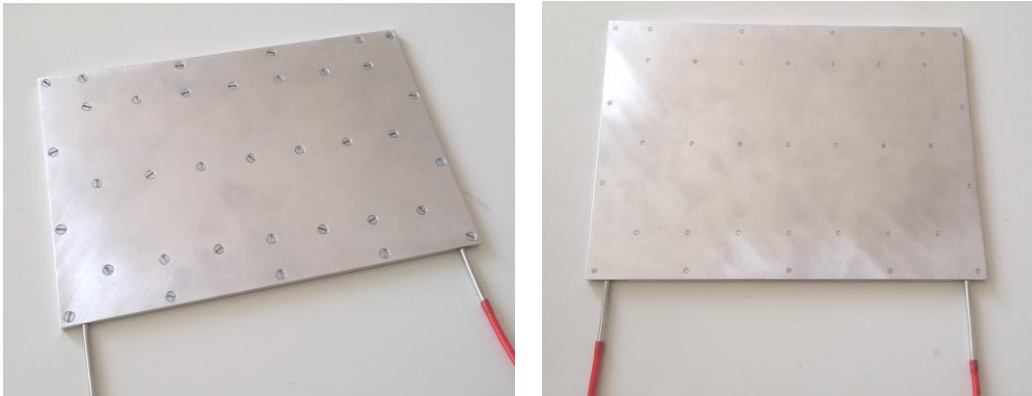


Fig. 44 *Finished prototype*

5.2 Test Section

The testing system is made of two main components: the first is the test set-up, the place in which the prototype is connected to the water plant, and the other zone, the test section, where there is the plant that permits the circulation of the water in sub atmospheric pressure.

The test set-up is basically a water circuit made of plastic pipes connected to an inlet and outlet pipe (both connected to the test section) made of steel. As figure 45 shows, after the inlet section the water flow pass through two valves: a safety valve that come into operation when the pressure in the plant is greater than 4.5 bar; a needle valve (V2) used for flow regulation. After valve V2 the flow has to pass through a flow meter (a turbine flow meter), which is connected to the read out card. Proceeding along the path the water flow meets a temperature (pt100) and a pressure meter before entering the prototype. At its outlet the flow impacts at first with another pt100 and pressure meter. Each of this sensors are connected to the read out unit. The flow that exits the testing tube goes to the return line. Before exits he meets a three-way valve used, with the needle valve V1, as a by-pass system: moving V1 the water flow can be deviated and then regulated. After the three-way valve, before the exit, is installed a ball valve that acts as a shutter.

For the tests several regulations on the water flow are requested. For doing this is useful to move the valve V1 at first, and when the valve stroke is at its end, also V2.

When V1 is closed no water flow pass through the by-pass. When V1 is open the water goes into the circuit side with the less hydraulic resistance that means it goes on the by-pass side. Then there is less water that goes to the testing prototype. If a major regulation is requested, valve V2 is movable till the closed position.

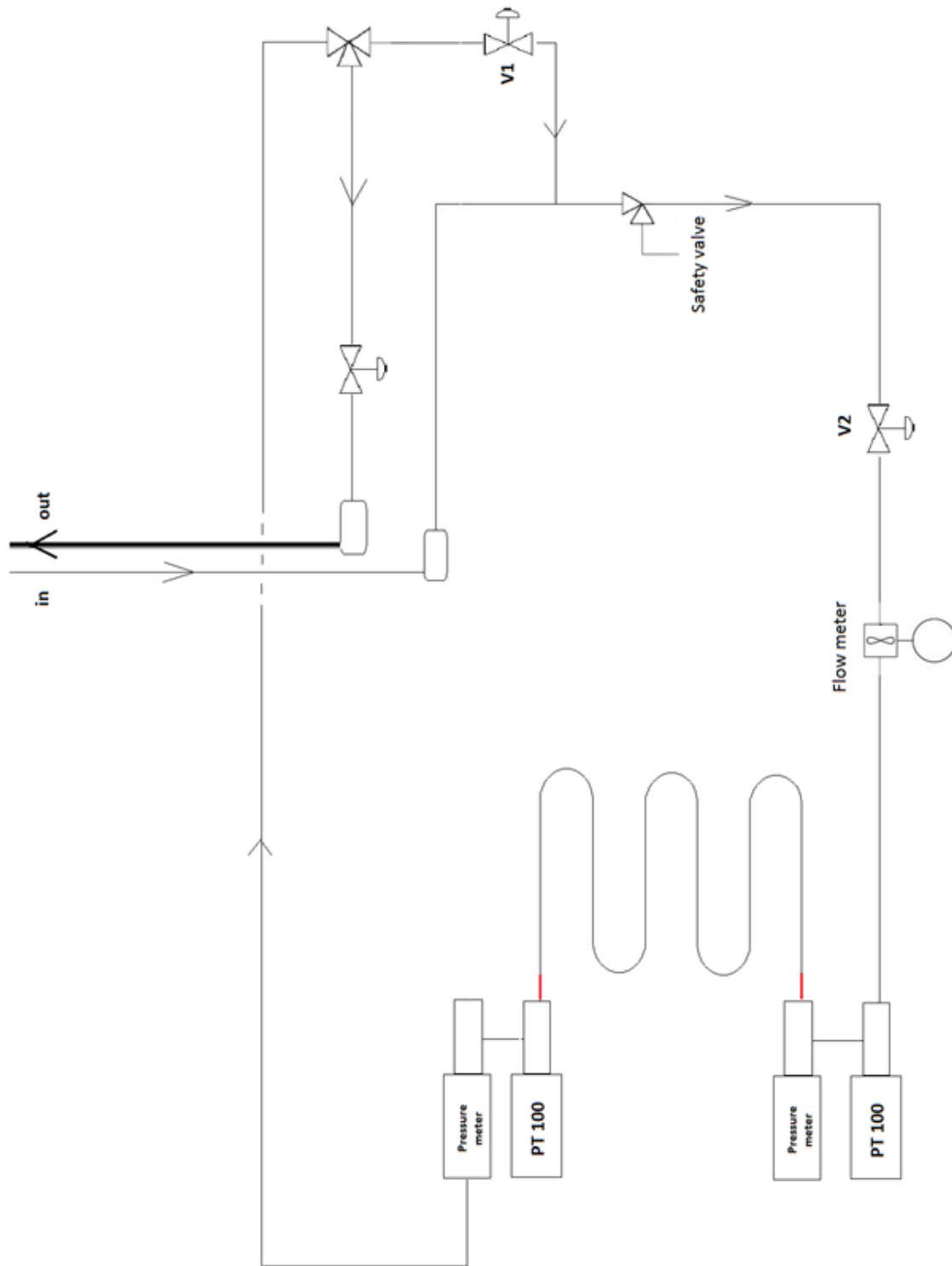


Fig. 45 Test section

The test plant, on the other hand, is basically a water plant made of different components. Its aim is to make the water circulate into the circuit at a sub atmospheric pressure to avoid the presence of the air inside the water flow. For this reason, a vacuum pump is installed. With this system is also possible to make a regulation on the water temperature by using a traditional refrigeration plant.

This system has been developed at CERN and is composed of:

- A water tank;
- A vacuum pump, that works based on a timed solenoid for maintaining the tank below the atmospheric pressure;
- A circulation pump, that injects the water into the circuit;
- A pressure switch, that stops the vacuum pump when the pressure of the water tank reaches a fixed value;
- Two filters, one on the main line and the other on a by-pass made only for the recirculation of part of the water into the filter.



Fig. 46 Views of the test plant

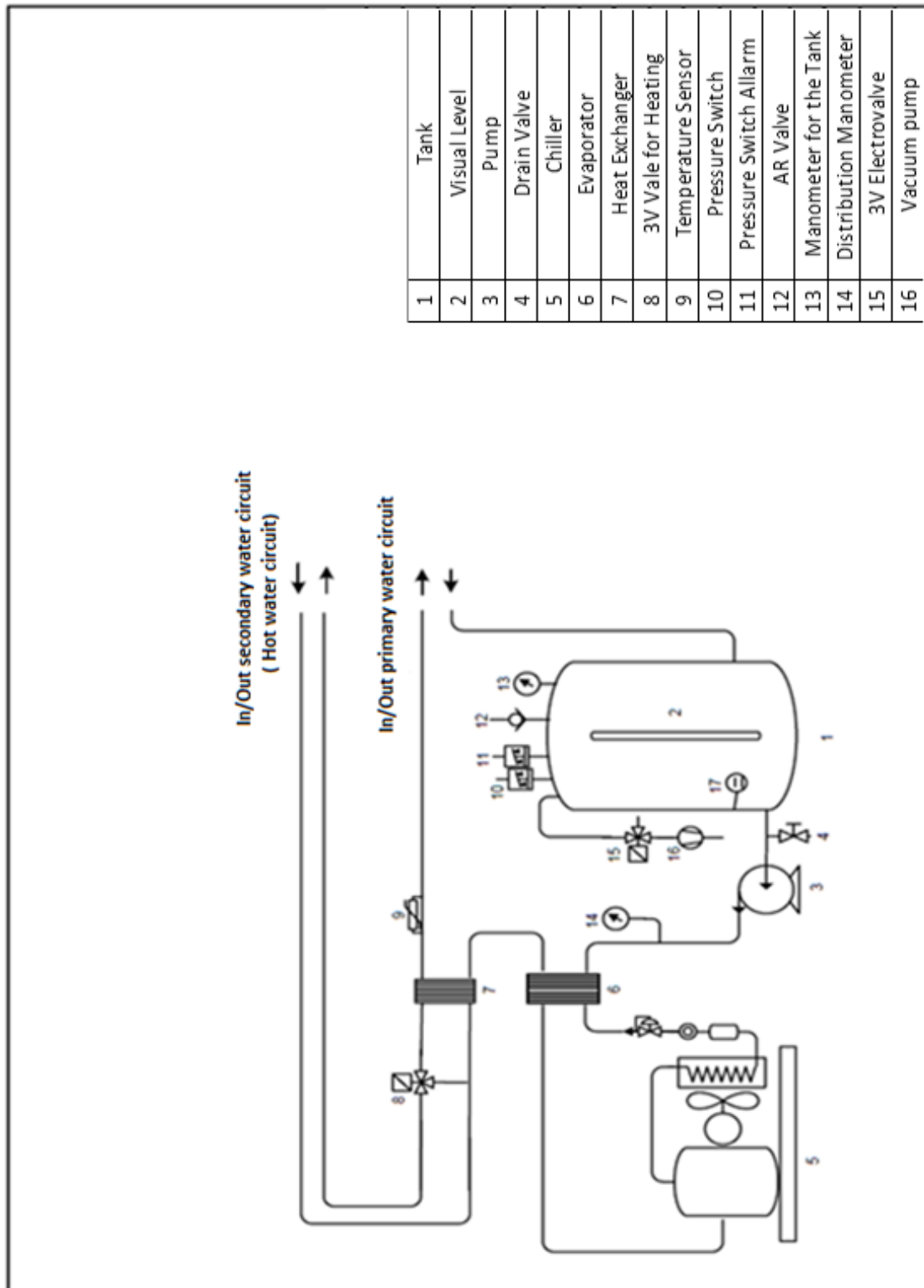


Fig. 47 Scheme of the testing section

5.3 Tests on the pipe

The tests done on the pipe are the following:

- Test on the connection pipes: flow variation for determining the pressure drop between inlet and outlet;
- Test on the serpentine pipe: flow variation for determining the pressure drop between inlet and outlet;

5.3.1 Test on the Connection Pipes

For having the real pressure drop into the serpentine is useful to find which is the pressure drop on the connection pipes used to join the pipe and the test circuit. For doing this a little portion of a plastic pipe, of about 11 cm, was taken and connected to the test set-up. The flow was varied between 16 and 6 l/h. The pressure drop measured in this test will be than subtracted to the total pressure drop for having more accurate values that allow to make a better comparison between analytic and numerical results.

Flow [l/min]	Pin [bar]	Pout [bar]	Δp	Flow [l/h]
0,27	0,57	0,55	0,017	16,07
0,25	0,56	0,55	0,012	14,80
0,23	0,59	0,57	0,013	13,77
0,20	0,62	0,60	0,011	12,21
0,18	0,58	0,57	0,009	11,18
0,16	0,62	0,62	0,008	9,53
0,14	0,63	0,63	0,006	8,46
0,13	0,64	0,63	0,005	7,74
0,12	0,59	0,58	0,004	7,32
0,11	0,61	0,60	0,005	6,68
0,10	0,57	0,57	0,003	6,01

Tab. 15 Results of the test on the connections

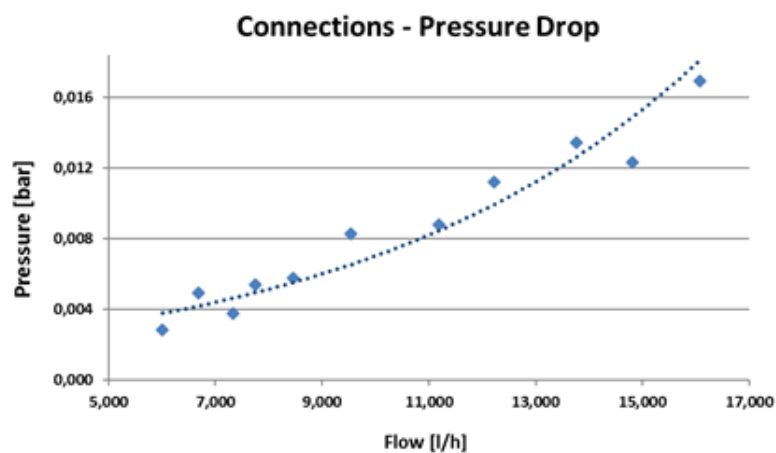


Chart. 8 Results of the test: Pressure drop values by increasing the water flow

5.3.2 Test on the Serpentine

The test on the serpentine is focuses on the water pressure drops behavior while changing the flow. For doing this test the serpentine was connected to the plant by using the plastic pipe previously measured: it was cutted in two peaces, one connected to the inlet and one to the outlet of the serpentine. Moving valves V1 and V2 [Fig. 45] a flow range between 16 and 0.003 l/h was obtained. The results are here reported.

Flow [l/min]	Pin [bar]	Pout [bar]	Δp	Flow [l/h]
0,26	1,05	0,68	0,364	15,94
0,24	1,00	0,69	0,310	14,39
0,23	1,00	0,73	0,278	13,55
0,22	0,96	0,68	0,273	13,41
0,22	0,96	0,71	0,258	12,97
0,20	0,96	0,72	0,241	12,48
0,17	0,71	0,54	0,172	10,25
0,16	0,72	0,56	0,160	9,74
0,15	0,72	0,58	0,137	8,78
0,13	0,72	0,60	0,117	7,69
0,10	0,62	0,53	0,084	6,10
0,07	0,60	0,54	0,056	4,55
0,06	0,60	0,56	0,041	3,54
0,02	0,58	0,57	0,013	1,38
0,02	0,52	0,51	0,008	0,88
0,003	0,53	0,53	-0,001	0,19

Tab. 16 Results of the test on the pipe

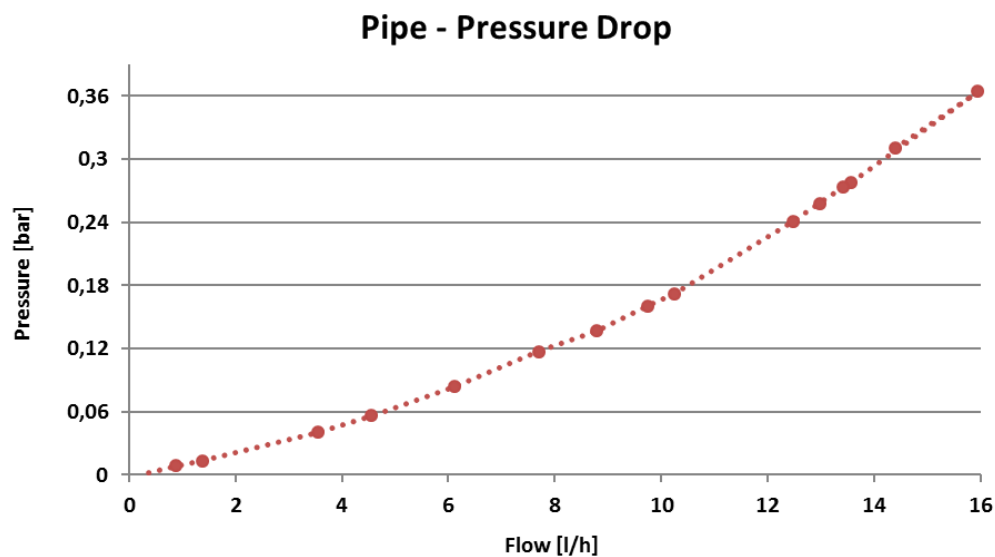


Chart. 9 Results of the test: Pressure drop values by increasing the water flow

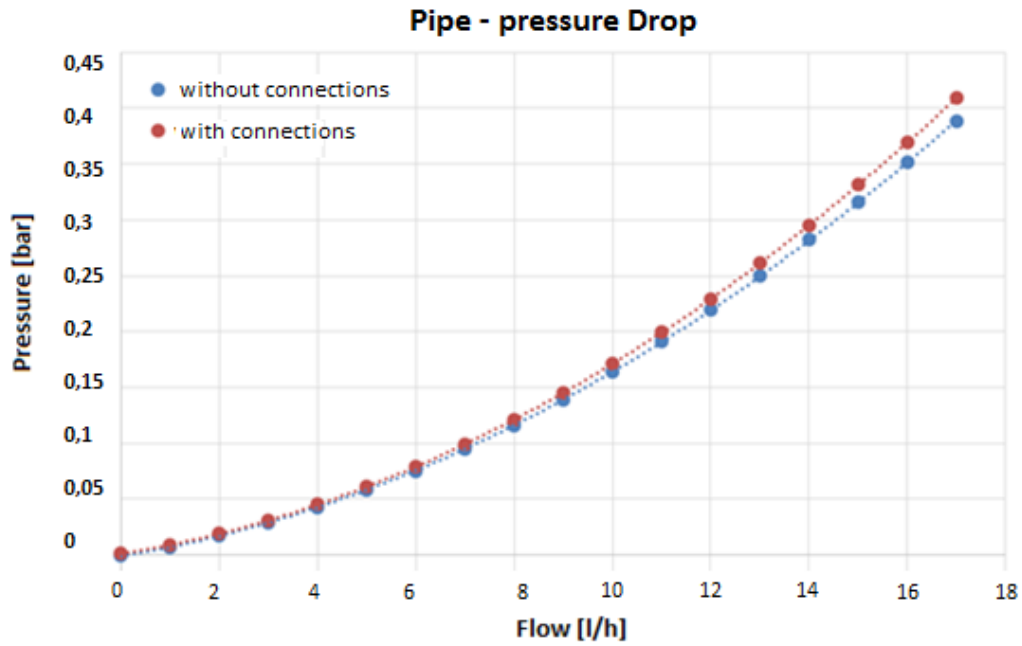


Chart. 10 Pressure drop comparison: pipe with and without the connection to the test set-up

In chart 10 are reported the values obtained for the pipe and the same values after having subtract the drop caused by the connection. Comparing it with the values obtained from the numerical simulations made with ANSYS, the result in chart 11 is obtained.

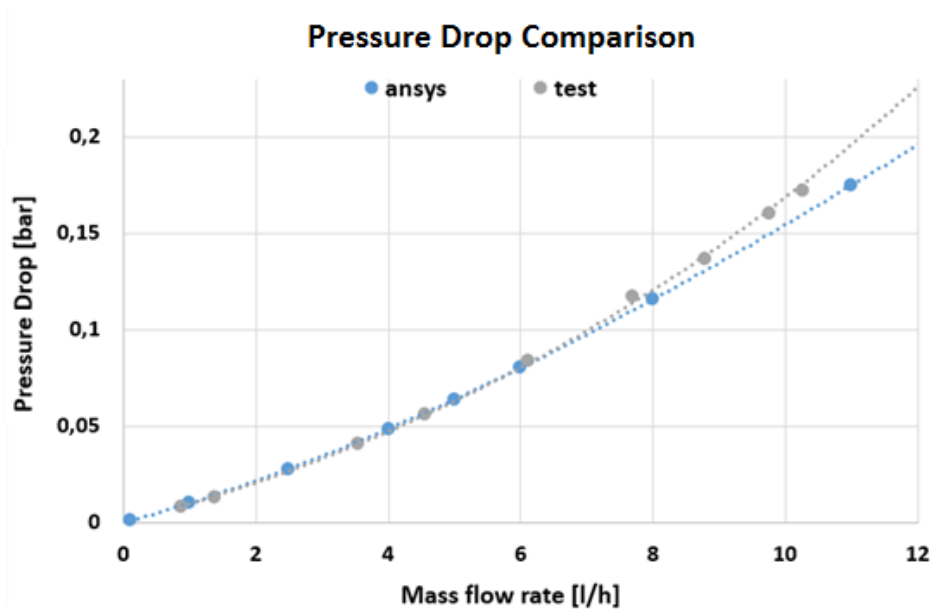


Chart. 11 Results of the test: Pressure drop comparison by increasing the water flow

The chart shows that simulations give good results in comparison to those obtained from the tests. The trend of the two curves stays closer till about 8 l/h. In fact starting from this point Re number increase and the motion pass from laminar to turbulent. This transition is detected during the experimental tests but not from ANSYS Fluent, because, for the turbulent motion, several specific implementation methods exist, and a laminar model was used. The turbulent models were tested but, as chart 12 shows, they are not reliable for the transition zone, but only for the fully turbulent motion. In fact the trend of the curves that results from the values obtained in Fluent with a turbulent setting, stay far from the curves obtained with the tests.

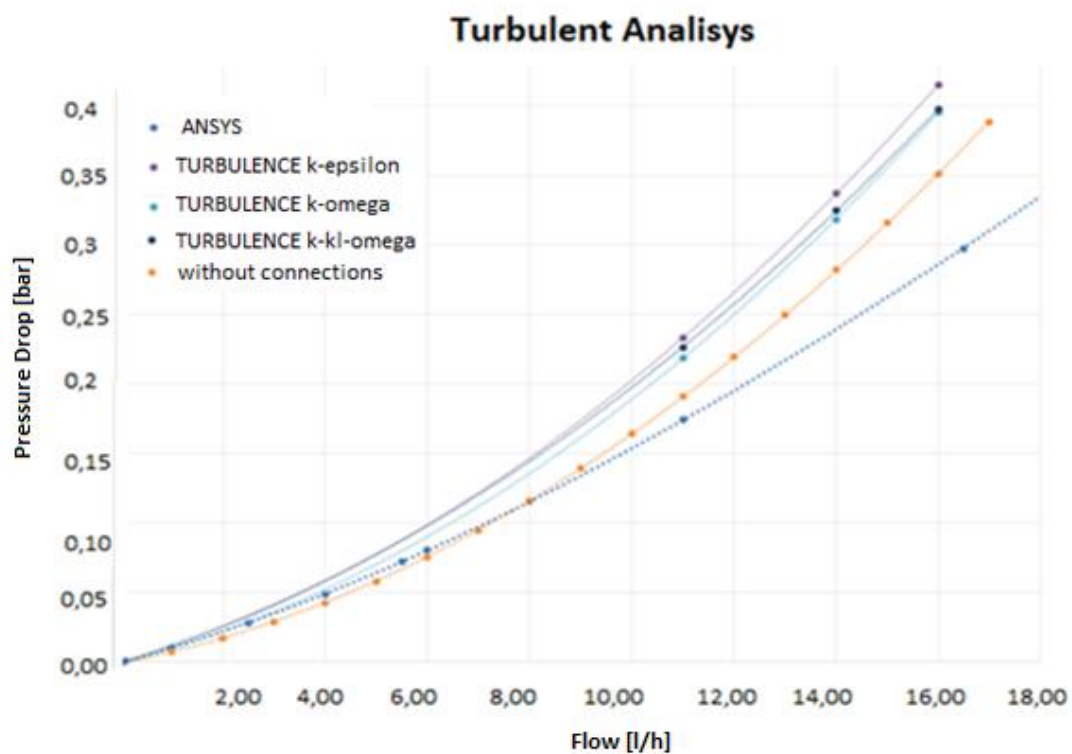


Chart. 12 Turbulent analysis of the water flow using three different methods implemented in ANSYS Fluent

5.4 Test on the Plate

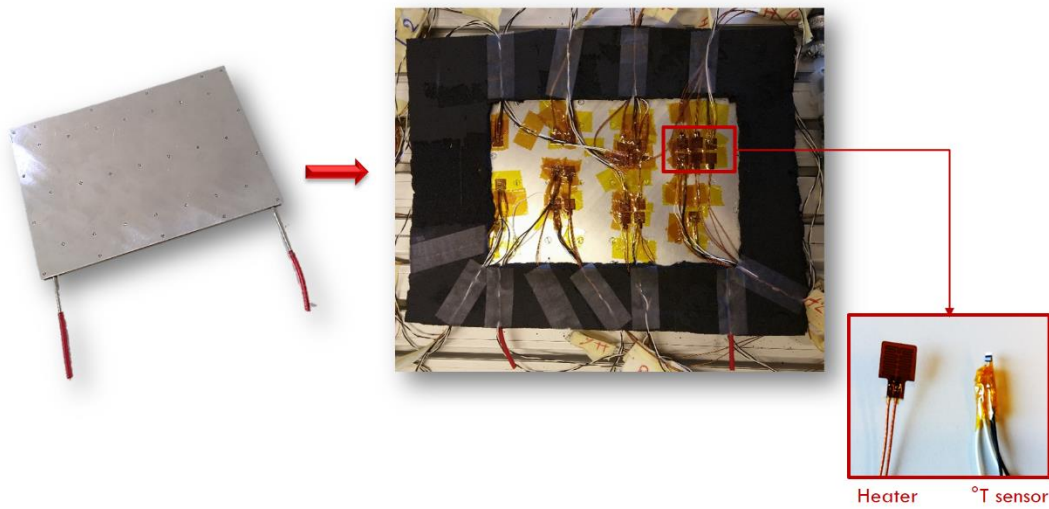


Fig. 48 Plate's test set-up

Once tested the pipe, the whole plate was tested too. The aim was to simulate the heat spread by the chips on the ROU board. For doing this, the plate was completely insulated in a foam box. On one side was decided the position of the main chips, following the indication given by the electronics team. The location of each chip is reported in figure 49. To simulate the chips polyamide heaters were used. Their surfaces measure 1 cm^2 .

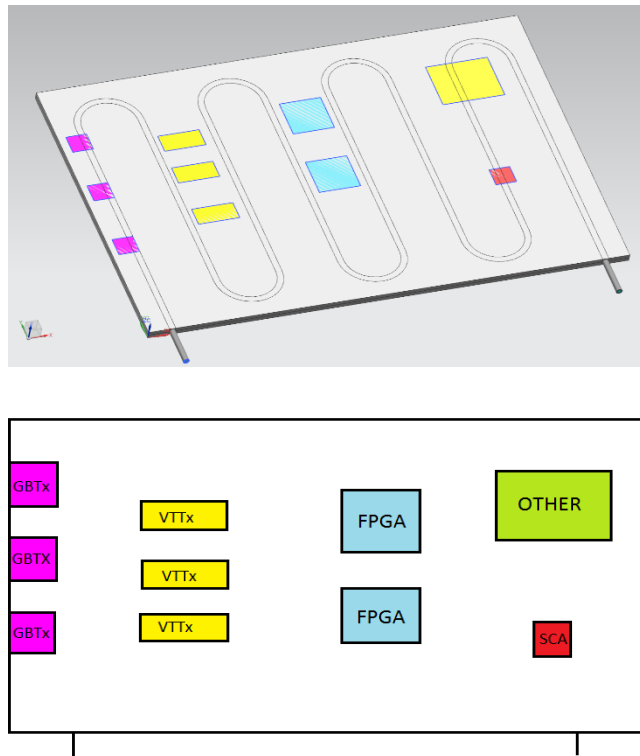


Fig. 49 Chips position on the plate

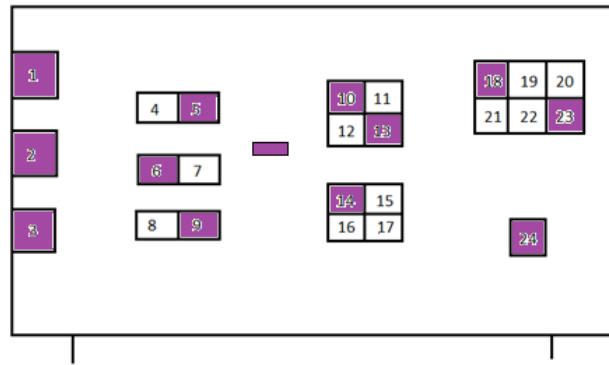


Fig. 50 Position of the thermal sensors above the heaters.

To simulate GBTx and SCA only one of this heater was used in fact the chips have the same dimensions of this resistances. VTTX instead, requests 2 heaters for covering its whole surface, while FPGA needs 4 and OTHER needs 6 of them. In this tracks the heaters were coupled with the plate by using a thermal interface material. Above some of this chips, temperature sensors, PT 100, were glued. The sensor's position is reported in figure 50 as the violet squares.

Several tests were made on the plate and are now here reported:

- Test on the plate by varying the water flow and the power spread by the chips. Inlet water at 20°C;
- Test on the plate by varying the water flow and the power spread by the chips. Inlet water at 15°C;
- Thermal analysis by using an infrared camera.

5.4.1 First Test with the Inlet Water Flow at 20°C

The first test with the inlet water at 20°C, that will probably be the temperature use in the ITS cooling system, was made for three different level of the chips' power: nominal power, +50%, -50%. The test was performed also for three different values of the water flow: the nominal value, 11 l/h, and for 5 and 15 l/h. Each chip was simulated by the use of the heater, previously introduced. Each heater that composes a chip was linked to a power supply for giving it the right voltage value to produce the corresponding power value. Table 17 reports the voltage values and the electrical current and also the values for the equivalent electrical resistance because the chips made of more than one heater, were connected to the power supply by an electric parallel.

The temperature values for each chip and for the plate were taken from the PT100. PT100 and heaters were coupled to the plate by using a thermal paste.

VTTx	P	I	V	Req
-50%	0,18	0,73	1,53	2,083
Nominal	0,37	1,03	2,16	2,083
+50%	0,56	1,27	2,65	2,083

FPGA	P	I	V	Req
-50%	0,93	2,19	3,42	1,56
Nominal	1,87	3,09	4,84	1,56
+50%	2,81	3,79	5,92	1,56

OTHER	P	I	V	Req
-50%	0,41	1,09	2,28	2,083
Nominal	0,83	1,54	3,22	2,083
+50%	1,25	1,89	3,95	2,083

SCA	P	I	V	R
-50%	0,05	0,06	0,79	12,5
Nominal	0,1	0,08	1,11	12,5
+50%	0,15	0,10	1,36	12,5

Tab. 17 Electrical features at different power level for the electronics chips

Here are reported the results, in °C, obtained for each water flow at the three different power level.

5 l/h			
	-50%	Nominal	50%
FPGA	28	36	42,7
VTTX	24,5	28	29,5
GBTX	25,6	31	36
SCA	21,8	232,3	24,7
OTHER	25,3	30,5	35,6
PLATE	22,7	24,6	26,5

11 l/h			
	-50%	Nominal	50%
FPGA	27	34	41,7
VTTX	23	25,5	28
GBTX	24,5	28,8	33,2
SCA	21,3	22,3	23,2
OTHER	25	29,2	33,7
PLATE	21,6	22,8	24

15 l/h			
	-50%	Nominal	50%
FPGA	26	33,3	39,5
VTTX	22,6	33,3	29
GBTX	23,6	27,524	31,8
SCA	21	21,2	22
OTHER	24,6	29	32,5
PLATE	20,4	21,4	22

Tab. 18 Chips' temperature values [$^{\circ}\text{C}$], obtained at different water flow and power at 20°C

5.4.2 Second Test with the Inlet Water Flow at 15°C

The same kind of experiment was made on the plate by using an inlet water flow at 15°C . Nothing changes from the previous set-up, and for this test the results are here reported.

5 l/h LOW T			
	-50%	Nominal	+50%
FPGA	19	26,6	35
VTTX	17,5	20,5	24
GBTX	17,5	22	28,5
SCA	13,7	14,8	17,2
OTHER	19	23,2	29,8
PLATE	14,2	15,5	18,5

11 l/h LOW T			
	-50%	Nominal	+50%
FPGA	20	27,2	34,2
VTTX	17	20,5	22,2
GBTX	17,5	21,8	26,4
SCA	14	14,9	16
OTHER	18,2	23,7	27,5
PLATE	14,15	15,5	16,3

15 l/h LOW T			
	-50%	Nominal	+50%
FPGA	19,6	27,5	33
VTTX	15,9	18,8	19,6
GBTX	16,8	21,8	25
SCA	14	16,2	17
OTHER	19,2	25,9	30,9
PLATE	13,6	15,4	15,9

Tab. 19 Chips' temperature values, obtained at different water flow and power, at 15°C

5.4.3 Thermal Analysis with the Infrared Camera



Fig. 51 Infrared camera: installation for acquiring temperature data from the cold plate

For taking temperature data from the cold plate by using the infrared camera, a particular installation occurred. The camera was placed perpendicular to the plate and then hanged on an aluminium support cover with black paper to avoid the reflection of the light. For this reason, all the tests were performed in a dark environment. In this case the PT100 were removed and the heaters were glued on the plate by using a thermal pad made of silicone also for trying to have a better coupling between the plate and the chips. Tests were performed at the same conditions used before that means same water flow, 5,11,15 l/h and for each flow, at the three different power level, -50%, Nominal, +50%. The results are reported in table 20(a). In the same way was performed also the case at low temperature and the results here obtained are reported in table 20(b). The picture captured by the infrared camera are reported in figure 52, 53 and 54 for the main case, the nominal one.

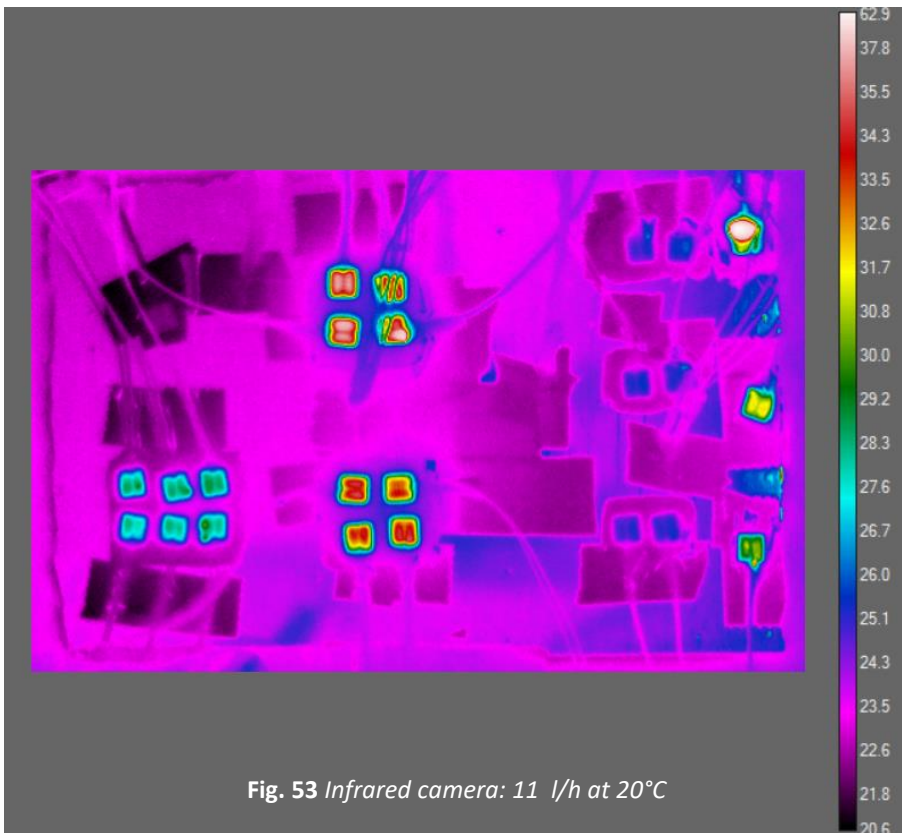
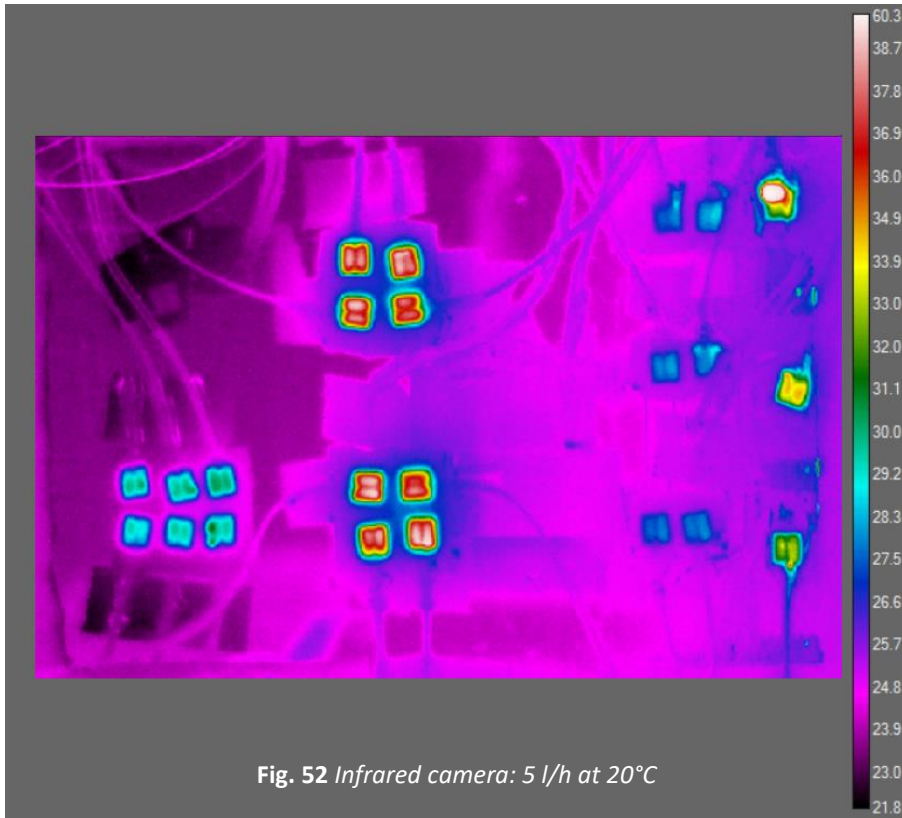
5 l/h CAMERA				5 l/h CAMERA LOW T			
	-50%	Nominal	50%		-50%	Nominal	50%
FPGA	25,6	30,1	34,5	FPGA	20,8	25,3	29,5
VTTX	23,7	26,1	28,8	VTTX	19	21,6	24,1
GBTX	24,9	29,9	33,8	GBTX	20	24,2	28
SCA	22	22,9	24,1	SCA	17	18	19,4
OTHER	23,8	26,3	29	OTHER	18,7	21,6	24,4
PLATE	23	24,4	25,8	PLATE	19,4	20,7	22,1

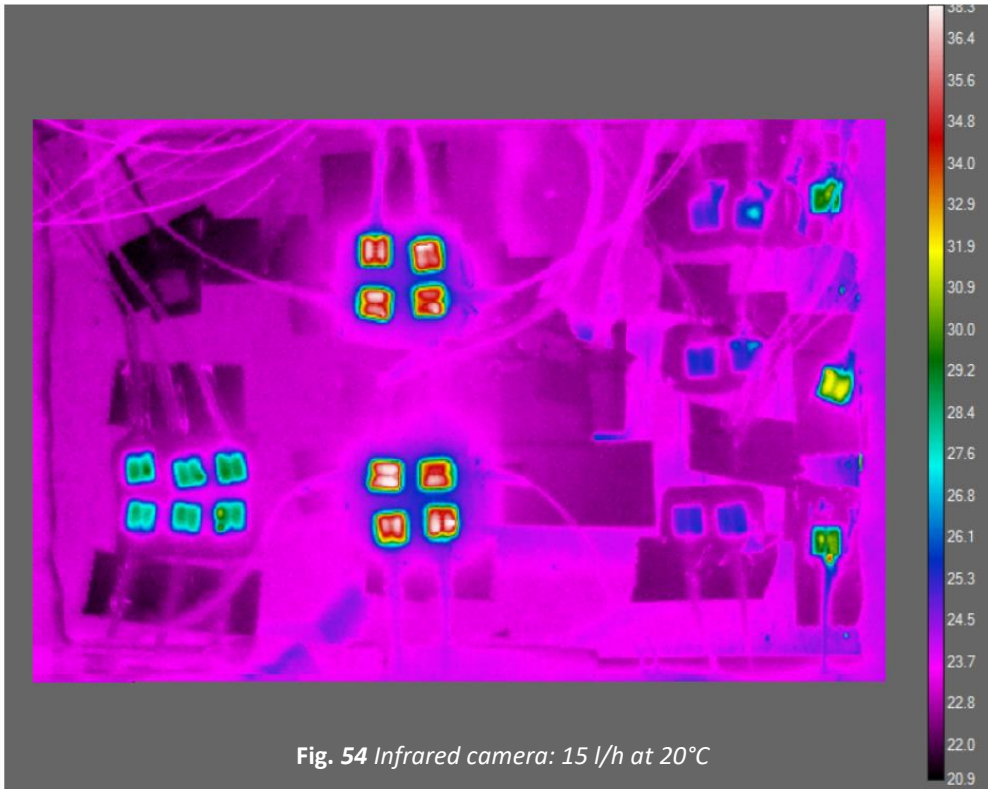
11 l/h CAMERA				11 l/h CAMERA LOW T			
	-50%	Nominal	50%		-50%	Nominal	50%
FPGA	24,2	27,3	32,2	FPGA	19,7	23,4	26,5
VTTX	22,4	24,1	25,8	VTTX	17,6	19,2	20,8
GBTX	24,2	27,6	30,5	GBTX	19	21,6	25
SCA	20,9	21,7	22,6	SCA	17,2	17,3	17,8
OTHER	22,6	25,1	27,7	OTHER	18,2	20,4	22,2
PLATE	22,2	22,8	24	PLATE	18,5	19,2	19,8

15 l/h CAMERA				15 l/h CAMERA LOW T			
	-50%	Nominal	50%		-50%	Nominal	50%
FPGA	24,5	28,1	31,9	FPGA	19,9	23,5	26,5
VTTX	22,7	23,7	25,3	VTTX	17,6	19	20,4
GBTX	24,1	26,7	31,2	GBTX	18,6	21,7	24
SCA	21,4	21,8	22,4	SCA	17,4	17,6	17,9
OTHER	23,1	25,1	27,1	OTHER	18,2	20,6	22,5
PLATE	22,2	22,8	23,5	PLATE	18,5	19,3	19,7

(a) (b)

Tab. 20 Chips' temperature values [°C], obtained at different water flow and power, at 20°C (a) and at 15°C (b)





6 Comparison Between Simulations and Experimental Results

It's possible now to make a comparison between the simulation results and the values obtained by the test and the infrared camera. The comparison will involve the three main water flow at the nominal chips power. An overview of the chips and plate temperature values is here reported in table 21.

5 l/h			
	ANSYS	TEST PT100	INFRARED CAMERA
FPGA	25,4	36	30,1
VTTX	24,8	28	26,1
GBTX	25,5	31	29,9
SCA	21,67	23,3	22,9
OTHER	22,8	30,5	26,3
PLATE	23,8	24,6	24,4

11 l/h			
	ANSYS	TEST PT100	INFRARED CAMERA
FPGA	24,3	34	27,3
VTTX	22,5	25,5	24,1
GBTX	23,2	28,8	27,6
SCA	20,9	22,3	21,7
OTHER	21,7	29,2	25,1
PLATE	22,5	22,8	22,8

15 l/h			
	ANSYS	TEST PT100	INFRARED CAMERA
FPGA	23,5	33,3	28,1
VTTX	22	24	23,7
GBTX	22,5	27,5	26,7
SCA	20,7	21,2	21,8
OTHER	21,5	29	25,1
PLATE	22,29	21,39	22,8

Tab. 21 Chips temperature: comparison between tests and simulations at 5,11 and 15 l/h with an inlet temperature of 20°C

As the table shows, exists an important difference between the values and the way in which they were obtained. As said in chapter 5, section 5.3, is difficult to reach with the experimental tests, the same value given by the simulations. On the other hand,

exists also a difference between the data acquired with the infrared camera and those obtained with the PT100. Looking at table 21, it's possible to notice that all the methods give about the same temperature values for the plate. This means that the coupling between the PT100 and the plate was optimal. The main difference is on the chips. This is due to the difficulties in gluing the heaters on the plate but mainly is due to the thermal resistance between the aluminium plate and the heater. In fact, trying to calculate analytically this resistance and the difference in temperature between the heater and the plate, starting from the plate temperature gave from the simulations, values closer to those obtained with the infrared camera, are reached. Figure 55 shows how the system is composed. For calculating the temperature difference between the plate and the heater surface, the following equation has to be used:

$$Q = \frac{T_2 - T_1}{R_{eq}} \quad (62)$$

where R_{eq} is the sum of the resistance of each layer, s is the thickness of the layer and λ the thermal conductivity of each material:

$$R_{eq} = \frac{s'}{\lambda'} + \frac{s''}{\lambda''} + \frac{s'''}{\lambda'''} \dots \quad (63)$$

The properties of each material here involved are reported in the table below.

	S [mm]	λ [W/mK]
KAPTON	0,1	0,46
COPPER	0,1	395
THERMAL SILICONE	0,3	5

Tab. 22 Materials involved in the coupling between the plate and the heater: properties

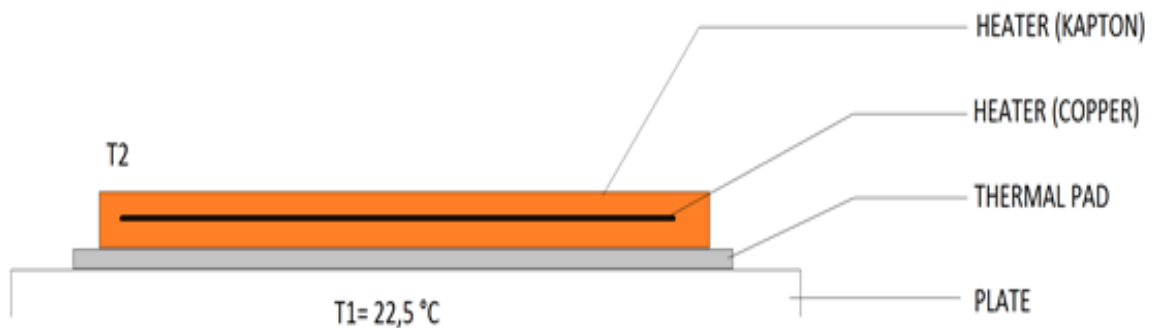


Fig. 55 Heater coupling with the plate: heater is made of kapton and copper, the thermal pad of a conductive silicon

For this system R_{eq} results:

$$R_{eq} = \frac{0,1 * 10^{-3}}{0,46} + \frac{0,1 * 10^{-3}}{395} + \frac{0,3 * 10^{-3}}{6} = 0,0002676 \frac{m^2 K}{W}$$

Performing the calculations for each chips the following temperature values are obtained for T2:

5 l/h	Q [W/m2]	ΔT	T2 [°C]
FPGA	18750	5,018	27,52
VTTX	3750	1,004	23,50
GBTX	12000	3,212	25,71
SCA	1000	0,268	22,77
OTHER	6666	1,784	24,28

11 l/h	Q [W/m2]	ΔT	T2 [°C]
FPGA	18750	5,018	27,72
VTTX	3750	1,004	23,70
GBTX	12000	3,212	25,91
SCA	1000	0,268	22,97
OTHER	6666	1,784	24,48

15 l/h	Q [W/m2]	ΔT	T2 [°C]
FPGA	18750	5,018	29,28
VTTX	3750	1,004	25,26
GBTX	12000	3,212	27,47
SCA	1000	0,268	24,53
OTHER	6666	1,784	26,04

Tab. 23 Chips temperatures obtained after adding the coupling thermal resistances

Evaluating this results with the one in table 21, can be noticed that chips' temperatures are closer to those taken with the infrared camera: the values taken with the camera are really reliable. A visual comparison is reported in table 24.

	5l/h		11 l/h		15 l/h	
	T2 camera	T2 simul. correction	T2 camera	T2 simul. correction	T2 camera	T2 simul. correction
FPGA	30,1	27,52	27,3	27,72	28,1	29,28
VTTX	26,1	23,50	24,1	23,70	23,7	25,26
GBTX	29,9	25,71	27,6	25,91	26,7	27,47
SCA	22,9	22,77	21,7	22,97	21,8	24,53
OTHER	26,3	24,28	25,1	24,48	25,1	26,04

Tab. 24 Chips temperatures: comparison between the camera value and the values correct with the thermal resistance

Counting all the things said previously and keeping a margin of security, the chips can reach at maximum 30/31°C, while the plate won't go above 24°C.

Giving a look at the water outlet temperatures is possible to understand if there will be the possibility to add another board on the other side of the plate for a total heat of about 51 W. In the studied case, the forecast temperature difference between pipe's inlet and outlet, was also confirmed from the simulations and the tests, as can be seen in the following table. Calculating the same difference for the case at 51 W, the last column in table 25 is obtained.

ΔT [°C]				
	Calculations	ANSYS	Tests	With 51 W
5 l/h	4,47	4,5	3,6	8,79
11 l/h	2	2,15	1,6	3,99
15 l/h	1,49	1,35	1,2	2,93

Tab. 25 Temperature difference between inlet and outlet at the nominal case

It can be concluded that there is a real possibility to couple another board, in fact at maximum, staying at the nominal water flow of 11 l/h, a difference of 4°C is reached that means water at the outlet will be at 24°C. If something wrong occurs and the water flow decreases till 5 l/h a significant ΔT of about 9°C is achieved.

Conclusions

The upgrade of the ALICE experiment at CERN will be performed in 2020. ALICE (A Large Ion Collider Experiment) detector studies the heavy-ion collisions and the physics of strongly interacting matter, and in particular the properties of the Quark-Gluon Plasma, by colliding ions. The detector is composed of several layers that are concentric with the beam pipe that comes from the LHC and is the path along which particles run. When they arrive in the middle of the detector they collide together and generate new different particles. To study the different products of the collision, each layer has its own identity. The inner layer, the one close to the beam pipe is the Inner Tracking System, ITS. Its aim is to recognise particles containing heavy quarks by identifying the points at which they decay. The upgrade involves the total replacement of the old structure with one in carbon fibre. In additions it will provide a new cooling system and a new electronics management. In fact, there will be new electronics boards for the read out of the data taken during the collisions. The boards will house new radiations resistant components. There will be 12 crates containing each one 16 boards for a total of 192 boards. Each board spread heat for about 26 W. This is a problem because of the requirements on the temperature that must be maintained inside the cave situated hundred meters underground. The temperature in the cave has to be maintained around 25°C and no condensation has to appear on the electronics components. In this work a dedicate cooling system for the read out electronics boards, was studied. At first preliminary analysis and considerations were made to develop the first 3D model of a cooling plate on which the boards will be coupled. Here only the read out board is studied because the power supply board has not yet been designed. A deeper analysis on the water convection was made, to try to understand the behaviour of the water inside the pipe, while exchanging heat with the chips. This investigation gave then the foundations to build an appropriate mesh, for performing thermal fluid dynamics simulations with ANSYS Fluent. The theoretical investigation provides information of what happens to the water near the pipe walls. This was fundamental while building the mesh. After several simulations for deciding the best mesh to use to perform the calculations on the whole plate, one grid was selected and reproduced on the entire water flow inside the plate. In the meanwhile, a test was conducted to obtain the values of the pressure drop inside the serpentine, and to obtain the highest temperature achievable from the chips on the board, here simulated with electrical resistances called heaters. To validate this tests, others were done by using the infrared camera. Each test and simulation was performed at 15 and 20°C and at 5, 11, 15 l/h at the nominal chips' power but tests were also made at $\pm 50\%$ of the nominal power. Comparing the results, it appears that values obtained with the tests are higher than those given by the simulations. This was due to the fact that the simulations were performed in adiabatic conditions, not the realistic ones. Considering

the thermal resistances across the materials involved in the coupling with the plate, values become more reliable. This comparison makes clear that the maximum temperature achievable from to plate is about 31°C. Furthermore, the water that exits the plate is cold enough to be able to cool another board coupled on the same plate. Here only a first aluminium plate was studied, but in the meanwhile another plate made of copper was manufactured in a different way: in a 4 mm thick copper plate the pipe's shape was machined and once installed inside its excavation, it is cover and fix with a copper brazing. Another possibility is to build the plate starting from an aluminium casting all around the pipe, inside a mold. Other investigations can be made on the coupling material, that means analyse the behaviour of different thermal pads and pastes. At the end the idea is to test also the plate coupled with the final board, once this will be completed.

Bibliography

- [1] F. P. Incropera, D.P. Dewitt, T.L. Bergman, A.S.Lavine (Wiley 2013). Principles of heat and mass transfer.
- [2] S.G. Kandlikar, S. Garimella, D.Li.S. Colin, M.R. King (Elsevier 2006). Heat transfer and fluid flow in minichannels and microchannels.
- [3] Carl Schaschke (Icheme 1998). Fluid Mechanics.
- [4] R.K. Shah, A.L. London (Academic Press 1978). Laminar Flow Forced Convection in Ducts.
- [5] Sadik Kakac, Yaman Yener, Anchasa Pramuanjaroenkij (CRC Press, 2014). Convective Heat Transfer
- [6] R. K. Shah and A. L. London (1971). Laminar Flow Forced Convection Heat Transfer and Flow Friction in Straight and Curved Ducts a Summary of Analytical Solutions.
- [7] H. Schopper, L. Di Lella (World Scientific 2015).60 years of CERN.
- [8] TDR Technical Design Report for the Upgrade of the ALICE Inner Tracking System.
- [9] V. Gnielinski. Heat transfer in Pipe Flow.
- [10] Ning Hsing Chen (1979). An Explicit Equation for Friction Factor in Pipe.
- [11] A.A. Donaldson, D.M. Kirpalani/, A. Macchi (2010). Single and two-phase pressure drop characteristics in serpentine mini-channels.
- [12] Jyh-tong Teng et al. Chung Yuan Christian University, Chung-Li Taiwan (2012). Fluid Dynamics in Microchannels.

- [13] I.E. Idel'chik (1966). Handbook of Hydraulic Resistance.
- [14] Sadik Kacaç, Hongtan Liu (2002). Heat Exchangers.
- [15] The ALICE Collaboration (203-2014). Technical Design Report for the Upgrade of the ALICE Inner Tracking System.
- [16] Ansys Workbench / Ansys Fluent User's Guide

Websites

- [17] <https://home.cern>
- [18] <http://aliceinfo.cern.ch>
- [19] <http://aliceinfo.cern.ch/ITSUpgrade>
- [20] <http://cfd.ninja>
- [21] <http://www.cfd-online.com>
- [22] <https://confluence.cornell.edu>
- [23] <https://www.sharcnet.ca/Software/Ansys/16.2.3>
- [24] <http://www.pointwise.com/theconnector/May-2012/Mesh-Quality.shtml>
- [25] http://www.academia.edu/LOCAL_MESH_CONTROLS_ANSYS_WORKBENCH

Ringraziamenti

Nel 2013 una visita al CERN di Ginevra mi fece dire: “io in qualche modo qui voglio tornarci!” E dopo 3 anni finalmente il desiderio si è realizzato. Per avermi permesso di realizzare questo piccolo sogno il primo grande grazie va alla sezione INFN di Padova. In particolare i ringraziamenti vanno ad Andrea Dainese per avermi dato questa possibilità, per aver seguito il mio percorso in questi mesi e per essere sempre stato disponibile a rispondere alle mie domande. Un altro grandissimo grazie di cuore va a Massimo Benettoni che qui a Padova è stato mentore, consigliere ed amico. In ambito INFN un altro grazie va a tutti i ragazzi dell’ufficio tecnico di INFN per aver sopportato la mia presenza, per avermi insegnato ad usare NX e per avermi tenuto compagnia mentre aspettavo i comodi di ANSYS.

Poi è giunto il momento di trasferirsi al CERN facendo bagaglio di tutte le nozioni datemi in questi anni e soprattutto quelle fresche fresche di Massimo. Ed è qui che mi voglio soffermare con il ringraziamento più sentito. Andrea Francescon, a te va il grazie più grande. Un grazie sincero non solo per avermi seguito così come nessuno avrebbe potuto fare, ma un grazie per la tua infinita disponibilità e gentilezza, per avermi insegnato davvero tante cose di cui farò tesoro a vita. Sei stato un riferimento ma anche un ottimo compagno di chiacchiere tra l’incollaggio di un heater e l’altro. Mi hai regalato un’esperienza intensa e varia, ricca di bei momenti ma anche di alti e bassi. Ho imparato a seguire un certo rigore “scientifico” ma anche morale. Grazie Andrea, grazie dal profondo del cuore.

E come potrei non ringraziare anche il gruppo dell’ITS al CERN! Corrado Gargiulo ed Elisa Laudi grazie per esservi sempre interessati dell’avanzamento del mio lavoro per non avermi mai negato un sorriso o una parola. Grazie inoltre Elisa per avermi dato sempre utilissimi consigli non solo tecnici, ma anche di vita. E qui mi sento di dover mandare un piccolo grazie anche al mitico Gregory Lahu per la sua simpatia e per avermi permesso di realizzare con lui il prototipo scambiando delle divertenti chiacchiere francesi. Voglio ringraziare inoltre in questo contesto gli amici cernioti del pranzo: Max, Antonio, Andrea, Sofia, Alex, Munir. Grazie per avermi dato la possibilità di impraticarmi con l’inglese spicciolo ma soprattutto per essere stati dei buoni amici lungo il percorso. In tema di pranzi ci tengo a ringraziare anche Andrea Festanti per non avermi fatto mai sentire sola i primi giorni al CERN e per essere stato davvero un amico e compagno d’ufficio divertentissimo. Grazie per avermi fatto conoscere nuove persone e in particolare il fantastico Umberto de Sanctis che voglio ringraziare per le crepes del pomeriggio e le nozioni di fisica quantistica protrattesi fino alle 2 di notte. Grazie anche ad Elena Buratin per essere stata una super amica sempre disposta ad aiutarmi. Grazie per il termometro Elena! Ringrazio in ultima il CERN come entità “mistica” più che materiale, per non avermi fatta mai sentire sola e fuori posto, perché è stato come una casa e perché lo porterò nel cuore per il resto del tempo concessomi.

Nel concludere ringrazio chi mi ha accompagnato lungo questi 5 memorabili anni. Grazie a tutti gli amici di Leds grazie dal primo all'ultimo, dal più old al più young! Grazie per aver condiviso assieme del tempo di valore sia dal punto di vista contenutistico/scientifico sia dal punto di vista umano. Grazie a tutti per i bei momenti passati assieme e auguro il meglio ad ognuno di voi. Grazie anche al gruppo di Unizeb per il coraggio con cui ha affrontato e costruito quella che inizialmente era una mera idea nella testa mia, di Filippo Piovanello e Marco Costa a cui va un grazie per essere stati buoni compagni di avventura.

Grazie poi ad Enrico per essermi sempre stato vicino, per aver sempre mostrato interesse e supporto in ogni cosa che ho fatto, per avermi dato pieno appoggio senza mai tirarsi indietro davanti ai problemi ma anzi per avermi aiutato a risolverli. Grazie agli amici di una vita, i BertioStello, grazie per volermi bene per come sono e per essere ancora qui assieme a condividere ogni cosa dopo 10 lunghi anni.

In fine voglio chiudere ringraziando chi mi ha dato la possibilità di arrivare qui dove sono ora: grazie famiglia, grazie Mamma e Papà per non avermi mai fatto mancare nulla, per avermi permesso di arrivare qui, per aver fatto sacrifici, per credere in me più di quanto io non sarò mai in grado di fare, per avermi sempre appoggiato e sostenuto. Grazie dal più profondo del cuore.